Budapest University of Technology and Economics
Faculty of Mechanical Engineering

Student Scientific Report

Evaluation of fracture mechanical tests on composite beams by the J-integral and higher-order theories

Author:
Balázs Kiss

Supervisors:
Dr. András Szekrényes
Dr. Gergely Czél

Department of Applied Mechanics

October 26, 2018

Declaration of Authorship

I, Balázs Kiss, the undersigned, hereby declare that the present student scientific report has been prepared by myself without any unauthorized help or assistance such that only the specified sources (references, tools, etc.) were used. All parts taken from other sources word by word or after rephrasing but with identical meaning were unambiguously identified with explicit reference to the utilized sources.

Budapest, December 11, 2018

....

Balázs Kiss

Acknowledgements

I would like to express my great appreciation to my supervisor Dr. András SZEKRÉNYES who supported and inspired me throughout this project. I am thankful for his aspiring guidance, constructive suggestions and advice during my work, which will be an unforgettable experience during my all life.

Furthermore, I would also like to express my deep gratitude to Dr Gergely CZÉL for his generous support. He never regretted the time to deal with my project, even if he must have sacrificed his free time for helping me. Without him and his knowledge, I wouldn't have been able to perform experimental investigation of the composite beams, which represents an important role in my report.

Finally, I wish to thank my parents for their support and encouragement throughout my study.

BUDAPEST UNIVERSITY OF TECHNOLOGY AND ECONOMICS

Abstract

Faculty of Mechanical Engineering
Department of Applied Mechanics

Mechanical Engineering

Evaluation of fracture mechanical tests on composite beams by the J-integral and higher-order theories

by Balázs KISS

By using more and more fiber reinforced thermoset polymer composites the need of undestanding their mechanical description becomes inevitable in the engineering life. Because of the direction dependent material properties they offer great freedom to the designers, although, their complex mechanical behaviour hides some drawbacks, as well. Comparing to the other commonly used heterogeneous engineering materials, very different modes of failure can take place. One of the most distinctive and typical form of these damages is the so-called interlaminar fracture or delamination. During this phenomenon the laminated layers get separated from each other causing significant loss of mechanical properties. Even nowadays, it is a pioneering research topic from fracture mechanics and material science point of view, as well.

In my student scientific report I deal with those kind of mechanical models which are applicable to describe laminated composite beams. New types of model are developed and compared to each other. Along the thickness of the beam the displacement field is approximated with higher-order polynomials. The equilibrium equations are derived by using the virtual work principle [1, 5, 7]. Solving the system of ODEs and utilizing the more accurate displacement and stress field around the crack tip the application of the J-integral becomes possible. According to the basic definition of this integral the energy release rate, the fundamental quantity of the linear elastic fracture mechanics, can be calculated. Reaching the critical value of this parameter in a given material the delamintaion propagates and the layers separate from each other [2]. Furthermore, by using the J-integral more accurate and exact mode partitioning becomes achievable (in the case of beam specimens mode-I and mode-II can appear) comparing to the previously published solutions and models in the literature [4].

Finally, the newly developed models are used to determine the basic fracture mechanical properties of UD glass and carbon fiber reinforced specimens, which were made myself.

For my grandparents, who had never
had possibility of learning.

Contents

Acknowledgements **v**

Abstract **vii**

1 Introduction **1**
- 1.1 Basics of fracture mechanics 1
- 1.2 Delamination in composite structures 2
- 1.3 Main aims and analysis methods 3
- 1.4 Orthotropic and transversely isotropic materials 4
  - 1.4.1 Plane stress reduced constitutive relations 5

2 The basic equations of delaminated composite beams **7**
- 2.1 Semi-layerwise beam model 8
- 2.2 The system of exact kinematic conditions 8
- 2.3 Virtual work principle and constitutive equations 10
- 2.4 Equilibrium equations - Invariant form 13
  - 2.4.1 Undelaminated region 13
  - 2.4.2 Delaminated region 14

3 The method of four equivalent single layers **15**
- 3.1 Undelaminated region 15
  - 3.1.1 Third-order beam theory 17
  - 3.1.2 Second-order beam theory 17
  - 3.1.3 First-order beam theory 18
- 3.2 Delaminated region 18
  - 3.2.1 Third-order beam theory 20
  - 3.2.2 Second-order beam theory 20
  - 3.2.3 First-order beam theory 20

4 J-integral **23**
- 4.1 Basic definition 23
- 4.2 Mode partitioning of the total J-integral 24

5 Built-in configuration **27**
- 5.1 Analytical solution 27
  - 5.1.1 Continuity conditions 28
  - 5.1.2 Boundary conditions 31
- 5.2 FEA solution 32
- 5.3 Results - Displacement and stress 33
  - 5.3.1 Transversely isotropic beam 33

5.3.2 Bi-material beam 37
5.4 Energy release rates and mode mixity 40
5.4.1 Transversely isotropic beam 40
5.4.2 Bi-material beam 42

6 Asymmetric Double Cantilever Beam **43**
6.1 Analytical solution 43
6.2 FEA solution 45
6.3 Energy release rates and mode mixity 46

7 Measurements **47**
7.1 Manufacturing of the composite specimens 47
7.2 Material parameters 48
7.3 Measurement results 49

Bibliography **59**

A Matrix elements - Method of 4ESLs **61**
A.1 Third-order beam theory 61
A.2 Second-order beam theory 65
A.3 First-order beam theory 67

B Other evaluation techniques in the literature **69**
B.1 Suo-Hutchinson solution 69
B.2 Williams and Bruno-Greco solutions 70
B.2.1 Curvature based solution (Williams) 71
B.2.2 Strain and stress based solutions (Bruno-Greco and Williams) 72
B.3 VCCT 73

C Laminated composite beams with complex lay-up sequence **75**

Chapter 1

Introduction

In this chapter those kind of definitions are introduced which are indispensable to understand this student scientific report. It briefly deals with the basic concepts of fracture and composite mechanics, and furthermore, introduces one of the most distinctive form of damages in fiber reinforced polymer composites.

1.1 Basics of fracture mechanics

In agreement with the linear elastic fracture mechanics approach, the given cracked body is essentially linear elastic. Crack initiation and propagation is governed by the so-called "energy release rate". According to the formulation, the energy release rate is the change in the total potential energy Π of the linear elastic system with respect to the inceremental increase in the crack area dA:

$$G = -\frac{d\Pi}{dA} \,. \tag{1.1}$$

The total potential energy in a given elastic body is defined as:

$$\Pi = U - W, \tag{1.2}$$

where U is the sum of the stored elastic strain energy and W is the work of external forces [2, 6]. This energy based definition, which was originally propesed by Irwin in 1956, supplementing with the Griffith's criterion is already suitable to handle the existing singularity

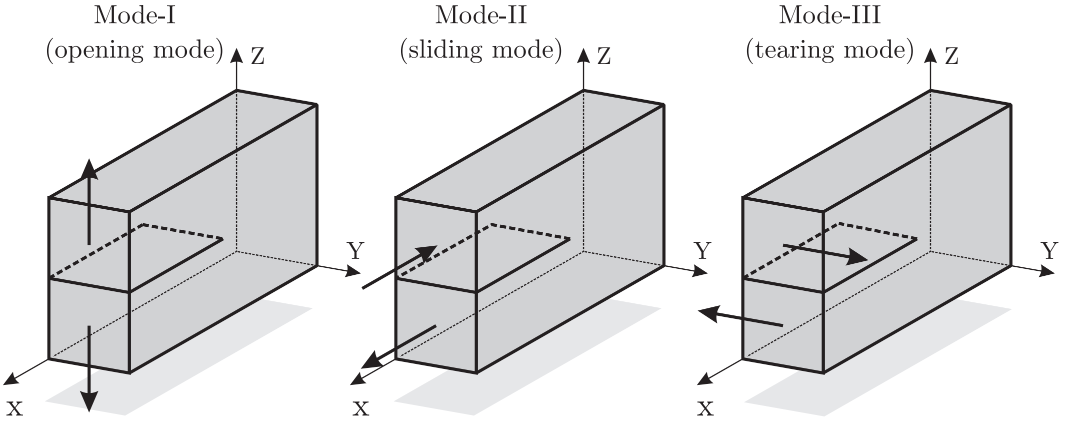

FIGURE 1.1: Basic fracture modes in linear elastic fracture mechanics.

nature of the stress field in the small vicinity of crack tips. According to the Griffith's criterion, crack initiation, or propagation can occur only if the energy release rate reaches the G_c critical value. Similarly to the Young's modulus or Poisson's ratio, it can be discussed and handled as a material property [2]. For the determination of G_c some experimentally recorded quantities, such as critical load and displacement is necessary. The three basic fracture modes are shown in Figure 1.1. In case of mode-I, where the principal load is applied normal to the crack plane, the crack tends to open. By applying forces parallel to the crack plane sliding can appear. It is mode-II. Mode-III refers to out-of-plane shear causing some kind of tearing. A cracked body can be loaded in any of these modes, or a combination of two or three modes [6].

1.2 Delamination in composite structures

Composites are multicomponent, multiphase, inhomogeneous materials consisting of high strength, high modulus reinforcement phase and tough but stiff matrix phase. Strong adhesion between the two phases, which remains relaiable even at high strains and stresses, is essential [12]. A typical tensile test of polymer composite and its components are depicted by Figure 1.2. As can be seen, the breaking strength of the composite becomes much higher than the original matrix has, furthermore, the breaking strain is mainly determined by the fiber reinforcement causing significant increase of the Young's modulus. One of the main advantages, beside the high strength despite low density, is that load bearing capacity can be fitted to the loading direction. This type of materials has uniquely tailorable mechanical properties, not to mention some other functional and operational benefits, like corrosion, chemical and fatigue resistance [12]. However, composite materials are susceptible to various and quite complicated failure mechanism, as well. As it is illustrated by Figure 1.2, fiber rupture, matrix cracking, fiber pull-out, fiber-matrix de-bonding, excessive matrix deformation and among others, due to the weakening of interface layer between the laminated plies, interlaminar fracture or delamination can occur, which is the main object of this report [6, 12]. This unavoidable and critical interlaminar failure behavior inspires us to find mechanical models to describe and, if it is possible, delay or prevent delamination in order to increase the life and load bearing capability of the laminated structures.

Application of linear fracture mechanics is one of the possible way of describing delaminated structures. The previously introduced G_c critical energy release rate value is applicable to characterize the interface layer between two composite plies.

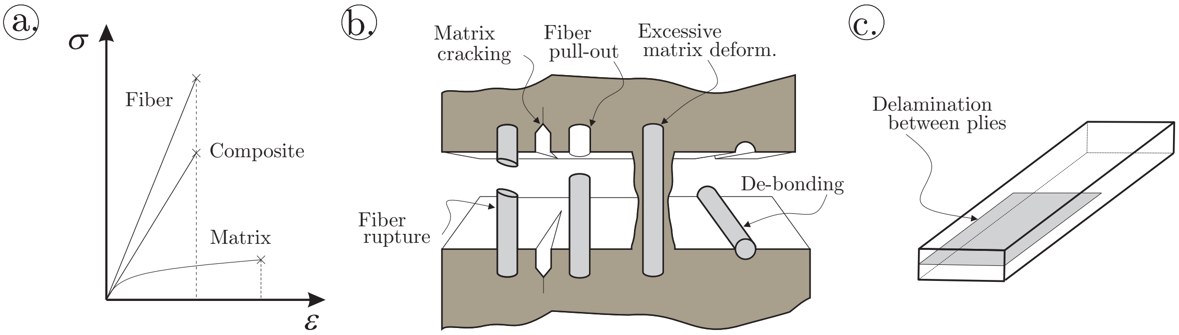

FIGURE 1.2: Tensile test of polymer composite and its components (a). Possible failure mechanism of composite materials (b-c).

1.3 Main aims and analysis methods

As it was already mentioned, application of linear elastic fracture mechanics makes possible to describe and characterize a given interface strength between two composite plies by using G_c value. Similarly to metals, in order to determine this material parameter and to investigate the failure process in composites, experimental investigations have to be performed. Generally, the fracture tests are carried out on different type of pre-cracked specimens including mode-I, mode-II, mixed-mode I/II, mode-III, mixed-mode I/III, mixed-mode II/III and mixed-mode I/II/III test by utilizing basic geometries like beams and plates [5, 6]. However, in order to determine the energy relase rate, mechanical model has to be applied.

Previously, in the literature, many models were developed based on Euler-Bernoulli hypothesis. According to this hypothesis, the cross sections of the beam are assumed to remain planar and normal to the tangent of beam flexure. Thus, the assumed dipslacement vector field can be written in the following form:

$$\boldsymbol{u}(x,z) = \begin{pmatrix} u \\ 0 \\ w \end{pmatrix}, \qquad u(x,z) = u_0(x) - z\frac{\partial w}{\partial x}, \qquad w(x) = w_0(x), \tag{1.3}$$

where there are two independent parameters: u_0 is the membrane displacement and w is the tranverse deflection of the bent beam. The rotation of the cross section, as it is illustrated by Figure 1.3, is approximated by the derivative of the deflection. However, using this theorem, the effect of shearing force cannot be taken into account.
To solve this contradiction and to increase the accuracy of beam models researchers were encouraged and inspired to introduce novel, higher order beam theorems. The first-order shear deformable beam theory (FSDT) assumes independent $\theta(x)$ rotation about the Y axes:

$$\boldsymbol{u}(x,z) = \begin{pmatrix} u \\ 0 \\ w \end{pmatrix}, \qquad u(x,z) = u_0(x) + \theta(x)z, \qquad w(x) = w_0(x). \tag{1.4}$$

By generalization of the FSDT displacement field in thickness direction the higher-order theories, secon- and third-order shear deformabe theories (SSDT-TSDT), can be obtained:

$$u(x,z) = u_0(x) + \theta(x)z + \phi(x)z^2 + \lambda(x)z^3..., \tag{1.5}$$

where $\theta(x)$ denotes the angle of rotation (or first-order term), $\phi(x)$ represents the second-order term (SSDT) and $\lambda(x)$ describes the third-order term (TSDT). The assumed displacement field in each theory is also shown in Figure 1.3.

In the following, by utilizing the basic ideas of higher-order beam theories, novel beam theories are developed and used to decribe the displacement and stress field more accurately around the cract tip in delaminated composite specimens. Using the concepts of semi-layerwise plate model [5], the so-called semi-layerwise beam model is defined and used to predict mechanical behavior of delaminated composite beams in the case of mode-I, mode-II and mixed-mode I/II interlaminar fracture conditions. In order to calculate the energy release rate and to separate it into mode-I and mode-II parts, the J-integral is applied. Using the definition of this integral and by decomposing the calculated strain and stress fields

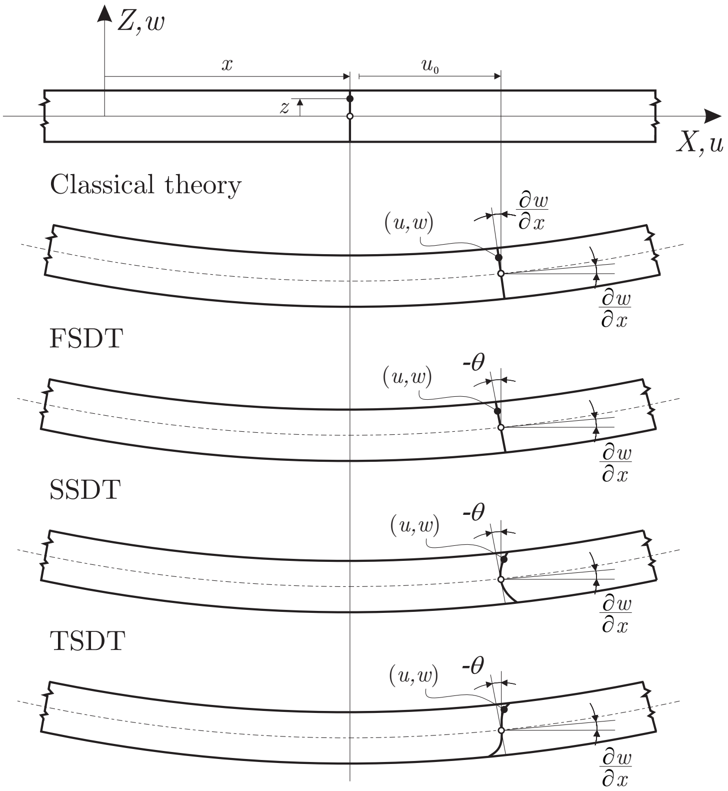
Z, w
x
u_0
z
X, u
Classical theory
(u,w)
$\frac{\partial w}{\partial x}$
$\frac{\partial w}{\partial x}$
FSDT
(u,w)
$-\theta$
$\frac{\partial w}{\partial x}$
SSDT
(u,w)
$-\theta$
$\frac{\partial w}{\partial x}$
TSDT
(u,w)
$-\theta$
$\frac{\partial w}{\partial x}$

FIGURE 1.3: The deformation of material line of a beam on the x - z plane in accordance with the different beam theories.

into symmetric and antisymmetric parts with respect to the delamination plane, more accurate and exact mode partitioning becomes achievable compared to the previously published solutions in the litarature, which are mostly based on Euler-Bernoulli beam theory.

1.4 Orthotropic and transversely isotropic materials

One of the main advantages of using composite materials is that these materials have uniquely tailorable material properties. Using different lay-up sequences and designs the load-bearing capacity can be modified in each directions, thus obtaining generally anisotropic materials. By writting the $\boldsymbol{\sigma}$ stress and $\boldsymbol{\varepsilon}$ strain tensors into vectorial forms, the Hooke's law can be formulated as:

$$\boldsymbol{\sigma} = \boldsymbol{C}\boldsymbol{\varepsilon} \quad or \quad \boldsymbol{\varepsilon} = \boldsymbol{S}\boldsymbol{\sigma}, \qquad \boldsymbol{S}^{-1} = \boldsymbol{C}, \qquad \boldsymbol{S}^{T} = \boldsymbol{S}, \tag{1.6}$$

where $\boldsymbol{C}$ is the stiffnes matrix and $\boldsymbol{S}$ is the compliance matrix. These are full 6x6 matrices, but they are symmetric, as well, requiring 21 engineering constants and describing several coupling between different deformations [3].

Nevertheless, if we look at only one ply in its own material coordinate system, it mostly behaves like orthotropic and transversely isotropic material which significantly reduces the necessary number of material constants. In the case of orthotropic material behavior, as it is illustrated by Figure 1.4, there are three mutually orthogonal material planes. An important feature of orthotropic material behavior is that there is no coupling between simple tensions and shears. If σ_1 is applied in X_1 direction, then shear strain does not appear. The number of independent constants is reduced to 9, and $\boldsymbol{S}$ compliance matrix can be written in the following form:

$$\boldsymbol{S}=\begin{bmatrix} 1/E_{11} & -\nu_{21}/E_{22} & -\nu_{31}/E_{33} & 0 & 0 & 0\\ -\nu_{12}/E_{11} & 1/E_{22} & -\nu_{32}/E_{33} & 0 & 0 & 0\\ -\nu_{13}/E_{11} & -\nu_{23}/E_{22} & 1/E_{33} & 0 & 0 & 0\\ 0 & 0 & 0 & 1/G_{23} & 0 & 0\\ 0 & 0 & 0 & 0 & 1/G_{13} & 0\\ 0 & 0 & 0 & 0 & 0 & 1/G_{12} \end{bmatrix}, \tag{1.7}$$

where $E_{11}, E_{22}, E_{33}, G_{12}, G_{13}, G_{23}, \nu_{12}, \nu_{13}, \nu_{23}$ denote the necessary engineering constants [3].

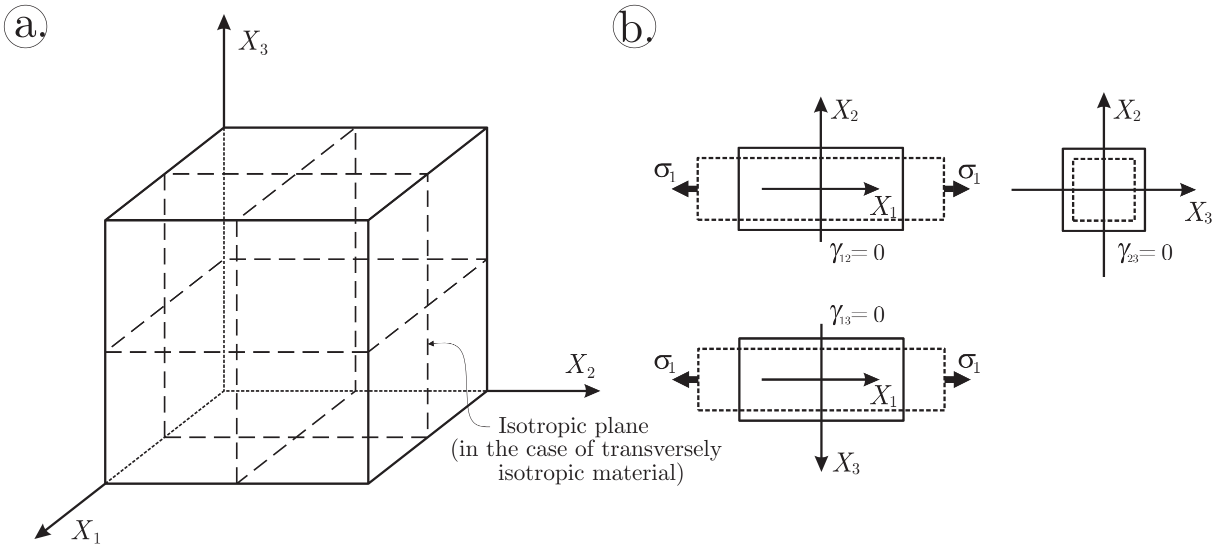

FIGURE 1.4: The material symmetry planes (a) and tension without any tension-shear coupling (b).

The next level of material symmetry is the tranversely isotropic material, which has 5 independent constants. Supposing this kind of material behavior requires that one of the three material symmetry planes has to be isotropic plane, as well. Is is also depicted in Figure 1.4. The stress-strain relation for a tranversely isotropic material takes the form:

$$\boldsymbol{S}=\begin{bmatrix} 1/E_{11} & -\nu_{21}/E_{22} & -\nu_{21}/E_{22} & 0 & 0 & 0\\ -\nu_{12}/E_{11} & 1/E_{22} & -\nu_{32}/E_{22} & 0 & 0 & 0\\ -\nu_{12}/E_{11} & -\nu_{23}/E_{22} & 1/E_{22} & 0 & 0 & 0\\ 0 & 0 & 0 & 2(1+\nu_{23})/E_{22} & 0 & 0\\ 0 & 0 & 0 & 0 & 1/G_{13} & 0\\ 0 & 0 & 0 & 0 & 0 & 1/G_{13} \end{bmatrix}, \tag{1.8}$$

where the independent contans according to the Figure 1.4 are $E_{11}, E_{22}, G_{13}, \nu_{12}, \nu_{23}$ [3].

1.4.1 Plane stress reduced constitutive relations

According to [1], in case of beams and plates, which are modeled by using their middle plane, plane-stress condition can be assumed. The stress-strain relations of an orthotropic body in plane stress state can be written as:

$$\begin{pmatrix} \sigma_1 \\ \sigma_2 \\ \tau_{12} \end{pmatrix} = \begin{bmatrix} E_{11}/(1-\nu_{21}\nu_{12}) & \nu_{21}E_{11}/(1-\nu_{21}\nu_{12}) & \\ \nu_{12}E_{22}/(1-\nu_{21}\nu_{12}) & E_{22}/(1-\nu_{21}\nu_{12}) & \\ 0 & 0 & G_{12} \end{bmatrix} \begin{pmatrix} \varepsilon_1 \\ \varepsilon_2 \\ \gamma_{12} \end{pmatrix}, \tag{1.9}$$

furthermore, $\sigma_3 = \tau_{13} = \tau_{23} = 0$. In case of beam, only one term remains:

$$\sigma_1 = \frac{E_{11}}{(1-\nu_{21}\nu_{12})}\varepsilon_1. \tag{1.10}$$

A quite important property of the higher-order beam (and plate) theories is that by taking into account tranverse shear stress does not disturb the plane stress assumptions of the stress field. The appearing shear effect is treated separately from these conditions. Referring again to [1], and as it is shown by Figure 1.5, the transverse shear stress is calculated as an additional stress term:

$$\tau_{13} = G_{13}\gamma_{13} \tag{1.11}$$

Although, applying numerical modelling, by e.g. plane elements, beams are generally not modelled by their middle plane. Instead of that, the $X_1 - X_3$ plane is used to describe the stress field by using plane stress conditions, again.

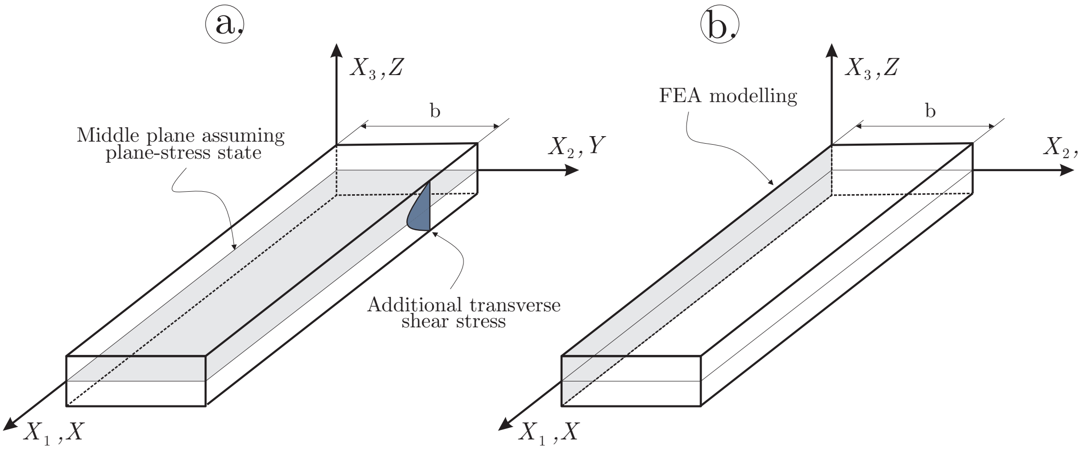
a.
X_3, Z
b
Middle plane assuming plane-stress state
X_2, Y
Additional transverse shear stress
X_1, X
b.
X_3, Z
FEA modelling
b
X_2, Y
X_1, X

FIGURE 1.5: Comaprison of the analytical (a) and numerical FEA modell (b) of the problem.

For the sake of simplicity, in the remaining discussion the material (X_1, X_2, X_3) coordinates and the global (X, Y, Z) coordinates are exactly the same.

Chapter 2

The basic equations of delaminated composite beams

In this chapter the basic equations of delaminated composite beams are presented. The formulations are based on the so-called "semi-layerwise" modeling technique [5]. The invariant form of the equilibrium equations, separately for the delaminated and undelaminated portion, are derived by using the virtual work principle [1].

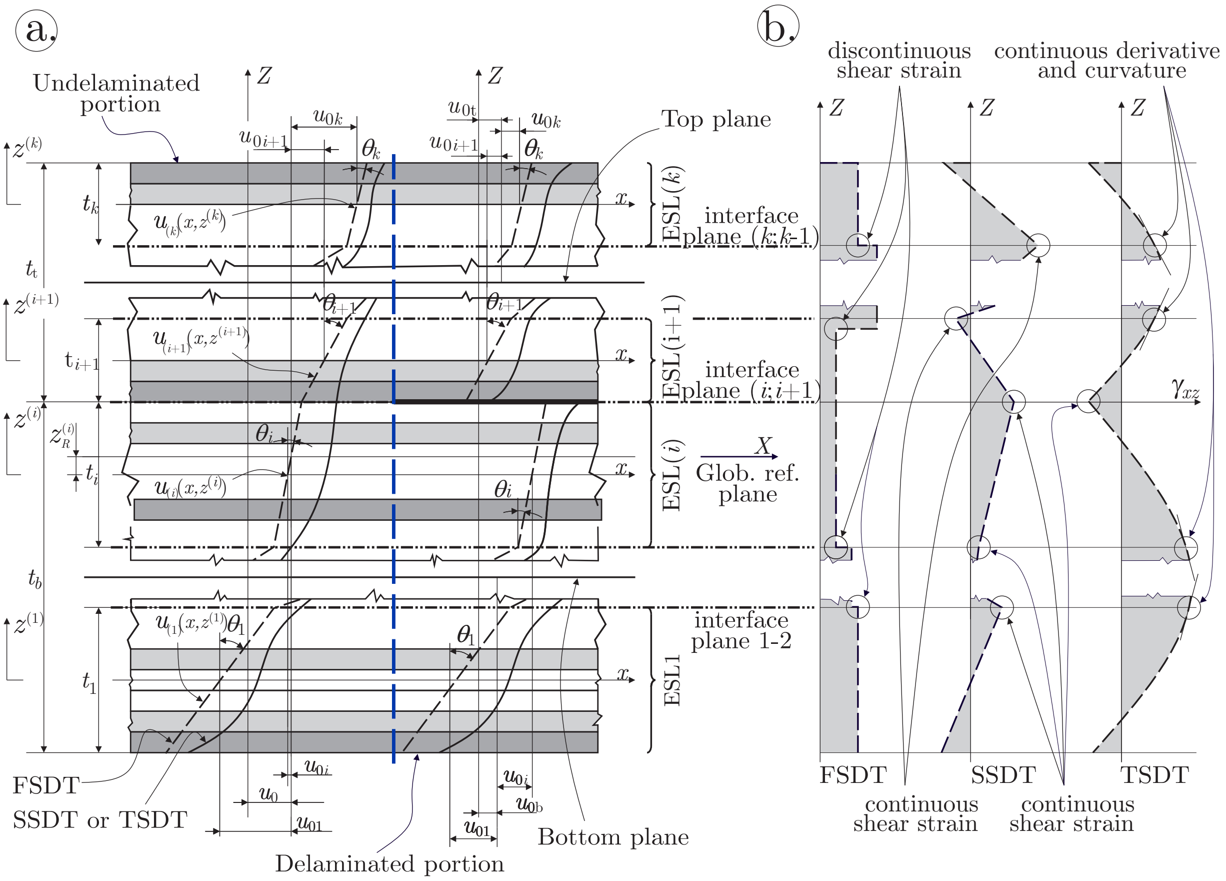
a.
b.
Undelaminated portion
Top plane
Bottom plane
Delaminated portion
Z
x
X
Glob. ref. plane
u_{0k}
u_{0t}
u_{0i+1}
θ_k
θ_{i+1}
θ_i
θ_1
$z^{(k)}$
$z^{(i+1)}$
$z^{(i)}$
$z^{(1)}$
$z_R^{(i)}$
t_k
t_t
t_{i+1}
t_i
t_b
t_1
$u_{(k)}(x,z^{(k)})$
$u_{(i+1)}(x,z^{(i+1)})$
$u_{(i)}(x,z^{(i)})$
$u_{(1)}(x,z^{(1)})$
u_{0i}
u_0
u_{01}
u_{0b}
ESL(k)
ESL(i+1)
ESL(i)
ESL1
interface plane (k:k-1)
interface plane (i:i+1)
interface plane 1-2
FSDT
SSDT or TSDT
discontinuous shear strain
continuous derivative and curvature
continuous shear strain
continuous shear strain
γ_{xz}
FSDT
SSDT
TSDT

FIGURE 2.1: Cross sections and deformation of the top and bottom beam elements of a delaminated beam in the $X - Z$ plane (a) and distributions of the transverse shear strain by different theories (b).

2.1 Semi-layerwise beam model

As it is shown in Figure 1.2 (c), if a delamination occures in a composite beam it separates the beam into a top and bottom sub-laminates. In order to deal with this phenomena the model has to be divided into top and bottom parts, too. These parts are further divided into equivalent single layers (in the following "ESL"), which are represented by Figure 2.1. This method is the so-called "semi-layerwise" technique. According to the definition of semi-layerwise beam model, which was originally defined for composite plates, if a laminated composite beam with N_l number of layers is modelled by N_{ESL} number of equivalent single layers and $N_{ESL} < N_l$ than the model is called semi-layerwise beam model. In this case the stiffness parameters of each ESL has to be calculated with respect to the local refrence planes of the ESLs [5].

Figure 2.1 shows the transition section between the delaminated and undelaminated portions of the composite beam in the X-Z plane, as well. The transverse splitting by using blue dashed line highlights that fact the undelaminated and delaminated regions are described by different mathematical functions. The two coordinate systems are to depict the displacement parameters in the different portions, separately. The general case involves k number of ESLs applied through the whole thickness of the beam. For each and every ESL the displacement field can be written in the following form:

$$\begin{aligned} u_{(i)}(x, z^{(i)}) &= u_0(x) + u_{0i}(x) + \theta_i(x) z^{(i)} + \phi_i(x)[z^{(i)}]^2 + \lambda_i(x)[z^{(i)}]^3, \\ w_{(i)}(x) &= w_{(i)}(x), \end{aligned} \tag{2.1}$$

where i denotes the index of actual ESL, $z^{(i)}$ is the local thickness coordinate of the i^{th} ESL and always coincides with the local midplane, u_0 is the global, u_{0i} is the local membrane displacements, θ denotes the rotation of the cross section about the Y axes, ϕ means the second-order, and λ expresses the third-order terms in the assumed displacement fields. Moreover, $w_{(i)}$ represents the separate transverse deflection function. Eq. (2.1) is applied equally to the undelaminated and delmainated portions, as well. The displacement functions of FSDT and SSDT can be obtained by substituting $\phi = 0$ and $\lambda = 0$ into the Eq. (2.1), respectively. The displacement field given by Eq.(2.1) is associated to each ESL [5].

2.2 The system of exact kinematic conditions

The kinematic continuity of the displacement fields between the contiguous ESLs is specified by using the sytem of exact kinematic conditions [5]:

$$(u_{(i)}, w_{(i)})\Big|_{z^{(i)}=t_i/2} = (u_{(i+1)}, w_{(i+1)})\Big|_{z^{(i+1)}=-t_{i+1}/2}, \tag{2.2}$$

where t_i is the thickness of the specified ESL. On the other hand, it is important to highlight and indicate, $w_{(i)}$ deos not depend on $z^{(i)}$ coordinate. It means that each $w_{(i)}$ is replaced with simple w function through the all thickness. The second condition restricts the u_0 global membrane displacement at the reference plane of the actual region. If it is located in the i^{th}

layer and the coordinate of the global reference plane is z_R^i within this i^{th} coordinate system, then the condition can be written as:

$$u_{(i)}\Big|_{z^{(i)}=z_R^{(i)}} - u_0 = 0. \tag{2.3}$$

Eqs.(2.2)-(2.3) are already sufficient to develop semi-layerwise model for the FSDT. If the SSDT or TSDT is applied, then shear strain continuities at the interface planes can be or have to be introduced. In accordance with Figure 2.1(b), these conditions are expressed as:

$$\gamma_{xz(i)}\Big|_{z^{(i)}=t_i/2} = \gamma_{xz(i+1)}\Big|_{z^{(i+1)}=-t_{i+1}/2}. \tag{2.4}$$

For the TSDT theory two more types of kinematic conditions are needed to be imposed. These are the derivatives and the curvatures of the shear strain between the interfaces:

$$\frac{\partial\gamma_{xz(i)}}{\partial z^{(i)}}\Big|_{z^{(i)}=t_i/2} = \frac{\partial\gamma_{xz(i+1)}}{\partial z^{(i+1)}}\Big|_{-z^{(i+1)}=t_{i+1}/2}, \tag{2.5}$$

and:

$$\frac{\partial^2\gamma_{xz(i)}}{\partial\left(z^{(i)}\right)^2}\Big|_{z^{(i)}=t_i/2} = \frac{\partial^2\gamma_{xz(i+1)}}{\left(\partial z^{(i+1)}\right)^2}\Big|_{-z^{(i+1)}=t_{i+1}/2}. \tag{2.6}$$

These conditions can be imposed to the undelaminated and delaminated portions of the beam, as well. In Eq.(2.1) the displacement fields are modified in order to satisfy Eq.(2.2)-(2.6). By using the FSDT, SSDT and TSDT theories the displacements functions can be expressed in the following, compact form [5]:

$$u_{(i)} = u_0 + \left(K_{ij}^{(0)} + K_{ij}^{(1)}z^{(i)} + K_{ij}^{(2)}[z^{(i)}]^2 + K_{ij}^{(3)}[z^{(i)}]^3\right)\psi_j, \quad i = 1..k, \tag{2.7}$$

where K_{ij} is the displacement multiplicator matrix and related exclusively to the geometry (thicknesses of the ESLs), i refers to the ESL number, the summation index j defines the components in $\boldsymbol{\psi}_p$, which is the vector of primary parameters. Eq.(2.7) can be obtained by using parameter elimination. Certain parameters of the displacement functions can be eliminated by the previously introduced system of exact kinematic conditions. Using the remaining (primary) parameters each and every eliminated (secondary) parameters can be expressed [5]. Theoretically, selecting the necessary primary parameter is almost arbitrary, but for instance, the local membrane displacements are typically secondary, the global membrane displacements are typically primary parameters. It is important to highlight the size and elements number of the $\boldsymbol{\psi}_p$ depend on the applied theory, the number of ESLs and the number of prescribed conditions.

2.3 Virtual work principle and constitutive equations

If the displacement field is known, assuming small displacements, the strain field in an elastic beam can be obtained by the following equations:

$$\varepsilon_{x(i)} = \frac{\partial u_{(i)}}{\partial x}, \qquad \gamma_{xz(i)} = \frac{\partial u_{(i)}}{\partial z^{(i)}} + \frac{\partial w_{(i)}}{\partial x}, \tag{2.8}$$

where ε_x is the normal strain in the x-direction, and γ_{xz} is the shear strain. Thus, the strains become:

$$\varepsilon_{x(i)} = \varepsilon^{(0)}_{x(i)} + z^{(i)} \cdot \varepsilon^{(1)}_{x(i)} + [z^{(i)}]^2 \cdot \varepsilon^{(2)}_{x(i)} + [z^{(i)}]^3 \cdot \varepsilon^{(3)}_{z(i)}, \tag{2.9}$$

and:

$$\gamma_{xz(i)} = \gamma^{(0)}_{xz(i)} + z^{(i)} \cdot \gamma^{(1)}_{xz(i)} + [z^{(i)}]^2 \cdot \gamma^{(2)}_{xz(i)}. \tag{2.10}$$

To derive the governing equations the virtual work principle can be applied [1]:

$$\int\limits_{T_0}^{T_1} (\delta U - \delta W_F) dt = 0, \qquad \delta U = \sum_i \delta U_{(i)}, \qquad \delta W_F = \sum_i \delta W_{F(i)}, \tag{2.11}$$

where U denotes the strain energy, W_F represents the work of external forces and t is the time. The virtual strain energy of the laminated composite beam sytem for the i^{th} ESL can be expressed as:

$$\delta U_{(i)} = \int\limits_V \sigma_{(i)} : \delta\varepsilon_{(i)} dV = \int\limits_{\Omega_0} \left\{ \int\limits_0^b \int\limits_{-t_i/2}^{t_i/2} (\sigma_{x(i)}\delta\varepsilon_{x(i)} + \tau_{xz(i)}\delta\gamma_{xz(i)}) dz^{(i)} dy \right\} dx, \tag{2.12}$$

where $\sigma_{(i)}$ is the stress tensor, $\delta\varepsilon_{(i)}$ is the virtual strain tensor of the i^{th} ESL and Ω_0 denotes the domain of the beam. Taking back the strain fields into Eq.(2.12), the following can be obtained:

$$\begin{aligned} \delta U_{(i)} = \int\limits_{\Omega_0} \Bigg\{ \int\limits_0^b \int\limits_{-t_i/2}^{t_i/2} & \Big[\sigma_{x(i)} \Big(\delta\varepsilon^{(0)}_{x(i)} + y^{(i)} \cdot \delta\varepsilon^{(1)}_{x(i)} + [z^{(i)}]^2 \cdot \delta\varepsilon^{(2)}_{x(i)} + [z^{(i)}]^3 \cdot \delta\varepsilon^{(3)}_{x(i)}\Big) \\ & + \tau_{xz(i)} \Big(\delta\gamma^{(0)}_{xz(i)} + z^{(i)} \cdot \delta\gamma^{(1)}_{xz(i)} + [z^{(i)}]^2 \cdot \delta\gamma^{(2)}_{xz(i)}\Big)\Big] dz^{(i)} dy \Bigg\} dx. \end{aligned} \tag{2.13}$$

Furthermore, the constitutive equation has to be used to continue the derivation. The constitutive equation for orthotropic and transversely ispotropic materials has already been discussed in Eq.(1.10)-(1.11). As a reminder, in this student scientific report, the material coordinates and the global coordinates are exactly the same for the sake of simplicity. Thus the constitutive relations can be formulated in the following form [1]:

$$\begin{aligned}\begin{pmatrix}\sigma_x\\ \tau_{xz}\end{pmatrix}_{(i)} = \overline{\mathbf{C}}^{(m)}_{(i)} \begin{pmatrix}\varepsilon_x\\ \gamma_{xz}\end{pmatrix}_{(i)} &= \begin{bmatrix}\overline{C}_{11} & 0\\ 0 & \overline{C}_{55}\end{bmatrix}^{(m)}_{(i)} \begin{pmatrix}\varepsilon_x\\ \gamma_{xz}\end{pmatrix}_{(i)}\\ &= \begin{bmatrix}E_{11}/(1-\nu_{21}\nu_{12}) & 0\\ 0 & G_{13}\end{bmatrix}^{(m)}_{(i)} \begin{pmatrix}\varepsilon_x\\ \gamma_{xz}\end{pmatrix}_{(i)},\end{aligned} \tag{2.14}$$

where $\overline{\mathbf{C}}^{(m)}_{(i)}$ is the stiffness matrix of the m^{th} layer within the i^{th} ESL. By using the constitutive equations the stress resultants are calculated by integrating the stresses over the thickness of each ESL:

$$\begin{pmatrix}N_x\\ M_x\\ L_x\\ P_x\end{pmatrix}_{(i)} = \int_0^b \int_{-t_i/2}^{t_i/2} \sigma_x \begin{pmatrix}1\\ y\\ y^2\\ y^3\end{pmatrix}_{(i)} dz^{(i)} dy, \tag{2.15}$$

and:

$$\begin{pmatrix}Q_{xz}\\ R_{xz}\\ S_{xz}\end{pmatrix}_{(i)} = \int_0^b \int_{-t_i/2}^{t_i/2} \tau_{xz} \begin{pmatrix}1\\ y\\ y^2\end{pmatrix}_{(i)} dz^{(i)} dy. \tag{2.16}$$

The relationship between the strain field and the stress resultants can be determined by taking back Eqs.(2.14) and (2.9)-(2.10):

$$\begin{pmatrix}N_x\\ M_x\\ L_x\\ P_x\end{pmatrix}_{(i)} = \begin{bmatrix}A_{11} & B_{11} & D_{11} & E_{11}\\ B_{11} & D_{11} & E_{11} & F_{11}\\ D_{11} & E_{11} & F_{11} & G_{11}\\ E_{11} & F_{11} & G_{11} & H_{11}\end{bmatrix}_{(i)} \begin{pmatrix}\varepsilon^{(0)}\\ \varepsilon^{(1)}\\ \varepsilon^{(2)}\\ \varepsilon^{(3)}\end{pmatrix}_{(i)}, \tag{2.17}$$

$$\begin{pmatrix}Q_{xy}\\ R_{xy}\\ S_{xy}\end{pmatrix}_{(i)} = \begin{bmatrix}A_{55} & B_{55} & D_{55}\\ B_{55} & D_{55} & E_{55}\\ D_{55} & E_{55} & F_{55}\end{bmatrix}_{(i)} \begin{pmatrix}\gamma^{(0)}_{xy}\\ \gamma^{(1)}_{xy}\\ \gamma^{(2)}_{xy}\end{pmatrix}_{(i)}, \tag{2.18}$$

where $N_{x(i)}$ denotes the normal force, $M_{x(i)}$ represents the bending moment, $Q_{x(i)}$ is the transverse shear force, and finally $L_{x(i)}$, $P_{x(i)}$, $R_{x(i)}$, $S_{x(i)}$ are the higher-order stress resultants [5]. In Eqs.(2.17)-(2.18) $A_{pp(i)}$ is the extensional, $B_{pp(i)}$ is the coupling, $D_{pp(i)}$ is the bending, $E_{pp(i)}$, $F_{pp(i)}$, $G_{pp(i)}$ and $H_{pp(i)}$ are higher-order stiffnesses defines as:

$$(A_{pp}, B_{pp}, D_{pp}, E_{pp}, F_{pp}, G_{pp}, H_{pp})_{(i)} = \sum_{m=1}^{N_{l(i)}} \int_0^b \int_{y_m^{(i)}}^{y_{m+1}^{(i)}} \overline{C}^{(m)}_{pp} (1, z, z^2, z^3, z^4, z^5, z^6)^{(i)} dz^{(i)} dy, \tag{2.19}$$

where $N_{l(i)}$ is the number of layers within i^{th} ESL [5]. The stiffnesses above have to be calculated with respect to the local reference planes for each ESL. Thus, obtaining:

$$
\begin{aligned}
A_{pp(i)} &= b\sum_{m=1}^{N_{l(i)}} \overline{C}_{pp}^{(m)}(z_{m+1}^{(i)} - z_m^{(i)}), & B_{pp(i)} &= b\frac{1}{2}\sum_{m=1}^{N_{l(i)}} \overline{C}_{pp}^{(m)}([z_{m+1}^{(i)}]^2 - [z_m^{(i)}]^2),\\
D_{pp(i)} &= b\frac{1}{3}\sum_{m=1}^{N_{l(i)}} \overline{C}_{pp}^{(m)}([z_{m+1}^{(i)}]^3 - [z_m^{(i)}]^3), & E_{pp(i)} &= b\frac{1}{4}\sum_{m=1}^{N_{l(i)}} \overline{C}_{pp}^{(m)}([z_{m+1}^{(i)}]^4 - [z_m^{(i)}]^4),\\
F_{pp(i)} &= b\frac{1}{5}\sum_{m=1}^{N_{l(i)}} \overline{C}_{pp}^{(m)}([z_{m+1}^{(i)}]^5 - [z_m^{(i)}]^5), & G_{pp(i)} &= b\frac{1}{6}\sum_{m=1}^{N_{l(i)}} \overline{C}_{pp}^{(m)}([z_{m+1}^{(i)}]^6 - [z_m^{(i)}]^6),\\
H_{pp(i)} &= b\frac{1}{7}\sum_{m=1}^{N_{l(i)}} \overline{C}_{pp}^{(m)}([z_{m+1}^{(i)}]^7 - [z_m^{(i)}]^7), & & p = 1 \ \ or \ \ 5,
\end{aligned}
\quad , \tag{2.20}
$$

where b is the beam width, z_m^i and z_{m+1}^i are the local bottom and top coordinates of the m^{th} layer in the i^{th} ESL [1]. By using the stress resultants by Eqs.(2.17)-(2.18) and the virtual strains the virtual strain energy of the i^{th} ESL becomes:

$$
\begin{aligned}
\delta U_{(i)} = \int\limits_{\Omega_0} \Bigg\{ & N_{x(i)}\delta\varepsilon_{x(i)}^{(0)} + M_{x(i)}\delta\varepsilon_{x(i)}^{(1)} + L_{x(i)}\delta\varepsilon_{x(i)}^{(2)} + P_{x(i)}\delta\varepsilon_{x(i)}^{(3)}\\
& + Q_{xz(i)}\delta\gamma_{xz(i)}^{(0)} + R_{xz(i)}\delta\gamma_{xz(i)}^{(1)} + S_{xz(i)}\delta\gamma_{xz(i)}^{(2)}\Big)\Bigg\} dx.
\end{aligned}
\tag{2.21}
$$

To transform Eq.(2.21) further the chain rule and the divergence theorem can be used [1]:

$$
N_x\frac{\partial(\delta u_0)}{\partial x} = \frac{\partial(N_x\delta u_0)}{\partial x} - \frac{N_x}{\partial x}\delta u_0 ..., \ \int_\Omega \frac{\partial(N_x\delta u_0)}{\partial x} d\Omega = \oint_\Gamma n_x(N_x\delta u_0)ds..., \ etc. \tag{2.22}
$$

Finally, the following can be written:

$$
\begin{aligned}
\delta U_{(i)} = \int\limits_{\Omega_0} \Bigg\{ & - N_{x(i),x}\delta u_0 - N_{x(i),x}K_{ij}^{(0)}\delta\psi_{(x)j} - M_{x(i),x}K_{ij}^{(1)}\delta\psi_{(x)j}\\
& - L_{x(i),x}K_{ij}^{(2)}\delta\psi_{(x)j} - P_{x(i),x}K_{ij}^{(3)}\delta\psi_{(x)j} + Q_{x(i),x}K_{ij}^{(1)}\delta\psi_{(x)j}\\
& + R_{x(i),x}K_{ij}^{(2)}\delta\psi_{(x)j} + S_{x(i),x}K_{ij}^{(3)}\delta\psi_{(x)j} - Q_{x(i),x}\delta v \Bigg\} dx\\
+ \int\limits_{\Gamma_\sigma} \Bigg\{ & + N_{x(i)}n_{x(i)}\delta u_0 + N_{x(i)}n_{x(i)}K_{ij}^{(0)}\delta\psi_{(x)j} + M_{x(i)}n_{x(i)}K_{ij}^{(1)}\delta\psi_{(x)j}\\
& + L_{x(i)}n_{x(i)}K_{ij}^{(2)}\delta\psi_{(x)j} + P_{x(i)}n_{x(i)}K_{ij}^{(3)}\delta\psi_{(x)j} + Q_{x(i)}n_{x(i)}K_{ij}^{(1)}\delta\psi_{(x)j}\\
& + R_{x(i)}n_{x(i)}K_{ij}^{(2)}\delta\psi_{(x)j} + S_{x(i)}n_{x(i)}K_{ij}^{(3)}\delta\psi_{(x)j} + Q_{x(i)}n_{x(i)}\delta v \Bigg\} dx,
\end{aligned}
\tag{2.23}
$$

where the comma means differentiation. The first term in the Eq.(2.23) is the virtual strain energy related to the volume domain of the ESL, the second term represents the boundary conditions. Finally, the virtual work of the external forces for single ESL is:

$$\delta W_{F(i)} = \int_{\Omega_0} \left\{ q_{b(i)}(x)\delta w(x, -t_i/2) + q_{t(i)}(x)\delta w(x, t_i/2) \right\} dx, \tag{2.24}$$

where q_b and q_t are the distributed loads on the top and bottom parts of the i^{th} ESL. The equilibrium equations can be obtained by setting the coefficient of virtual displacement parameteres in the virtual work expression Eq.(2.11) using Eqs.(2.23) and (2.24) on the domain Ω_0 equal to zero. [1, 5]. The equilibrium equations, separately for undelaminated and delaminated portions, are discussed in the further subsections.

2.4 Equilibrium equations - Invariant form

In the sequel the equilibrium equations are detailed separately for the undelaminated and delaminated regions.

2.4.1 Undelaminated region

By setting the sum of coefficients for the virtual membrane displacement δu_0, primary parameters $\delta\psi_j$ and the deflection δw in Eq.(2.11) to zero by using Eqs:(2.23)-(2.24) leads to three types of equilibrium equations. By using normal stress resultants, the form of equilibrium equation becomes absolutely independent of the above mentioned theories (FSDT, SSDT, TSDT). Each and every case it can be written as:

$$\delta u_0 : \sum_{i=1}^{k} \left(\frac{\partial N_{x(i)}}{\partial x} \right) = 0, \tag{2.25}$$

where k is the total number of ESLs. Although, the definition of the normal forces are not independent of the applied theory referring to Eq.(2.17). Generally, using any higher order theory, the number of primary parameters (ignoring the global membrane displacements) in the displacement field is r, which is equal to the number of elements in $\boldsymbol{\psi_p}$. By collecting the coefficients of the virtual primary displacements parameters in Eq.(2.11) and make them equal to zero the following equations can be read out:

$$\begin{aligned} \delta\psi_j : \sum_{i=1}^{k} \Bigg(& K_{ij}^{(0)} \frac{\partial N_{x(i)}}{\partial x} + K_{ij}^{(1)} \frac{\partial M_{x(i)}}{\partial x} + K_{ij}^{(2)} \frac{\partial L_{x(i)}}{\partial x} + K_{ij}^{(3)} \frac{\partial P_{x(i)}}{\partial x} - \\ & K_{ij}^{(1)} Q_{x(i)} - 2K_{ij}^{(2)} R_{x(i)} - 3K_{ij}^{(3)} S_{x(i)} \Bigg) = 0, \end{aligned} \tag{2.26}$$

where ψ_j denotes the primary parameters and $j = 1..q$. Similarly to the normal force equlibrium, by collecting the coefficients of the $\delta w(x)$ beam deflection and setting their sum to zero in Eq.(2.11) leads to:

$$\delta w : \sum_{i=1}^{k} \left(\frac{\partial Q_{x(i)}}{\partial x} \right) + q = 0, \tag{2.27}$$

where q is the external distributed force along the beam:

$$q=\sum_{i=1}^{k}\left(q_{b(i)}+q_{t(i)}\right)=0. \tag{2.28}$$

This form is also idependent of the applied theory, although, definition of the shear forces are not, referring to Eq.(2.18).

The previous equations define the invariant form of the equilibrium equations. Using any theory and any number of layers, by calculating K_{ij} displacement multiplicator matrix elements and defining $\boldsymbol{\psi}_p$ vector of primary parameters, expression of the equilibrium equations is possible [5].

2.4.2 Delaminated region

The delaminated regions consist of a top and a bottom beam. Each of them is modeled by further ESLs. The most essential difference between the delaminated and undelaminated plate regions is that in the delaminated region the displacements are not connected to each other at the delaminated plane. Therefore, the global membrane displacement u_0 is replaced by u_{0b} for ESLs of the bottom plate, moreover, by u_{0t} for the ESLs of the top plate in Eq.(2.7):

$$\begin{aligned}
u_{(i)}&=u_{0b}+\left(K_{ij}^{(0)}+K_{ij}^{(1)}y^{(i)}+K_{ij}^{(2)}[y^{(i)}]^2+K_{ij}^{(3)}[y^{(i)}]^3\right)\psi_j, \quad i=1..h,\\
u_{(i)}&=u_{0t}+\left(K_{ij}^{(0)}+K_{ij}^{(1)}y^{(i)}+K_{ij}^{(2)}[y^{(i)}]^2+K_{ij}^{(3)}[y^{(i)}]^3\right)\psi_j, \quad i=h+1..k,
\end{aligned} \tag{2.29}$$

where h is the number of ESLs in the bottom beam and j is a summation index. Furthermore, the w tranverse deflection is also separated into bottom and top deflections:

$$\begin{aligned}
w_{(i)}&=w_b, \quad i=1..h,\\
w_{(i)}&=w_t, \quad i=h+1..k.
\end{aligned} \tag{2.30}$$

As a consequence, the equilibrium equations of the normal forces and the transverse forces get separated from each other:

$$\delta u_{0b}:\sum_{i=1}^{h}\left(\frac{\partial N_{x(i)}}{\partial x}\right)=0, \qquad \delta u_{0t}:\sum_{i=h+1}^{k}\left(\frac{\partial N_{x(i)}}{\partial x}\right)=0, \tag{2.31}$$

$$\delta w_b:\sum_{i=1}^{h}\left(\frac{\partial Q_{x(i)}}{\partial x}\right)+q_b=0, \quad \delta w_t:\sum_{i=h+1}^{k}\left(\frac{\partial Q_{x(i)}}{\partial x}\right)+q_t=0. \tag{2.32}$$

The form of the other equilibrium equations, of course with different K_{ij} displacement multiplicator matrix elements, are formulated according to Eq.(2.26).

Chapter 3

The method of four equivalent single layers

In this chapter the concept of semi-layerwise technique is utilized, separately for the undelaminated and delaminated portions. The whole laminate is modeled by 4ESLs. Two layers of the model are located above and further two below the delamination plane resulting four layers in the undelaminated part [5, 7, 8].

3.1 Undelaminated region

The concept of the method using 4ESLs in the undelaminated portion is illustrated by Figure 3.1. The displacement function is piecewise linear by FSDT, piecewise quadratic in the case of the SSDT and cubic for the TSDT. The corresponding shear strain distributions are shown in 3.1b. It is piecewise constant by FSDT, piecewise linear by SSDT and piecewise quadratic by TSDT with continuous derivatives and curvatures in the interface plane 1-2

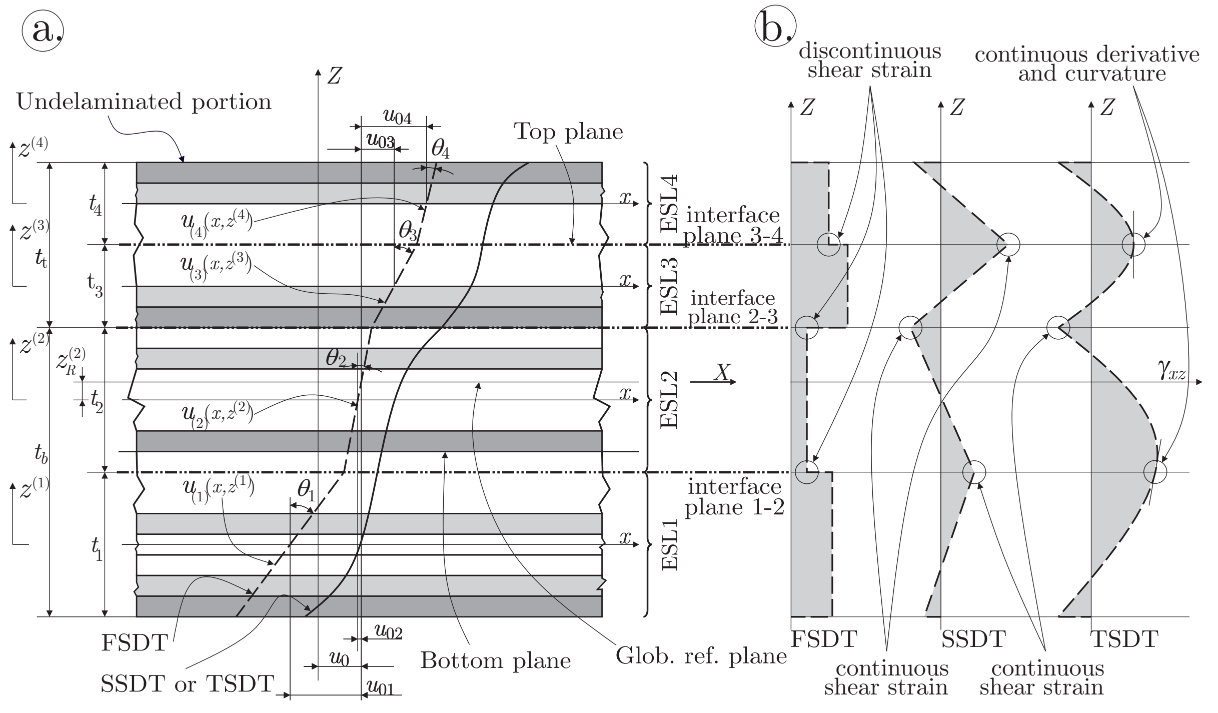
a.
b.
Undelaminated portion
Z
u_{04}
u_{03}
θ_4
Top plane
$z^{(4)}$
t_4
$u_{(4)}(x,z^{(4)})$
θ_3
x
ESL4
interface plane 3-4
$z^{(3)}$
t_t
t_3
$u_{(3)}(x,z^{(3)})$
ESL3
interface plane 2-3
$z^{(2)}$
$z_R^{(2)}$
θ_2
t_2
X
$u_{(2)}(x,z^{(2)})$
ESL2
t_b
$z^{(1)}$
$u_{(1)}(x,z^{(1)})$
θ_1
interface plane 1-2
t_1
ESL1
FSDT
SSDT or TSDT
u_{02}
u_0
u_{01}
Bottom plane
Glob. ref. plane
discontinuous shear strain
continuous derivative and curvature
Z
Z
Z
γ_{xz}
FSDT
SSDT
TSDT
continuous shear strain
continuous shear strain

FIGURE 3.1: Cross section and the assumed deformation of the undelaminated portion in the $X - Z$ plane (a) and distributions of the transverse shear strain by different theories (b) using 4ESLs.

and in the interface plane 3-4 [7]. According to the Eqs.(2.2)-(2.6), the following conditions can be formulated between the 4ESLs by starting with the continuity conditions:

$$\begin{aligned}
\left(u_{(1)}, w_{(1)}\right)\Big|_{z^{(1)}=t_1/2} &= \left(u_{(2)}, w_{(2)}\right)\Big|_{z^{(2)}=-t_2/2}, \\
\left(u_{(2)}, w_{(2)}\right)\Big|_{z^{(2)}=t_2/2} &= \left(u_{(3)}, w_{(3)}\right)\Big|_{z^{(3)}=-t_3/2}, \\
\left(u_{(3)}, w_{(3)}\right)\Big|_{z^{(3)}=t_3/2} &= \left(u_{(4)}, w_{(4)}\right)\Big|_{z^{(4)}=-t_4/2}.
\end{aligned} \tag{3.1}$$

The reference plane belongs to the second ESL, therefore, the following condition is imposed referring to Eq.(2.3):

$$u_{(2)}\Big|_{z^{(2)}=z_R^{(2)}} - u_0(x) = 0, \tag{3.2}$$

where $z_R^{(2)} = 1/2(t_3 + t_4 - t_1)$ in accordance with Figure 3.1a and it gives the location of the global midplane of the model with respect to ESL2. The next set of conditions decribes the continuous shear strain at the interface plane using Eq.(2.4):

$$\begin{aligned}
\gamma_{xz(1)}\Big|_{z^{(1)}=t_1/2} &= \gamma_{xz(2)}\Big|_{z^{(2)}=-t_2/2}, \\
\gamma_{xz(2)}\Big|_{z^{(2)}=t_2/2} &= \gamma_{xz(3)}\Big|_{z^{(3)}=-t_3/2}, \\
\gamma_{xz(3)}\Big|_{z^{(3)}=t_3/2} &= \gamma_{xz(4)}\Big|_{z^{(4)}=-t_4/2}.
\end{aligned} \tag{3.3}$$

As it was previously discussed by Eqs.(2.4) and (2.5), the contiuous shear strain derivates and curvatures can be imposed in the case of TSDT at interface planes 1-2 and 3-4:

$$\begin{aligned}
\frac{\partial \gamma_{xz(1)}}{\partial z^{(1)}}\Big|_{z^{(1)}=t_1/2} &= \frac{\partial \gamma_{xz2)}}{\partial z^{(2)}}\Big|_{-z^{(2)}=t_2/2}, \\
\frac{\partial \gamma_{xz(3)}}{\partial z^{(3)}}\Big|_{z^{(3)}=t_3/2} &= \frac{\partial \gamma_{xz(4)}}{\partial z^{(4)}}\Big|_{-z^{(4)}=t_4/2},
\end{aligned} \tag{3.4}$$

and:

$$\begin{aligned}
\frac{\partial^2 \gamma_{xz(1)}}{\partial \left(z^{(1)}\right)^2}\Big|_{z^{(1)}=t_1/2} &= \frac{\partial^2 \gamma_{xz(2)}}{\left(\partial z^{(2)}\right)^2}\Big|_{-z^{(2)}=t_2/2}, \\
\frac{\partial^2 \gamma_{xz(3)}}{\partial \left(z^{(3)}\right)^2}\Big|_{z^{(3)}=t_3/2} &= \frac{\partial^2 \gamma_{xz(4)}}{\left(\partial z^{(4)}\right)^2}\Big|_{-z^{(4)}=t_4/2}.
\end{aligned} \tag{3.5}$$

If the displacement functions are modified in order to satisfy Eqs.(3.1)-(3.5) then, using FSDT, SSDT or TSDT, the displacement functions can be formulated as:

$$\begin{aligned}
u_{(i)} &= u_0 + \left(K_{ij}^{(0)} + K_{ij}^{(1)} z^{(i)} + K_{ij}^{(2)} [z^{(i)}]^2 + K_{ij}^{(3)} [z^{(i)}]^3\right) \psi_j, \quad i = 1..4 \\
w_{(i)} &= w(x), \quad i = 1..4,
\end{aligned} \tag{3.6}$$

where the matrices denoted by K_{ij} are related only to the geometry, i refers to the ESL number, the summation index j defines the component in ψ_j, which is the vector of primary parameters, and finally $w(x)$ is the tranverese deflection identical for each ESL [5].

3.1.1 Third-order beam theory

Using the above mentioned exact kinematic conditions by Eqs.3.1-3.5, 11 unknown displacement parameters can be eliminated from the original 18 parameters. The secondary parameters are: $u_{0(i)}$, $\lambda_{(i)}$ for $i = 1..4$, $\theta_{(i)}$ for $i = 1, 2$ and 4. The unknown terms and the vector of primary parameters are:

$$u_0, \quad w, \quad \boldsymbol{\psi}_p = \begin{pmatrix} \theta_3 & \phi_1 & \phi_2 & \phi_3 & \phi_4 \end{pmatrix}^T. \tag{3.7}$$

The elements of the matrices $K_{ij}^{(0)}$,$K_{ij}^{(1)}$,$K_{ij}^{(2)}$ and $K_{ij}^{(3)}$ in Eq.(3.6) are defined in Appendix A.1. The equilibrium equations can be obtained using Eqs.(2.25)-(2.27) and the vector of primary parameters from Eq.(3.7):

$$\delta u_0 : \sum_{i=1}^{k} \left(\frac{\partial N_{x(i)}}{\partial x} \right) = 0, \tag{3.8}$$

$$\begin{aligned} \delta\psi_j : \sum_{i=1}^{4} \Bigg(& K_{ij}^{(0)} \frac{\partial N_{x(i)}}{\partial x} + K_{ij}^{(1)} \frac{\partial M_{x(i)}}{\partial x} + K_{ij}^{(2)} \frac{\partial L_{x(i)}}{\partial x} + K_{ij}^{(3)} \frac{\partial P_{x(i)}}{\partial x} - \\ & K_{ij}^{(1)} Q_{x(i)} - 2K_{ij}^{(2)} R_{x(i)} - 3K_{ij}^{(3)} S_{x(i)} \Bigg) = 0, \quad j = 1..5, \end{aligned} \tag{3.9}$$

$$\delta w : \sum_{i=1}^{4} \left(\frac{\partial Q_{x(i)}}{\partial x} \right) + q = 0. \tag{3.10}$$

3.1.2 Second-order beam theory

In this case, by using similarly the exact kinematic conditions by Eqs.3.1-3.3, apart from the continuity of derivatives and curvatures, 7 unknown displacement parameters can be eliminated from the original 14 parameters. The secondary parameters are: $u_{0(i)}$, $\theta_{(i)}$ for $i = 2, 4$, $\phi_{(i)}$ for $i = 1$ and 3. The unknown terms and the vector of primary parameters are:

$$u_0, \quad w, \quad \boldsymbol{\psi}_p = \begin{pmatrix} \theta_1 & \theta_3 & \phi_1 & \phi_2 & \phi_4 \end{pmatrix}^T \tag{3.11}$$

Obviously, in this case, $K_{ij}^{(3)} = 0$. The elements of the matrices $K_{ij}^{(0)}$,$K_{ij}^{(1)}$ and $K_{ij}^{(2)}$ in Eq.(3.6) are specified by Appendix A.2. The equilibrium equations take the same form as Eqs.(2.25)-(2.27) and the vector of primary parameters from Eq.(3.11)

3.1.3 First-order beam theory

Apart from the continuity of strains and its derivatives , using similarly the exact kinematic conditions Eqs.3.1-3.2, 4 unknown displacement parameters can be eliminated from the original 10 parameters. These secondary parameters are: $u_{0(i)}$ for $i = 1, 4$. The unknown terms and the vector of primary parameters become:

$$u_0, \qquad w, \qquad \boldsymbol{\psi_p} = \begin{pmatrix} \theta_1 & \theta_2 & \theta_3 & \theta_4 \end{pmatrix}^T \tag{3.12}$$

Obviously, in this case, $K_{ij}^{(3)} = K_{ij}^{(2)} = 0$. The elements of the matrices $K_{ij}^{(0)}$ and$K_{ij}^{(1)}$ in Eq.(3.6) are defined in Appendix A.3. The equilibrium equations take the same form as Eqs.(2.25)-(2.27) associated to the vector of primary parameters from Eq.(3.12).

3.2 Delaminated region

Similarly to the previously intorduced kinematic conditions, displacement and strain conditions can be imposed at the interface planes. Although, contrary to the undelaminated case, in the delaminated region the top an bottom beams are equally modelled by 2-2ESLs. Apart from the delaminated plane, the adjacent layers are connected to each other. Thus, the delaminated regions are described by separated mathematical functions, as it is illustrated by Figure 3.2. As it is depicted in the figure, continuity conditions can be written in the

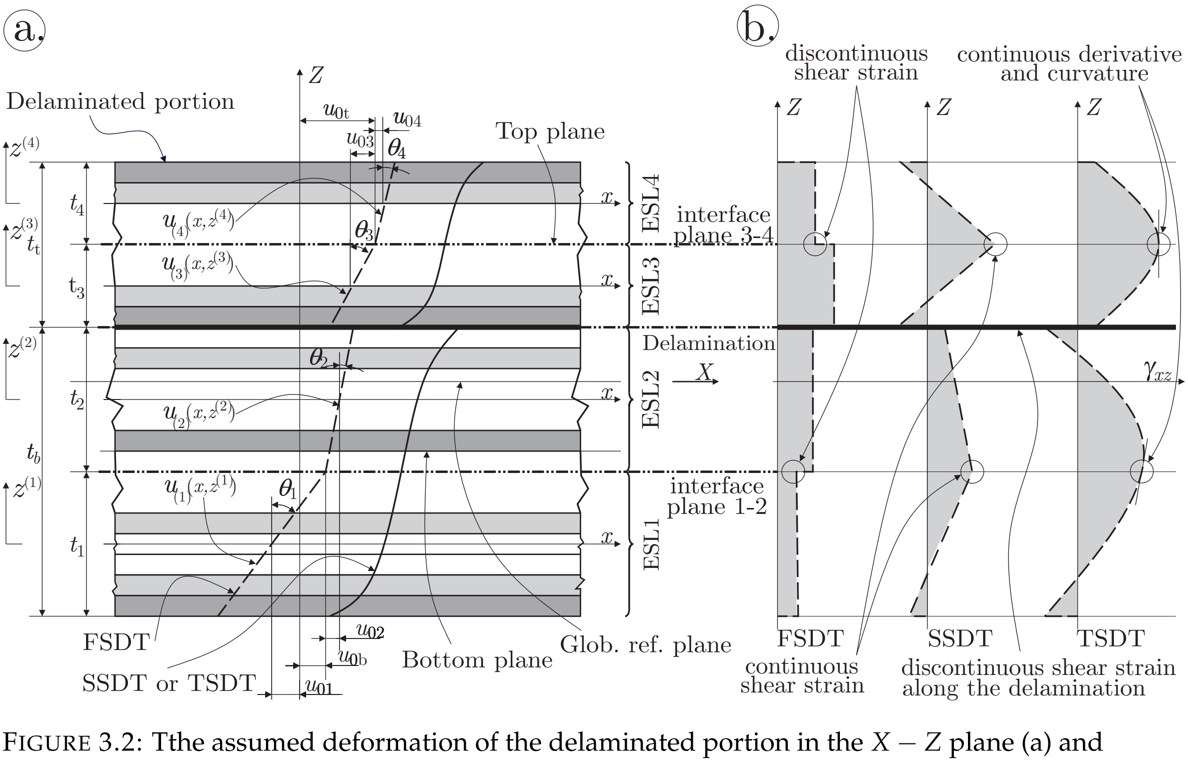
a.
b.
Delaminated portion
Z
u_{0t}
u_{04}
u_{03}
θ_4
Top plane
$z^{(4)}$
t_4
$u_{(4)}(x,z^{(4)})$
θ_3
$z^{(3)}$
t_t
t_3
$u_{(3)}(x,z^{(3)})$
x
ESL4
ESL3
interface plane 3-4
$z^{(2)}$
θ_2
Delamination
X
ESL2
t_2
$u_{(2)}(x,z^{(2)})$
t_b
$z^{(1)}$
$u_{(1)}(x,z^{(1)})$
θ_1
interface plane 1-2
t_1
ESL1
FSDT
SSDT or TSDT
u_{02}
u_{0b}
u_{01}
Bottom plane
Glob. ref. plane
discontinuous shear strain
continuous derivative and curvature
Z
γ_{xz}
FSDT
SSDT
TSDT
continuous shear strain
discontinuous shear strain along the delamination

FIGURE 3.2: Tthe assumed deformation of the delaminated portion in the $X - Z$ plane (a) and distributions of the transverse shear strain by different theories (b) using separately 2ESLs.

interface planes 1-2 and 3-4:

$$\begin{aligned}
\left(u_{(1)}, w_{(1)}\right)\Big|_{z^{(1)}=t_1/2} &= \left(u_{(2)}, w_{(2)}\right)\Big|_{z^{(2)}=-t_2/2}, \\
\left(u_{(3)}, w_{(3)}\right)\Big|_{z^{(3)}=t_3/2} &= \left(u_{(4)}, w_{(4)}\right)\Big|_{z^{(4)}=-t_4/2}.
\end{aligned} \tag{3.13}$$

The reference planes belong to the first and third ESLs:

$$\begin{aligned}
u_{(1)}\Big|_{z^{(1)}} &= t_2/2 - u_{0b}(x) = 0, \\
u_{(3)}\Big|_{z^{(3)}} &= t_4/2 - u_{0t}(x) = 0,
\end{aligned} \tag{3.14}$$

where u_{0b} and u_{0t} are the global memebrane displacements of the bottom and top sublaminates in accordance with Figure 3.2a. In the case of SSDT and TSDT, apart from the delaminated plane, shear strain continuities can be imposed also:

$$\begin{aligned}
\gamma_{xz(1)}\Big|_{z^{(1)}=t_1/2} &= \gamma_{xz(2)}\Big|_{z^{(2)}=-t_2/2}, \\
\gamma_{xz(3)}\Big|_{z^{(3)}=t_3/2} &= \gamma_{xz(4)}\Big|_{z^{(4)}=-t_4/2}.
\end{aligned} \tag{3.15}$$

Furthermore, using TSDT, continuity of the shear strain derivatives is imposed, as well:

$$\begin{aligned}
\frac{\partial \gamma_{xz(1)}}{\partial z^{(1)}}\Big|_{z^{(1)}=t_1/2} &= \frac{\partial \gamma_{xz(2)}}{\partial z^{(2)}}\Big|_{-z^{(2)}=t_2/2}, \\
\frac{\partial \gamma_{xz(3)}}{\partial z^{(3)}}\Big|_{z^{(3)}=t_3/2} &= \frac{\partial \gamma_{xz(4)}}{\partial z^{(4)}}\Big|_{-z^{(4)}=t_4/2},
\end{aligned} \tag{3.16}$$

and finally, continuity of the shear strain curvatures is ensured by:

$$\begin{aligned}
\frac{\partial^2 \gamma_{xz(1)}}{\partial \left(z^{(1)}\right)^2}\Big|_{z^{(1)}=t_1/2} &= \frac{\partial^2 \gamma_{xz(2)}}{\left(\partial z^{(2)}\right)^2}\Big|_{-z^{(2)}=t_2/2}, \\
\frac{\partial^2 \gamma_{xz(3)}}{\partial \left(z^{(3)}\right)^2}\Big|_{z^{(3)}=t_3/2} &= \frac{\partial^2 \gamma_{xz(4)}}{\left(\partial z^{(4)}\right)^2}\Big|_{-z^{(4)}=t_4/2}.
\end{aligned} \tag{3.17}$$

The displacement functions are given by the following equations:

$$\begin{aligned}
u_{(i)} &= u_{0b} + \left(K_{ij}^{(0)} + K_{ij}^{(1)} z^{(i)} + K_{ij}^{(2)} [z^{(i)}]^2 + K_{ij}^{(3)} [z^{(i)}]^3\right)\psi_j, \quad i = 1..2, \\
u_{(i)} &= u_{0t} + \left(K_{ij}^{(0)} + K_{ij}^{(1)} z^{(i)} + K_{ij}^{(2)} [z^{(i)}]^2 + K_{ij}^{(3)} [z^{(i)}]^3\right)\psi_j, \quad i = 3..4, \\
w_{(i)} &= w_b(x), \quad i = 1..2, \\
w_{(i)} &= w_t(x), \quad i = 3..4,
\end{aligned} \tag{3.18}$$

where notations, apart from the transverse deflections, are exactly the same as it in Eq.(3.6). Moreover, w_b denotes the tranverse deflection of the bottom beam and w_t represents deflection of the top beam.

3.2.1 Third-order beam theory

Utilizing the above mentioned exact kinematic conditions by Eqs.(3.13)-(3.17), 10 unknown displacement parameters can be eliminated from the 20 parameters. The secondary parameters are: $u_{0(i)}$, $\lambda_{(i)}$ for $i = 1..4$, $\theta_{(i)}$ for $i = 2$ and 4. Thus the unknown terms and the vector of primary parameters are:

$$u_{0b}, \quad u_{0t}, \quad w_b, \quad w_t, \quad \boldsymbol{\psi_p} = \begin{pmatrix} \textcircled{θ_1} & \phi_1 & \phi_2 & \theta_3 & \phi_3 & \phi_4 \end{pmatrix}^T, \tag{3.19}$$

where circle denotes the autocontinuity parameter. The role of this term will be discussed later. The elements of the matrices $K_{ij}^{(0)}$,$K_{ij}^{(1)}$,$K_{ij}^{(2)}$ and $K_{ij}^{(3)}$ in Eq.(3.18) are defined in Appendix A.1. The equilibrium equations can be obtained using the previously defined invariant forms by Eqs.(2.25)-(2.27) and the vector of primary parameters from Eq.(3.19):

$$\delta u_{0b} : \sum_{i=1}^{2} \left(\frac{\partial N_{x(i)}}{\partial x} \right) = 0, \quad \delta u_{0t} : \sum_{i=3}^{4} \left(\frac{\partial N_{x(i)}}{\partial x} \right) = 0, \tag{3.20}$$

$$\begin{aligned} \delta \psi_j : \sum_{i=1}^{4} \Bigg(& K_{ij}^{(0)} \frac{\partial N_{x(i)}}{\partial x} + K_{ij}^{(1)} \frac{\partial M_{x(i)}}{\partial x} + K_{ij}^{(2)} \frac{\partial L_{x(i)}}{\partial x} + K_{ij}^{(3)} \frac{\partial P_{x(i)}}{\partial x} - \\ & K_{ij}^{(1)} Q_{x(i)} - 2K_{ij}^{(2)} R_{x(i)} - 3K_{ij}^{(3)} S_{x(i)} \Bigg) = 0, \quad j = 1..6, \end{aligned} \tag{3.21}$$

$$\delta v_b : \sum_{i=1}^{2} \left(\frac{\partial Q_{x(i)}}{\partial x} \right) + q_b = 0, \quad \delta v_t : \sum_{i=3}^{4} \left(\frac{\partial Q_{x(i)}}{\partial x} \right) + q_t = 0. \tag{3.22}$$

3.2.2 Second-order beam theory

In the case of SSDT, using Eqs.3.13-3.15, 6 unknown displacement parameters can be eliminated from the original 14 unknown parameters. The secondary parameters are: $u_{0(i)}$, $\theta_{(i)}$ for $i = 2$ and 4. The unknown terms and the vector of primary parameters are:

$$u_{0b}, \quad u_{0t}, \quad w_b, \quad w_t, \quad \boldsymbol{\psi_p} = \begin{pmatrix} \theta_1 & \phi_1 & \phi_2 & \theta_3 & \textcircled{ϕ_3} & \phi_4 \end{pmatrix}^T \tag{3.23}$$

Obviously, in this case also, $K_{ij}^{(3)} = 0$. The elements of the matrices $K_{ij}^{(0)}$,$K_{ij}^{(1)}$ and $K_{ij}^{(2)}$ in Eq.3.18 are given in Appendix A.2. The equilibrium equations take the same form as Eqs.(2.25)-(2.27) according to the vector of primary parameters from Eq.(3.23)

3.2.3 First-order beam theory

In this case, using similarly the exact kinematic conditions by Eqs.3.13-3.14, 4 unknown displacement parameters can be eliminated from the original 12 unknown parameters. These secondary parameters are: $u_{0(i)}$ for $i = 1, 4$. The unknown terms and the vector of primary parameters are:

$$u_{0b}, \qquad u_{0t}, \qquad w_b, \qquad w_t, \qquad \boldsymbol{\psi_p} = \begin{pmatrix} \theta_1 & \theta_2 & \theta_3 & \theta_4 \end{pmatrix}^T \tag{3.24}$$

Obviously, by using FSDT, $K_{ij}^{(3)} = K_{ij}^{(2)} = 0$. The elements of the matrices $K_{ij}^{(0)}$ and $K_{ij}^{(1)}$ in Eq(3.18) are given in Appendix A.3. The equilibrium equations take the same form as Eqs.(2.25)-(2.27) associated to the vector of primary parameters from Eq.(3.24).

Chapter 4

J-integral

In this chapter the basic concepts of J-integral are introduced. From the general definition the application for 4ESLs is deduced. Finally, the separation of mechanical field parameters into symmetrical and asymmetrical components is discussed.

4.1 Basic definition

In order to analyse stress and strain concentrations in plane-problems including crack and notches the so-called "J-integral" was developed. This integral has enjoyed great success as a fracture characterizing parameter because of its advantageous properties, such as path independence and its possible application for nonlinear-elastic and even elastic-plastic problems [2]. In this report, considering only linear elastic fracture mechanics, the most important property of this integral is the following:

$$J = G_T, \tag{4.1}$$

where G_T denotes the previously defined total energy release rate by Eq.(1.1) and J represent the value of the J-integral. Considering an abitrary counterclokwise C contour around the

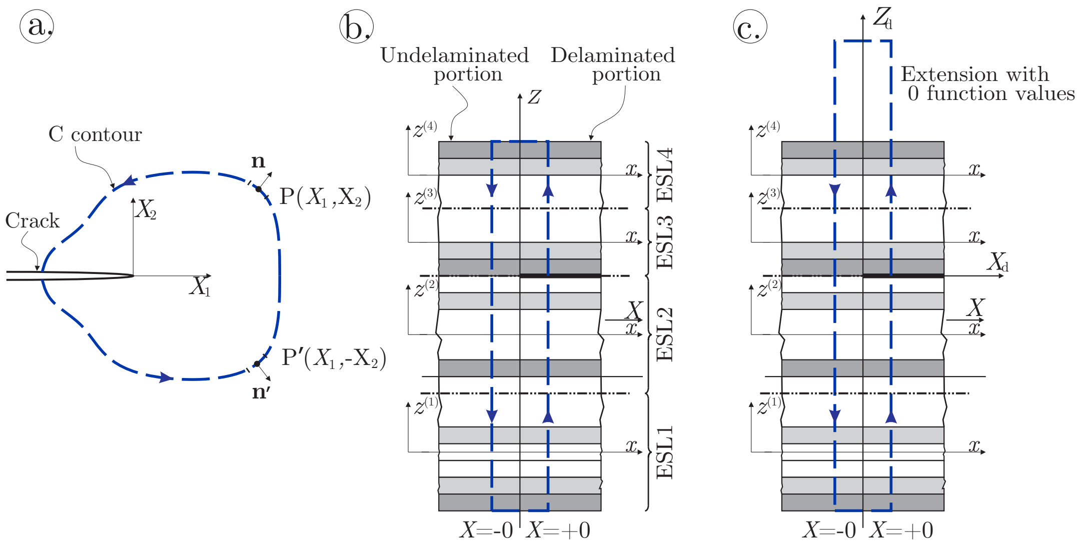
a.
C contour
Crack
n
P(X_1,X$_2$)
X_2
X_1
P′(X_1,-X$_2$)
n′
b.
Undelaminated portion
Delaminated portion
Z
$z^{(4)}$
$z^{(3)}$
$z^{(2)}$
$z^{(1)}$
x
X
ESL4
ESL3
ESL2
ESL1
X=-0
X=+0
c.
Z_d
Extension with 0 function values
X_d

FIGURE 4.1: The general defintion of the J-integral for plane problem (a). The application of the J-integral for semi-layerwise model using zero-area path(b) with the inevitable extension (c).

tip of a crack, as it is shown by Figure 4.1, the J-integral is given by:

$$
\begin{aligned}
J &= \int\limits_C \left\{ U n_1 - \sigma_{ij} n_j \frac{\partial u_i}{\partial x_1} \right\} ds \\
&= \int\limits_C \left\{ \frac{1}{2} \left(\sigma_{11}\ \sigma_{22}\ \tau_{12} \right) \begin{pmatrix} \varepsilon_{11} \\ \varepsilon_{22} \\ \gamma_{12} \end{pmatrix} n_1 - \left(\sigma_{11}\ \sigma_{22}\ \tau_{12} \right) \begin{bmatrix} n_1 & 0 \\ 0 & n_2 \\ n_2 & n_1 \end{bmatrix} \begin{pmatrix} \partial u_1 / \partial x_1 \\ \partial u_2 / \partial x_1 \end{pmatrix} \right\} ds,
\end{aligned}
\tag{4.2}
$$

where U is the strain energy density, σ_{ij} and ε_{ij} are the components of the stress and strain tensors, u_i represents the displacement vector components, ds is the length increment along the C contour and n_i means the unit vector components of the outward normal vector in a given $(X_1 - X_2)$ Cartesian coordinate system [4]. In the case of delaminated beams, using semi-layerwise beam model or even classical Euler-Bernoulli model, the J-integral is calculated by applying a zero-area path integral according to the Figure 4.1b. As the J-integral is path independent this gives absolutely the same results as any other appropriate contour would give [5, 7, 8]. The strain energy density for shear deformable beam, using the Eq.(2.14) constitutive equation, can be expressed as:

$$
U = \frac{1}{2} \int^{\varepsilon_{ij}} \sigma_{ij} d\varepsilon_{ij} = \frac{1}{2} (\sigma_x \varepsilon_x + \tau_{xz} \gamma_{xz}). \tag{4.3}
$$

As it is illustrated by Figure 4.1b, using the semi-layerwise beam model, $X_1 = -X$ and $X_2 = z^{(i)}$. Moreover, because of the zero-area path, the $\boldsymbol{n}$ vector is always parallel to the X axis. Taking into account the actual coordinate system and the assumed displacement field by Eq.(2.1), the G_T energy release rate can be expressed as:

$$
\begin{aligned}
G_T = \sum_{i=1}^{4} \int\limits_{-t_{(i)}/2}^{t_{(i)}/2} \Bigg\{ & \left(-\frac{1}{2} \sigma_{x(i)} \varepsilon_{x(i)} + \tau_{xz(i)} \left(\frac{1}{2} \gamma_{xz(i)} - \frac{\partial w_{(i)}}{\partial x} \right) \right) \Bigg|_{x=-0}^{(undel)} \\
& + \left(\frac{1}{2} \sigma_{x(i)} \varepsilon_{x(i)} - \tau_{xz(i)} \left(\frac{1}{2} \gamma_{xz(i)} - \frac{\partial w_{(i)}}{\partial x} \right) \right) \Bigg|_{x=+0}^{(del)} \Bigg\} dz^{(i)},
\end{aligned}
\tag{4.4}
$$

where the $(undel)$ and (del) superscripts refer to the undelaminated and delaminated portion, respectively [5].

4.2 Mode partitioning of the total J-integral

In order to deal with mixed-mode problems, the J integral can be split into mode-I and mode-II. Although, in this case, the path of the J-integral has to be arranged reflection-symetrically to the delamination front. It was not highlighted previously because the basic defintion of the J-integral to calculate the G_T total energy release rate does not depend on it. Nevertheless, in mode partitioning, it represents a key role [2, 4]. By separating the $\varepsilon_{x(i)}$, $\sigma_{x(i)}$, $\tau_{xz(i)}$ and $\gamma_{xz(i)}$ field quantities into symmetrical and asymmetrical components with respect to the delamination plane, the mode partitioning becomes feasible. Although, apart form that case when the delamination is located exactly in the global reference plane, the position of the delamination is asymmetric. In order to the separtion become possible, first, each and every field quantity has to be shifted into the (X_d - Z_d) coordinate system. It involves only linear function transformations in terms of the ESL thicknesses. After that, the shifted field quantities within the domain $\in [-t_b, t_t]$ have to be extended through the original thickness of the beam. Because this domain does not contain any material, the values above or below the beam can be assumed to be zero functions. Thus the integration has to be carried out with $-t$ lower and t upper limits, where $t := max\{t_{top}, t_{bot}\}$. Thus the components can be expressed as:

$$\begin{aligned}
\varepsilon_{x(sym)} &= \frac{\varepsilon_x(-z_d)+\varepsilon_x(+z_d)}{2}, & \varepsilon_{x(ant)} &= \frac{\varepsilon_x(-z_d)-\varepsilon_x(+z_d)}{2},\\
\gamma_{xz(sym)} &= \frac{\gamma_{xz}(-z_d)+\gamma_{xz}(+z_d)}{2}, & \gamma_{xz(ant)} &= \frac{\gamma_{xz}(-z_d)-\gamma_{xz}(+z_d)}{2},\\
\sigma_{x(sym)} &= \frac{\sigma_x(-z_d)+\sigma_x(+z_d)}{2}, & \sigma_{x(ant)} &= \frac{\sigma_x(-z_d)-\sigma_x(+z_d)}{2},\\
\tau_{xz(sym)} &= \frac{\tau_{xz}(-z_d)+\tau_{xz}(+z_d)}{2}, & \tau_{xz(ant)} &= \frac{\tau_{xz}(-z_d)-\tau_{xz}(+z_d)}{2},
\end{aligned} \tag{4.5}$$

where the (sym) and (ant) subscripts refer to the symmetrical and asymmetrical function components, respectively. In the case of tranverse deflections, since they are independent of the Z or Z_d coordinates (referring to Eq.(3.6) and (3.18)), the decomposition be written as:

$$\left.\frac{\partial w_{(sym)}}{\partial x}\right|_{x=-0}^{(undel)} = \left(\frac{\partial w}{\partial x}\right)\Bigg|_{x=-0}^{(undel)}, \quad \left.\frac{\partial w_{(ant)}}{\partial x}\right|_{x=-0}^{(undel)} = 0. \tag{4.6}$$

and for the delaminated portion:

$$\left.\frac{\partial w_{(sym)}}{\partial x}\right|_{x=+0}^{(del)} = \frac{1}{2}\left(\frac{\partial w_b}{\partial x}+\frac{\partial w_t}{\partial x}\right)\Bigg|_{x=+0}^{(del)}, \quad \left.\frac{\partial w_{(ant)}}{\partial x}\right|_{x=+0}^{(del)} = \frac{1}{2}\left(\frac{\partial w_b}{\partial x}-\frac{\partial w_t}{\partial x}\right)\Bigg|_{x=+0}^{(del)}, \tag{4.7}$$

Using these results the mode separation can be carried out as:

$$\begin{aligned}
G_I = \int_{-t}^{+t} \Bigg\{ & \left(-\frac{1}{2}\sigma_{x(sym)}\varepsilon_{x(sym)} + \tau_{xz(ant)}\left(\frac{1}{2}\gamma_{xz(ant)} - \frac{\partial w_{(ant)}}{\partial x}\right)\right)\Bigg|_{x=-0}^{(undel)}\\
& + \left(\frac{1}{2}\sigma_{x(sym)}\varepsilon_{x(sym)} - \tau_{xz(ant)}\left(\frac{1}{2}\gamma_{xz(ant)} - \frac{\partial w_{(ant)}}{\partial x}\right)\right)\Bigg|_{x=+0}^{(del)}\Bigg\} dz_d,
\end{aligned} \tag{4.8}$$

and

$$\begin{aligned}
G_{II} = \int_{-t}^{+t} \Bigg\{ & \left(-\frac{1}{2}\sigma_{x(ant)}\varepsilon_{x(ant)} + \tau_{xz(sym)}\left(\frac{1}{2}\gamma_{xz(sym)} - \frac{\partial w_{(sym)}}{\partial x}\right)\right)\Bigg|_{x=-0}^{(undel)}\\
& + \left(\frac{1}{2}\sigma_{x(ant)}\varepsilon_{x(ant)} - \tau_{xz(sym)}\left(\frac{1}{2}\gamma_{xz(sym)} - \frac{\partial w_{(sym)}}{\partial x}\right)\right)\Bigg|_{x=+0}^{(del)}\Bigg\} dz_d.
\end{aligned} \tag{4.9}$$

Using zero function extension of the field quantities above or below the delaminated beam, according to the actual location of the delamination front through the thickness, the original value of the J-integral does not change. It is also crucial from the point of mode mixity. Thus, the following relationship can always be ensured:

$$G_T = G_I + G_{II}. \tag{4.10}$$

Chapter 5

Built-in configuration

In this chapter the previously introduced method of 4ESLs is used to describe the diplacement and stress fields around the crack tip in a delaminated orthotropic composite beam with built-in end. Furthermore, in terms of different load cases, geometries and material structures, the mode mixity is investigated by applying J-integral and its decomposition. The computation is performed in the code MAPLE. The results are compared to finite element analisys (FEA), where the virtual crack closure technique (VCCT) is applied to determine mode mixity and with other models from the literature. These models are mostly based on Euler-Bernoulli classical beam theory. Solutions of these models with details can be found in Appendix B.

5.1 Analytical solution

The geometry of problem with the associated structure of ESLs is depicted in Figure 5.1, where l is total length, b denotes the width and $2h$ represents the total thickness of the beam. As the delamination splits the structure into a top and bottom sub-laminates, the corresponding thicknesses of these parts are denoted by t_t and t_b. These portions are modelled further with 2-2 ESLs, respectively, resulting 4ESLs in the undelaminated portion. The thicknesses of the ELSs are determined as half of the actual sub-laminate thickness. Two type of problems are investigated. First, when the beam is made out only unidirectional carbon reinforced epoxy material and secondly, when it contains unidirectional and woven

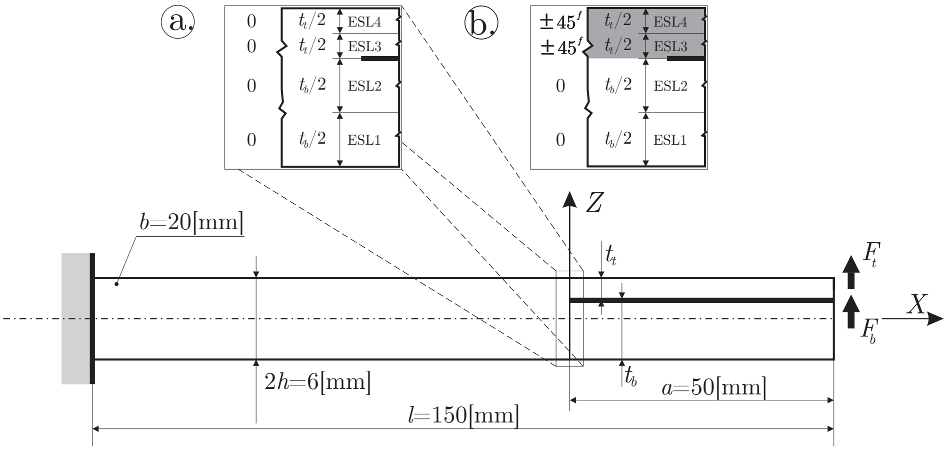

FIGURE 5.1: Built-in configuration of delaminated beam with only one material (a) and with two different material structure (b).

fabric plies also. The material properties (moduli and Poisson's ratios) of the individual laminae are given by Table 5.1.

	E_{11} [GPa]	E_{22} [GPa]	E_{33} [GPa]	G_{23} [GPa]	G_{13} [GPa]	G_{12} [GPa]	ν_{23} [-]	ν_{13} [-]	ν_{12} [-]
0	148	9.65	9.65	3.86	3.71	3.71	0.27	0.25	0.25
$\pm 45^f$	16.39	16.39	16.4	5.46	5.46	16.4	0.5	0.5	0.3

TABLE 5.1: Elastic properties of single carbon/epoxy composite laminates

5.1.1 Continuity conditions

In the sequal the continuity of displacements and stress resultants between the delaminated and undelaminated regions is detailed. The conditions are imposed against the primary parameters of both regions. The continuity of the membrane displacement components between the top parts of the delaminated and undelaminated regions can be ensured by imposing the equality between the membrane displacements terms on a single ESL in the delaminated part and a single one in the undelaminated one. This statement is also true for the bottom parts, as well. These conditions are satisfied through the following equations:

$$\left(u_0 + \sum_{j=1}^{q_{undel}} K_{1j}^{(0)} \psi_j \Big|_{x=-0}^{(undel)}\right) = \left(u_{0b} + \sum_{j=1}^{q_{del}} K_{1j}^{(0)} \psi_j\right)\Big|_{x=+0}^{(del)}, \tag{5.1}$$

$$\left(u_0 + \sum_{j=1}^{q_{undel}} K_{3j}^{(0)} \psi_j \Big|_{x=-0}^{(undel)}\right) = \left(u_{0t} + \sum_{j=1}^{q_{del}} K_{3j}^{(0)} \psi_j\right)\Big|_{x=+0}^{(del)}, \tag{5.2}$$

meaning two conditions for each theory. Because the transverse deflection of the undelaminated part, the bottom and top delaminated parts is modelled only one-one term in each theory, the continuity of the deflections involves similarly two conditions:

$$w\Big|_{x=-0}^{(undel)} = w_b\Big|_{x=+0}^{(del)}, \tag{5.3}$$

and

$$w\Big|_{x=-0}^{(undel)} = w_t\Big|_{x=+0}^{(del)}. \tag{5.4}$$

The total continuity of the first-, second-, and third-order terms in the displacement functions can be imposed through the vector of primary paremeters by connecting the first-order terms with first-order terms, the second- and the third-order terms with the corresponding second- and third-order terms. For the TSDT theory, by referring to Eq.(3.7) and (3.19), it can be expressed in the following way:

$$\begin{pmatrix}\theta_3 & \psi_1 & \psi_2 & \psi_2 & \psi_4\end{pmatrix}\Big|_{x=-0}^{(undel)} = \begin{pmatrix}\theta_3 & \psi_1 & \psi_2 & \psi_2 & \psi_4\end{pmatrix}\Big|_{x=+0}^{(del)}, \tag{5.5}$$

meaning q_{undel} number of conditions between the portions. Unfortunately, the number of parameters in the $\boldsymbol{\psi_p}$ vector for the undelaminated and delaminated parts are not equal to each other $q_{del} \neq q_{undel}$. The continuity of these terms cannot be expressed in a simple way beacuse $q_{del} > q_{undel}$. To handle this issue the theorem of auto-continuity has to be applied [8]. The remaining θ_1 term in the primary parameter vector of the delaminated part can be called as auto-continuity parameter, because continuity of this term can be ensured automatically by using only the primary parameters of the undelaminated parts:

$$\begin{aligned}\theta_1\Big|_{x=+0}^{(del)} &= \sum_{j=1}^{q_{undel}} K_{1j}^{(1)}\psi_j\Big|_{x=-0}^{(undel)} \\ &= \left(\theta_3 - \frac{t_1(t_1+2t_2)\phi_1 + (t_1+2t_2)^2\phi_2}{2(t_1+t_2)} - \frac{(3t_3+2t_4)t_3\phi_3 - t_3^2\phi_4}{2(t_3+t_4)}\right)\Big|_{x=-0}^{(undel)}.\end{aligned} \tag{5.6}$$

Thus the final number of conditions becomes $q_{undel} + 1 = 5 + 1 = 6$ for TSDT theory. The situation for SSDT theory, by referring to Eq.(3.11) and (3.23), is absolutely the same. The $q_{del} \neq q_{undel}$ inequality can be handled through the following way:

$$\begin{pmatrix}\theta_1 & \theta_3 & \psi_1 & \psi_2 & \psi_4\end{pmatrix}\Big|_{x=-0}^{(undel)} = \begin{pmatrix}\theta_1 & \theta_3 & \psi_1 & \psi_2 & \psi_4\end{pmatrix}\Big|_{x=+0}^{(del)}, \tag{5.7}$$

meaning q_{undel} number of conditions again. The auto-continuity of the remaining ψ_3 in the primary parameter vector of the delaminated part can be ensured by:

$$\begin{aligned}\phi_3\Big|_{x=+0}^{(del)} &= \sum_{j=1}^{q_{undel}} K_{3j}^{(2)}\psi_j\Big|_{x=-0}^{(undel)} \\ &= \left(\frac{-\theta_1 + \theta_3 - t_1\phi_1 - 2t_2\phi_2}{t_3}\right)\Big|_{x=-0}^{(undel)}.\end{aligned} \tag{5.8}$$

Thus the final number of conditions becomes $q_{undel} + 1 = 5 + 1 = 6$ for SSDT theory, as well. Fortunately, in the case of FSDT theory, by referring to Eq.(3.12) and (3.24), the number of parameters in primary parameter vector for undelaminated and delaminated portions are equal to each other $q_{del} = q_{undel}$. Thus, futher auto-continuity condition is not required to impose the displacement continuity. It can be expressed easily by imposing:

$$\begin{pmatrix}\theta_1 & \theta_2 & \theta_3 & \theta_4\end{pmatrix}\Big|_{x=-0}^{(undel)} = \begin{pmatrix}\theta_1 & \theta_2 & \theta_3 & \theta_4\end{pmatrix}\Big|_{x=+0}^{(del)}, \tag{5.9}$$

meaning $q_{del} = q_{undel} = 4$ conditions.

The continuity conditions of stress resultants between the delaminated and undelaminated regions can be imposed by using the equivalent stress resultants [5]. These equations can be directly read out from the equilibrium equations, referring to Eqs.(3.8)-(3.10) and Eqs.(3.20)-(3.22), by omitting derivatives with respect to the x coordinate. In the case of those equlilibrium equations, which correspond to the $\boldsymbol{\psi_{(p)}}$ primary parameter vector the $Q_{x(i)}$ shear and the $R_{x(i)}$, $S_{x(i)}$ higher-order shear forces must be omitted aslo to obtain the equivalent bending moments [1, 5]. According to the Figure 5.2, as a result of arbitrary external forces, $Q_{x(i)}$, $R_{x(i)}$, $S_{x(i)}$ $N_{x(i)}$, $M_{x(i)}$, $L_{x(i)}$ and $P_{x(i)}$ unknown stress resultants taking place at the end of the delaminated portion in each ESL. These are transferred between the

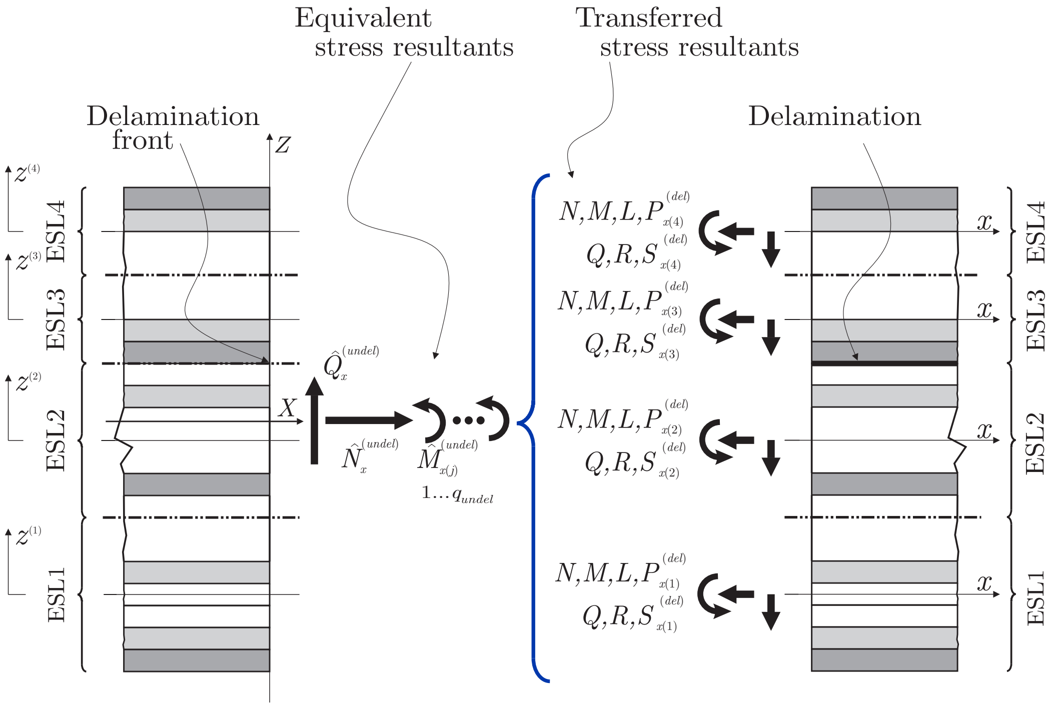
Equivalent stress resultants
Transferred stress resultants
Delamination front
Delamination
Z
$z^{(4)}$
$z^{(3)}$
$z^{(2)}$
$z^{(1)}$
ESL4
ESL3
ESL2
ESL1
X
$\hat{Q}_x^{(undel)}$
$\hat{N}_x^{(undel)}$
$\hat{M}_{x(j)}^{(undel)}$
$1 \dots q_{undel}$
$N,M,L,P_{x(4)}^{(del)}$
$Q,R,S_{x(4)}^{(del)}$
$N,M,L,P_{x(3)}^{(del)}$
$Q,R,S_{x(3)}^{(del)}$
$N,M,L,P_{x(2)}^{(del)}$
$Q,R,S_{x(2)}^{(del)}$
$N,M,L,P_{x(1)}^{(del)}$
$Q,R,S_{x(1)}^{(del)}$
x
Undelaminated portion
Delaminated portion

FIGURE 5.2: Continuity of the stress resultants at the delamination front.

portions in such a way to cause equivalent normal force, equivalent shear force and equivalent bending moments in the undelaminated portion at the delamination front. For the sake of simplicity and because there is not any conventional system in the actual literature to indicate higher-order stress resultants, the same arrows are used to sign them [1] in the above mentioned figure.Therefore, the following equation can be formulated to express the continuity of the normal forces at the cross section of delamination tip:

$$\hat{N}_x^{(undel)} = \sum_{i=1}^{4}\left(N_{x(i)}\right)\Bigg|_{x=-0}^{(undel)} = \sum_{i=1}^{2}\left(N_{x(i)}\right)\Bigg|_{x=+0}^{(del)} + \sum_{i=3}^{4}\left(N_{x(i)}\right)\Bigg|_{x=+0}^{(del)}, \tag{5.10}$$

where $\hat{N}_x^{(undel)}$ denotes the equivalent normal force meaning one condition for each theory. The shear force continuity can be described similarly as:

$$\hat{Q}_x^{(undel)} = \sum_{i=1}^{4}\left(Q_{x(i)}\right)\Bigg|_{x=-0}^{(undel)} = \sum_{i=1}^{2}\left(Q_{x(i)}\right)\Bigg|_{x=+0}^{(del)} + \sum_{i=3}^{4}\left(Q_{x(i)}\right)\Bigg|_{x=+0}^{(del)}, \tag{5.11}$$

where $\hat{Q}_x^{(undel)}$ is the equivalent shear force representing a further condition for each case.

The final conditions between the portions are the continuity of the equivalent bending moments. These continuity conditions can be formulated as:

$$\begin{aligned}\hat{M}_{x(j)}^{(undel)} &= \sum_{i=1}^{4}\left(K_{ij}^{(0)}\; K_{ij}^{(1)}\; K_{ij}^{(2)}\; K_{ij}^{(3)}\right)\Big|^{(undel)} \cdot \left.\begin{pmatrix} N_{x(i)} \\ M_{x(i)} \\ L_{x(i)} \\ P_{x(i)} \end{pmatrix}\right|_{x=-0}^{(undel)} = \\ &= \sum_{i=1}^{4}\left(K_{ij}^{(0)}\; K_{ij}^{(1)}\; K_{ij}^{(2)}\; K_{ij}^{(3)}\right)\Big|^{(undel)} \cdot \left.\begin{pmatrix} N_{x(i)} \\ M_{x(i)} \\ L_{x(i)} \\ P_{x(i)} \end{pmatrix}\right|_{x=+0}^{(del)}, \qquad j = 1..q_{undel},\end{aligned} \tag{5.12}$$

where $\hat{M}_{x(j)}^{(undel)}$ denotes the equivalent bending moments imposing four conditions for the FSDT theory and five conditions for the SSDT and TSDT theories.

5.1.2 Boundary conditions

In the case of built-in end, the displacement field must be zero. Meaning there is no deflection, membrane displacement or even rotation. This condition can be easily imposed be using the primary parameters:

$$u_0\big|_{x=-l+a}^{(undel)} = 0, \qquad w\Big|_{x=-l+a}^{(undel)} = 0, \qquad \boldsymbol{\psi_p}\Big|_{x=-l+a}^{(undel)} = \mathbf{0}. \tag{5.13}$$

The external forces and bending moments can be taken into account in such a way as the stress resultants are treated in the case of continuity. These similarly cause equivalent shear forces, normal forces and bending moments in the delaminated region, separately for the top and bottom parts. Because there are not any normal forces at the end of the beam, the following two boundary conitions can be imposed for each theory:

$$\sum_{i=1}^{2}\left.\left(N_{x(i)}\right)\right|_{x=a}^{(del)} = 0, \qquad \sum_{i=3}^{4}\left.\left(N_{x(i)}\right)\right|_{x=a}^{(del)} = 0. \tag{5.14}$$

As it is shown by Figure 5.1, the top and bottom parts of the delaminated regions are loaded with F_t and F_b forces, causing two conditions for each theory:

$$\sum_{i=1}^{2}\left.\left(Q_{x(i)}\right)\right|_{x=a}^{(del)} = F_t, \qquad \sum_{i=3}^{4}\left.\left(Q_{x(i)}\right)\right|_{x=a}^{(del)} = F_b. \tag{5.15}$$

And finally, because the lack of any external bending moments:

$$\sum_{i=1}^{4}\left(K_{ij}^{(0)}\; K_{ij}^{(1)}\; K_{ij}^{(2)}\; K_{ij}^{(3)}\right)\Big|^{(del)} \cdot \left.\begin{pmatrix} N_{x(i)} \\ M_{x(i)} \\ L_{x(i)} \\ P_{x(i)} \end{pmatrix}\right|_{x=-a}^{(del)} = \begin{pmatrix} 0 \\ 0 \\ 0 \\ 0 \end{pmatrix} \qquad j = 1..q_{del}, \tag{5.16}$$

	FSDT	SSDT	TSDT
No. of Unknown functions	6+8	7+10	7+10
No. of Differential equations	6+8	7+10	7+10
No. of Boundary conditions	㉘	㉞	㉞
Membrane disp. cont. $(x=0)$	1+1	1+1	1+1
Deflection cont. $(x=0)$	1+1	1+1	1+1
Vector of primary par. cont. $(x=0)$	4	5	5
Auto cont. $(x=0)$	0	(+1)	(+1)
Normal force cont. $(x=0)$	1	1	1
Shear force cont. $(x=0)$	1	1	1
Equivalent bending cont. $(x=0)$	4	5	5
Built-in end $(x=-l+a)$	2+4	2+5	2+5
Acting normal forces $(x=a)$	1+1	1+1	1+1
Acting shear forces $(x=a)$	1+1	1+1	1+1
Acting equivalent bendings $(x=a)$	2+2	3+3	3+3
Σ	㉘	㉞	㉞

TABLE 5.2: Summary of the necasarry continuity and boundary conditions for each theory.

representing five boundary conditions for FSDT and six-six conditions for SSDT and TSDT. The applied theories with the number of unknown functions and differential equations are summarized by Table 5.2. This table contains the number of conditions coming from the continuity and the boundray conditions, also.

5.2 FEA solution

In order to verify the analytical results finite element (FE) analyses were carried out. The structure of the mesh with the necessary boundary conditions and the applied Davidson mesh to determine energy release rates are depicted in Figure 5.3. The FEA model is applicable to use it for bi-material case, as well. The scheme and relevant equations of VCCT technique can be found in Appendix B.3. The material properties are given by Table 5.1.

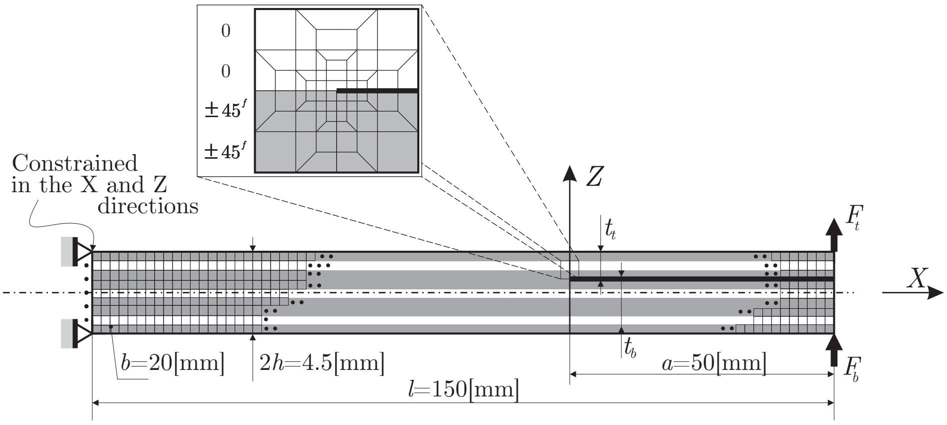

FIGURE 5.3: Discretization of the delaminated beam with only one material (a) and using two different materials (b) with the applied Davidson mesh at the crack tip.

5.3 Results - Displacement and stress

In this section the analytical and numerical results are compared to each other in the case of built-in configuration. The analyses are carried out by using the present TSDT, SSDT and FSDT solutions. Different load cases are investigated for single-material and bi-material cases containing symmetric and antisymmetric delamination position. The corresponding dipslacement fields and stress fields are investigated and compared to each other. The actual geometry and the structure of the layers are always indicated in the subsequent figures.

5.3.1 Transversely isotropic beam

In the case of symmetric delamination position, using only UD carbon/ epoxy layers, when the delaminated parts are teared with $F_t = 200$ N and $F_b = -200$ N forces, the displacement field is depicted in Figure 5.4. The in-plane u displacement, using any kind of higher-order theories, agrees very well with the numerical solutions. In terms of the w deflections the agreement between numerical and analytical results is very good. As it was expected, the delamination opening takes place. Although, the usage of higher-order theories results smaller values comparing to the numerical set of points, which are determined along the middle lines of the top and bottom parts of the beam. As it is illustrated also in the higlighted part of the figure, the additional contribution of the higher-order theories to the deflection becomes smaller and smaller. Thus, the improvement of deflection by the SSDT and TSDT compared to the FSDT is negligible. Using only FSDT the deflection can be obtained with sufficient accuracy. In order to understand the importance of the higher order theories Figure 5.5 depicts further results in terms of the normal and shear stresses.

The stresses are evaluated in the cross section of the delamination tip, respectively, at the undelaminated $X = -0$ and delaminated $X = -0$ regions. As a reminder, referring to the Table 5.2, only the continuity conditions of the displacement field can be imposed between the portions resulting certain stress discontinuities at the crack tip. This property of the stress field is highlihted in Figure 5.5. As it is shown, in the case of σ_x normal stresses, a quite good agreement with the FEA result can be seen. On the contrary of the analytical solutions, the numerical solution has singular nature in terms of the stress field. By decreasing the mesh size at the crack tip the stresses become inevitably higher and higher. Apart from this phenoma, by using reasonable mesh size, the trends of the normal stress solutions are exactly the same, meaning each theory is applicable.

In the case of τ_{xz} shear stresses the situation is different. This is the point where the usage of higher-order beam theories makes sense and becomes quite important. According to Figure 5.5b, by increasing the order of solutions, the shear stress can be described with more and more preciseness. If the accurate desription of the shear stress is important at the crack tip then the application of higher order theories becomes inevitable.

In order to help the understanding of the mode mixity, the previously introduced mode partitioning method is discussed here also. According to Eq.(4.5), the mode separation becomes possible by decomposing the strain and stress quantities into symmetrical and asymmetrical components with respect to the delamination position. Fortunately, in this previous demonstrated example, the delamination is located exactly in the global reference plane making the decomposition quite easy and straightforward. Even by visual observation the following can be stated: the distribution of the σ_x normal stress is absolutely symmetric and the distribution of the τ_{xz} shear stress is perfectly asymmetric to the location of the delamination. These properties are valid for the ε_x and γ_{xz} strains, as well. Using the Eqs.(4.8) and

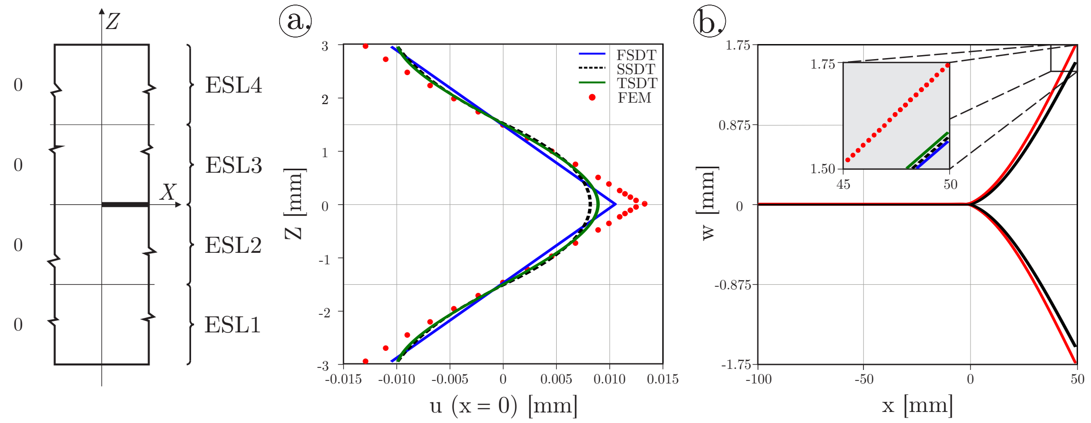

FIGURE 5.4: Distribution of the u displacement at the delamination front (a) and comparison of the deflections along the beam (b), $F_t = 200$ N and $F_b = -200$ N.

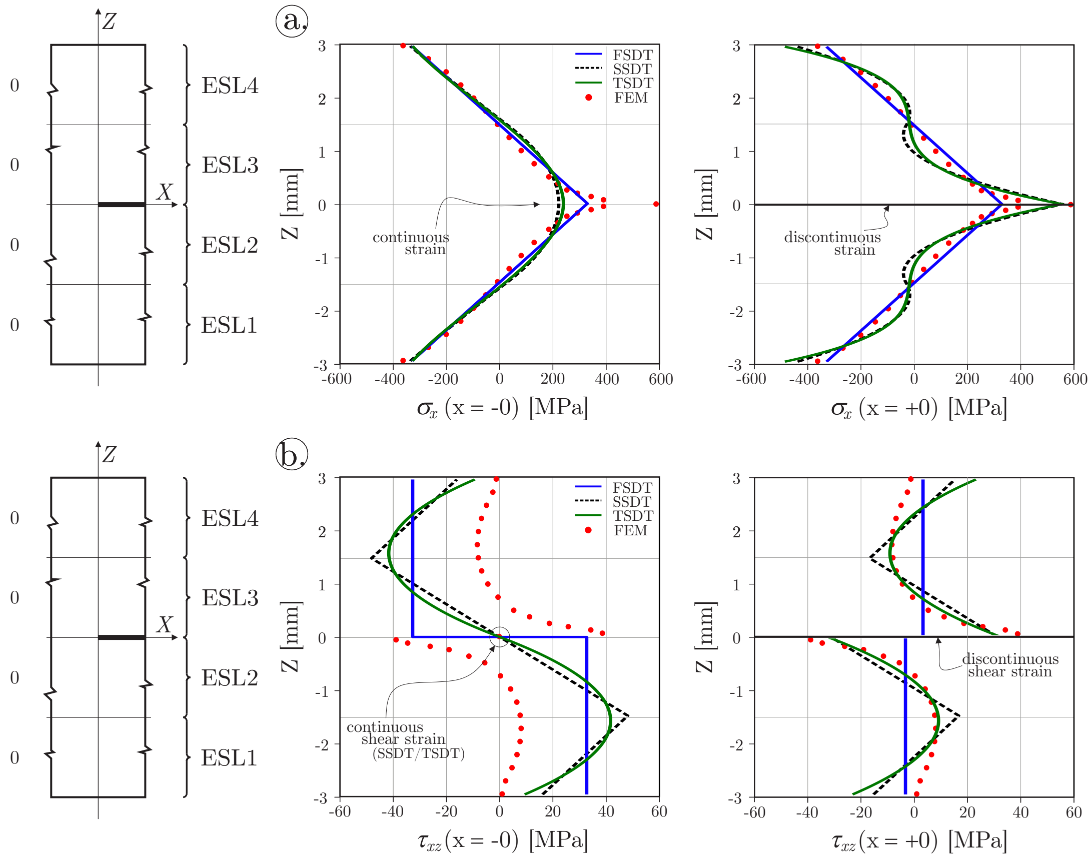

FIGURE 5.5: Distribution of the σ_x normal stresses (a) and the τ_{xz} shear stresses at the delamination tip (b), $F_t = 200$ N and $F_b = -200$ N.

(4.9), it can be easily seen that this loading case with symmetric location of the delaination causes pure mode-I energy relase rate.

Loading symmetrically delaminated UD carbon/epoxy beam with $F_t = 200$ N and $F_b = 200$ N forces the so-called "End-load split" specimen (ELS) can be obtained. The displacement and stress fields are illustrated in Figure 5.6 and 5.7. As these figures represent, there is quite good agreement between the analytical and numerical solutions in terms of

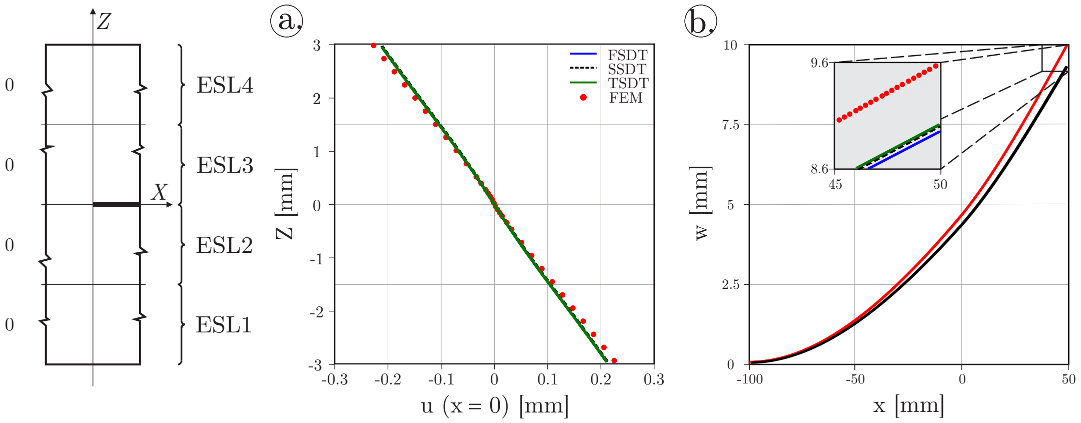

FIGURE 5.6: Distribution of the u displacement at the delamination front (a) and comparison of the deflections along the beam (b), $F_t = 200$ N and $F_b = 200$ N.

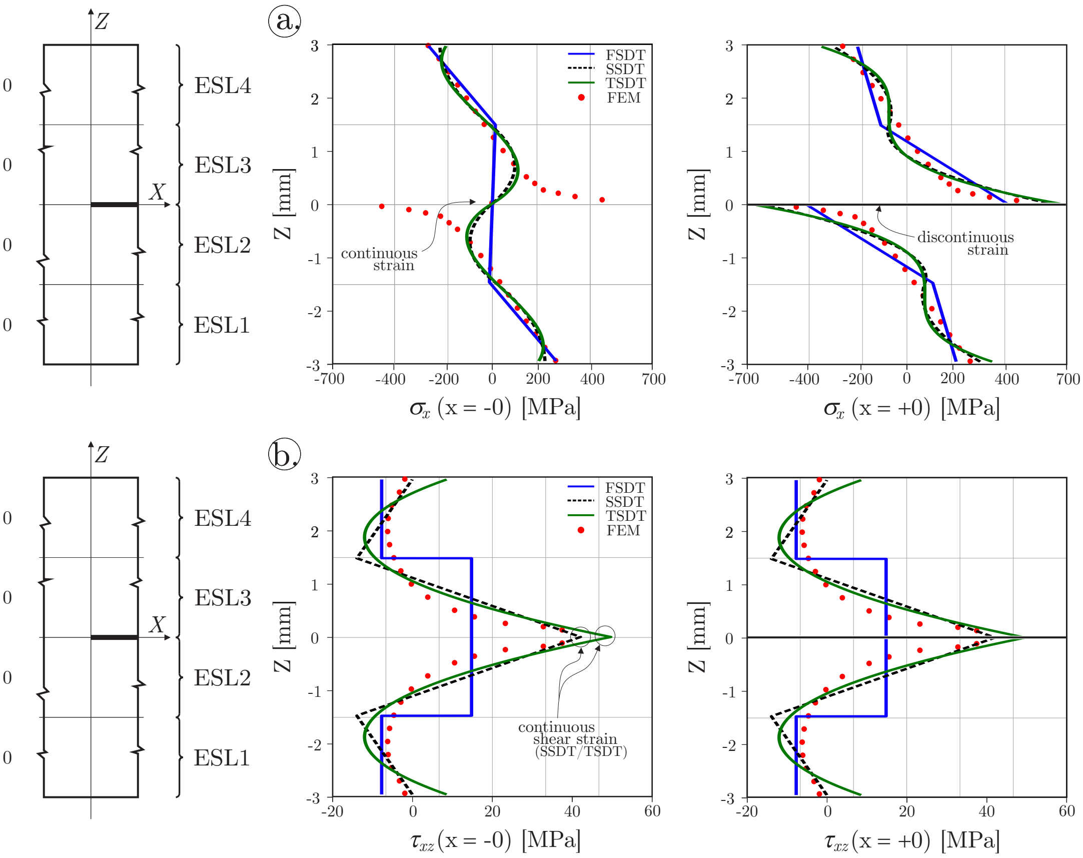

FIGURE 5.7: Distribution of the σ_x normal stresses (a) and the τ_{xz} shear stresses at the delamination tip (b), $F_t = 200$ N and $F_b = 200$ N.

displacement. Application of SSDT and TSDT theories are not necessarily required, if the displacement terms are considered only. Although, similarly to the previous example, if stresses represent important role of the investigation the application of the higher-order theories is inevitable and essential. Using visual observation and Eq.(4.9), the following can be seen: the distribution of the σ_x is perfectly asymmetric and the distribution of the τ_{xz} is totally symmetric to the delamination plane resulting in pure mode-II energy release rate.

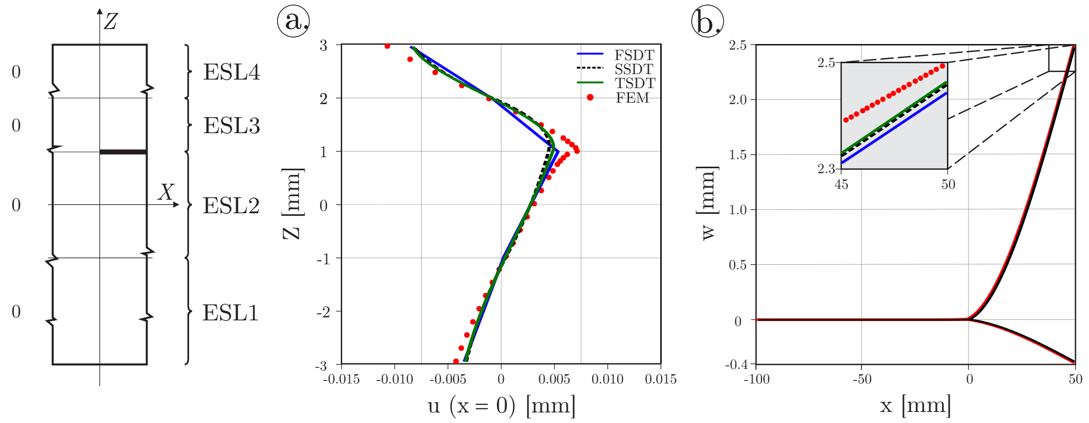

FIGURE 5.8: Distribution of the u displacement at the delamination front (a) and comparison of the deflections along the beam (b), $F_t = 100$ N and $F_b = -100$ N.

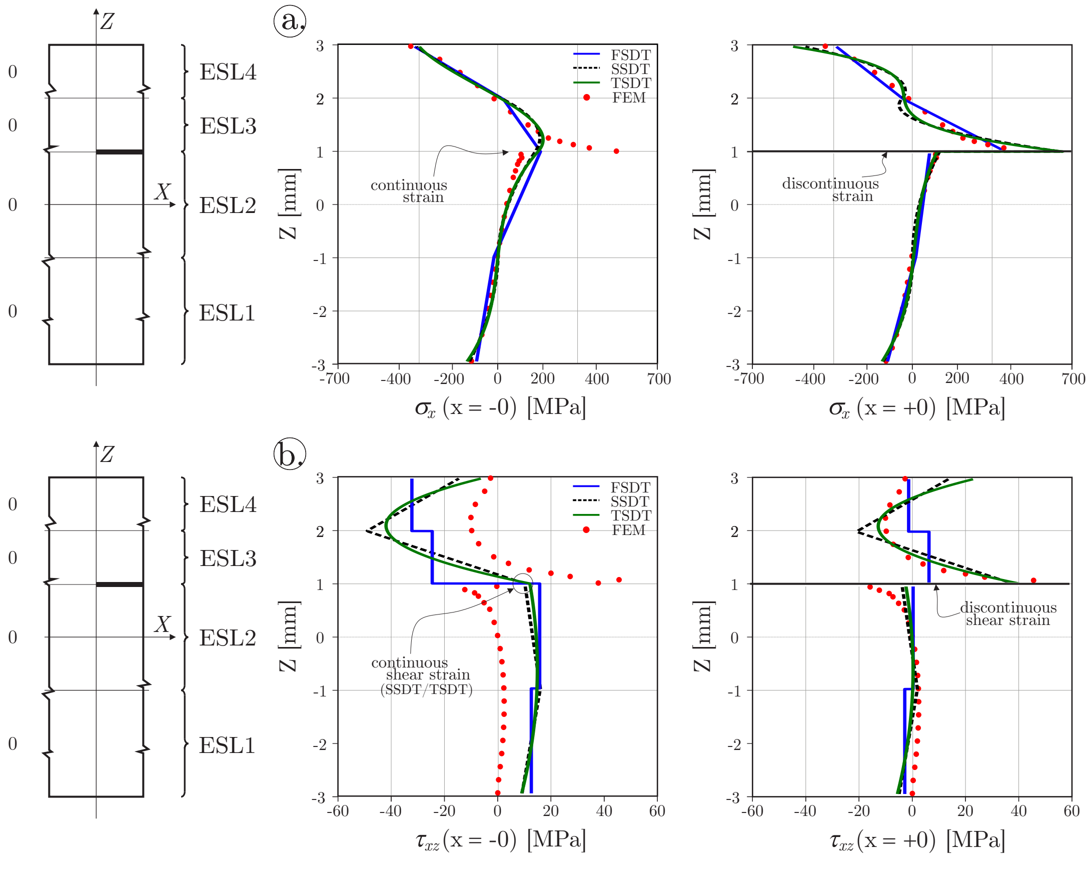

FIGURE 5.9: Distribution of the σ_x normal stresses (a) and the τ_{xz} shear stresses at the delamination tip (b), $F_t = 100$ N and $F_b = -100$ N.

An asymmetrically delaminated UD carbon /epoxy built-in beam with $F_t = 100$ N and $F_b = -100$ N acting forces are investigated in Figure 5.8 and 5.9. As it shown by the figures, the geometry of the beam is not changed, although, the location of the delamination is no longer coincident with the global reference plane. The distribution of the u displacement, σ_x normal stress and τ_{xz} shear stress through the thickness of the beam at the delamination tip section can be determined and compared to the FEA solution. As it is shown by the figure,

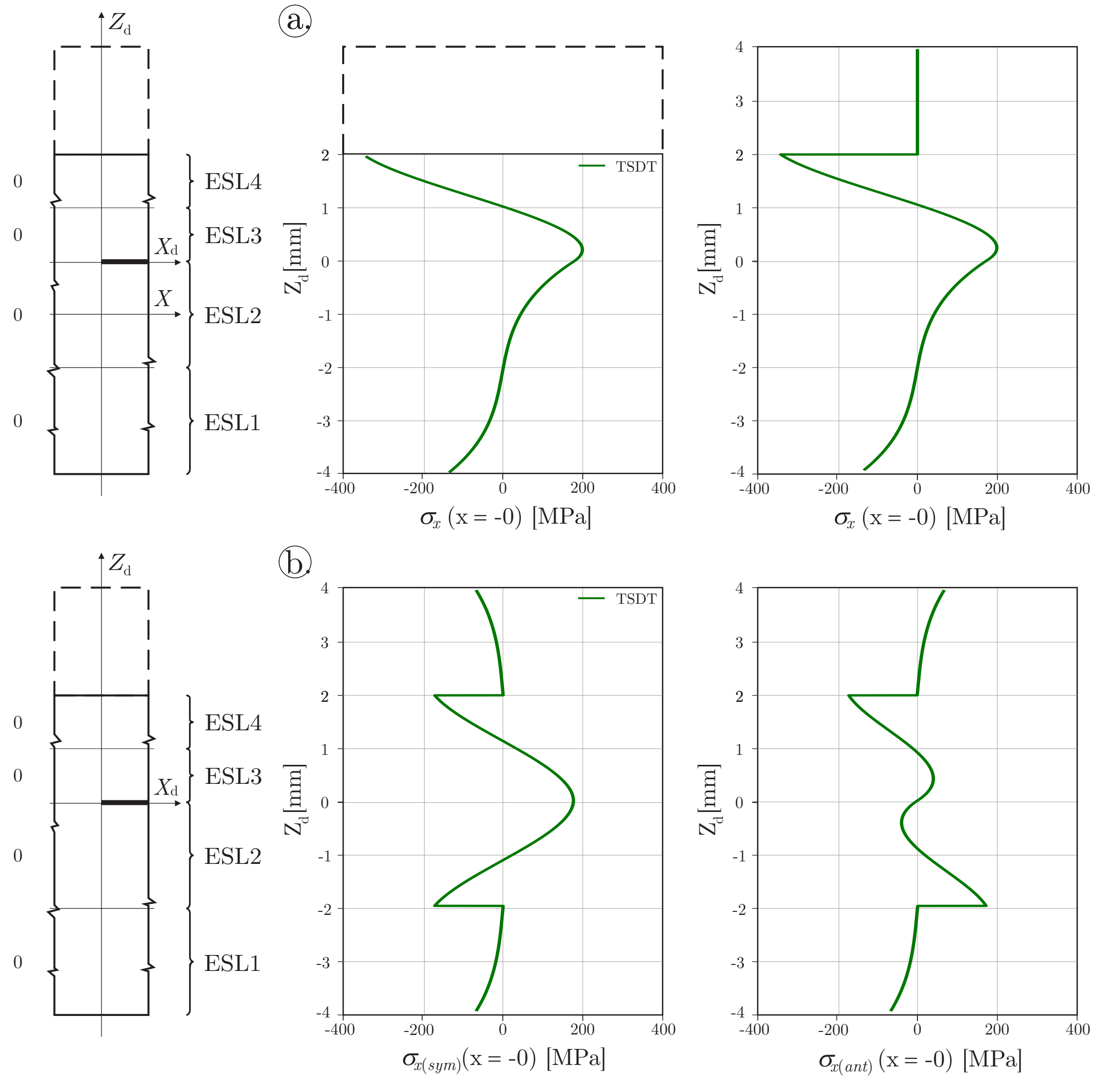

FIGURE 5.10: Tranformation of the σ_x field function into the delamination coordinate system(a) and extension of the field with zero value function above the beam (b).

these terms cannot be decomposed easily into the symmetric and asymmetric components with respect to the delamination plane. Furthermore, as it was introduced previously, function transformation and extension are necassary to make the decomposition possible. In order to make it comprehensible Figure 5.10 illustrates an example with σ_x normal stress function. First the field quantitiy has to be shifted into the delamination coordinate system and has to be extended with zero value function above the beam to make the domain symmetric. Thus the decomposition can be performed according to Eq.(4.5). The results are illustrated by Figure 5.10b. Using similar transformation for the other field quantities and applying Eq.(4.8) and (4.9) the determination of the mode mixity becomes achievable.

5.3.2 Bi-material beam

Figure 5.11 and 5.12 depict further results in terms of bi-material beam. The bi-material beam contains UD carbon and woven fabric plies as well. The materials are separated from each other at the delaminated region and loaded with $F_t = 200$ N, $F_b = -200$ N forces.

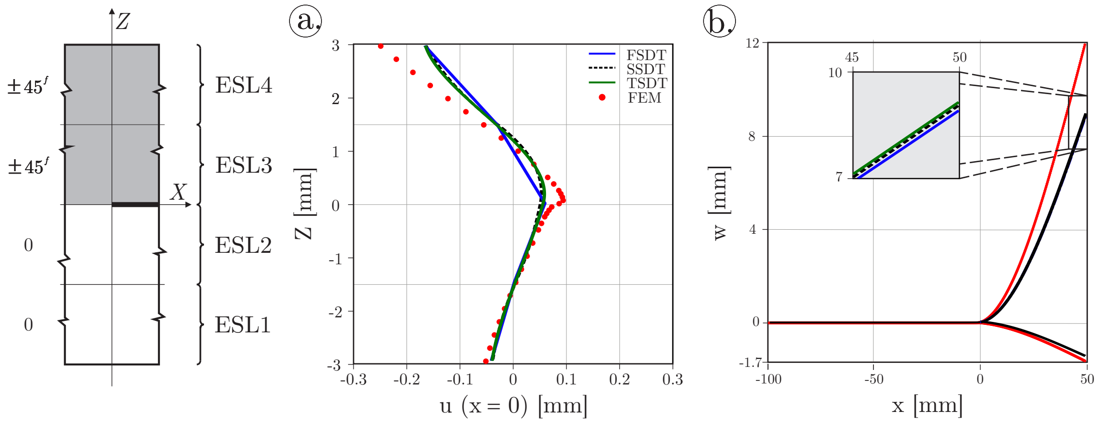

FIGURE 5.11: Distribution of the u_x displacement at the delamination front (a) and comparison of the deflections along the bi-material beam (b), $F_t = 200$ N and $F_b = -200$ N.

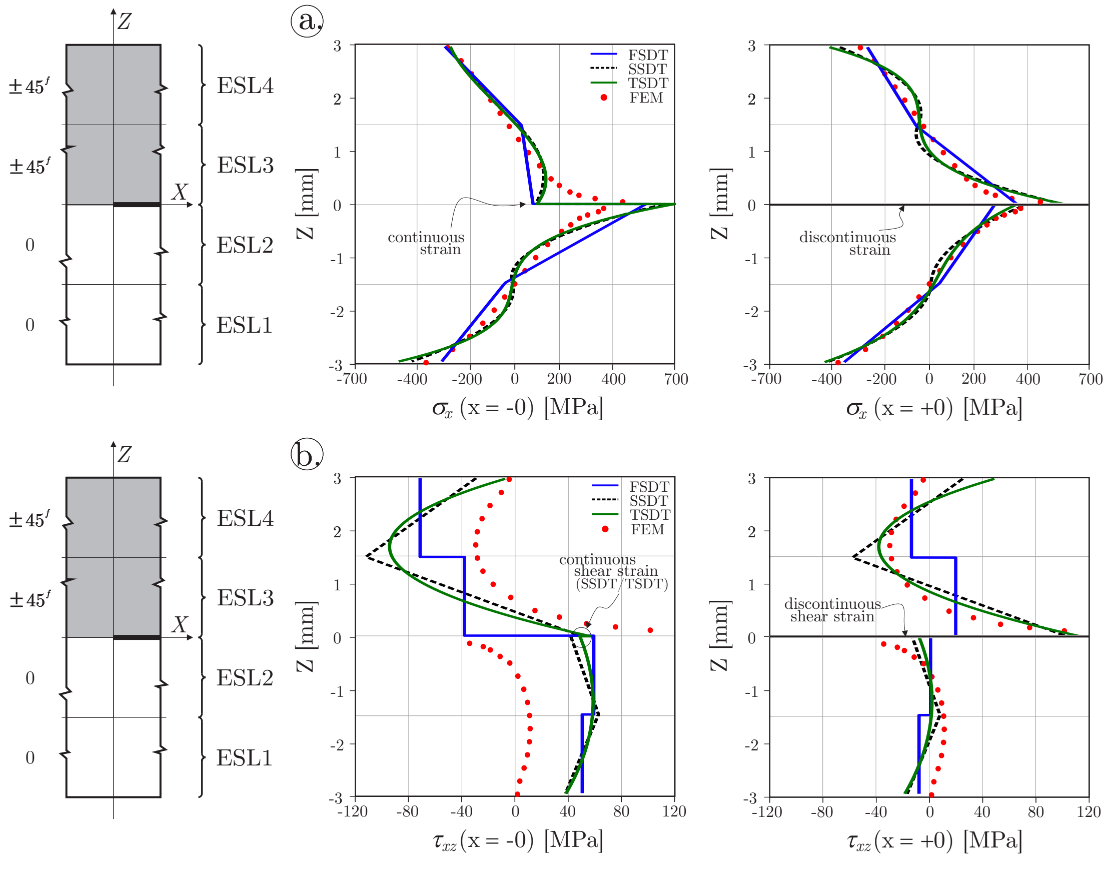

FIGURE 5.12: Distribution of the σ_x normal stresses (a) and the τ_{xz} shear stresses (b) at the delamination front in the case of bi-material beam, $F_t = 200$ N and $F_b = -200$ N

The location of the delamination is symmetric. The UD plies are located at the bottom sub-laminate and the carbon woven fabrics at the top sub-laminate with quite different material properties (referring to Table 5.1). According to Figure 5.11b, the difference between the stiffnesses can be realized immediately. Applying same range of force for the top and bottom part causes significantly higher deflection in the case of top part, which is made out

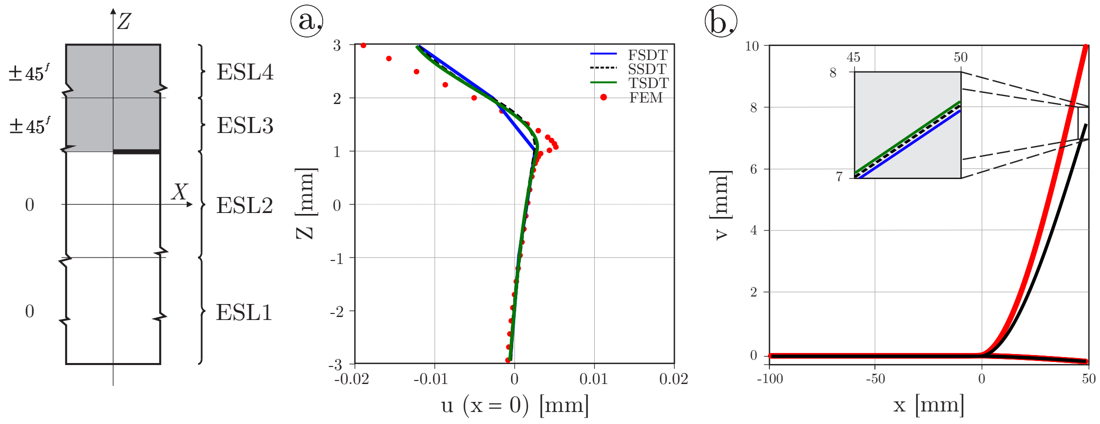

FIGURE 5.13: Distribution of the u_x displacement at the delamination front (a) and comparison of the deflections along the bi-material beam (b), $F_t = 50$ N and $F_b = -50$ N.

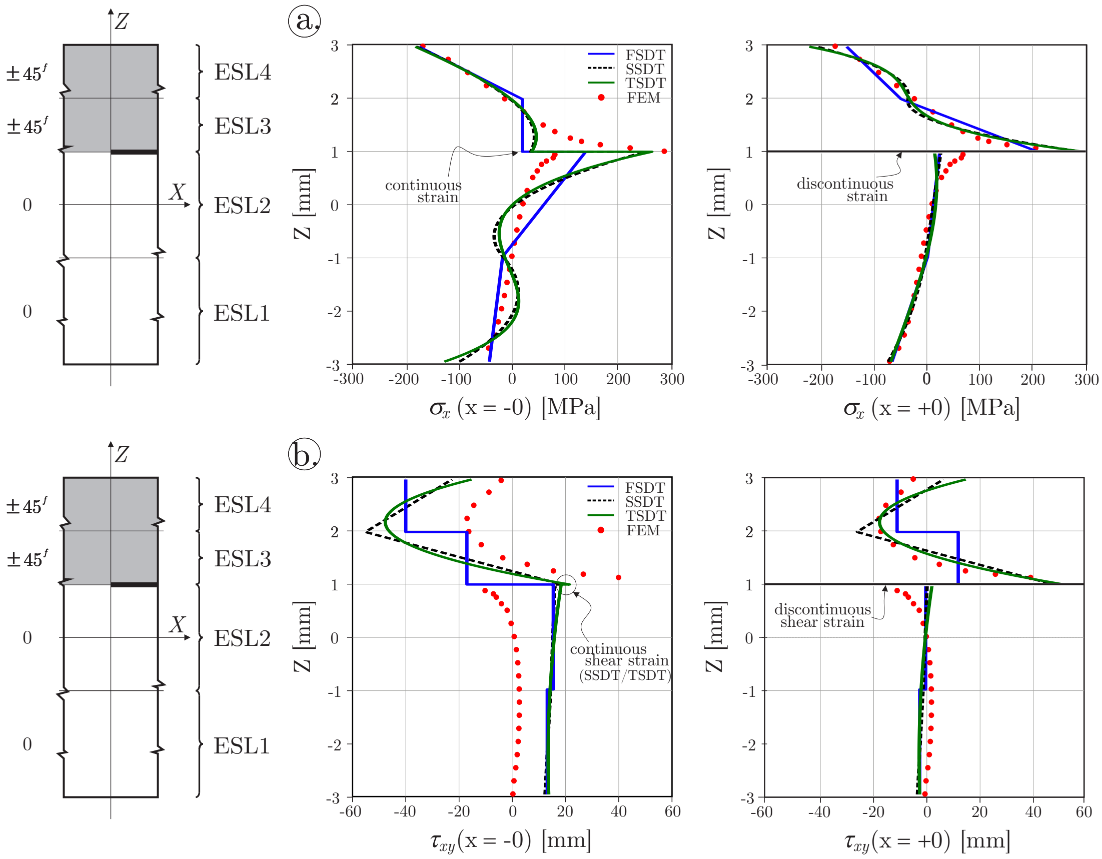

FIGURE 5.14: Distribution of the σ_x normal stresses (a) and the τ_{xz} shear stresses (b) at the delamination front in the case of bi-material beam, $F_t = 50$ N and $F_b = -50$ N.

of carbon woven fabrics. Similary to the previously introduced tranversely isotropic examples, the application of any kinds of higher-order theory results good agreement with the numerical set of data in terms of the u displacement. As it is higlighted by the Figure 5.11b, the utilization of SSDT or TSDT theory causes very small additional contribution to the w deflection compared to the FSDT solution. Using only FSDT the deflection can be calculated with good accuracy. In order to understand the importance of the higher-order theories the stress field has to be investigated.

Figure 5.12 illustrates the distribution of σ_x normal and τ_{xz} shear stresses at the delamination front. Similar discontinuities can be seen between the undelaminated and delaminated portions at the crack tip. Moreover, using two kinds of material, certain jumps in the stress field can be noticed between the ESLs. This phenomena is caused by the different material properties. It is important to higlight and emphasize, the strain continuities between the ESLs, which are imposed by the system of exact kinematic conditions in Eqs.(2.2)-(2.6), are still hold. Only the above mentioned differences between the material properties of UD carbon and woven fabrics cause certain jumps in the stress field. Obviously , it does not disturb the continuity of the strain field. It can be experienced in the case of normal and shear stresses, as well.

In order to analyze the stress field further, it makes sense to compare Figure 5.7 with Figure 5.12, where only the material properties of the top part are different. The geometry, the location of the delamination, and the loadings are absolutely the same. As it is shown, it cause significant change in terms of the stress fields. Thus, contrary to the previous case, the functions are not pure symmetric or asymmetric functions, meaning this loading scenario causes mode-I and mode-II energy relase rates, as well. It indicates that modification of the material properties within one sub-laminate can change the mode mixity, even if the location of the delamination and the loadings are the same.

Finally, for the sake of completeness, Figure 5.13 and 5.14 illustrate an example when the bi-material beam is asymmetrically delaminated with $F_t = 50$ N and $F_b = -50$ N forces acting. The distribution of the u displacement, σ_x normal stress and τ_{xz} shear stress at the delimantion tip can be determined and compared to the numerical set of data. Because the location of the delamination is asymmetric, certain function transformation and extension are inevitable to make the decomposition possible (referring to Figure 5.10).

5.4 Energy release rates and mode mixity

In this section the effects of different loading scenarios and delamination locations on the mode mixity are presented and compared to FEA solution. Other models from the literature, which are mostly based on Euler-Bernoulli theory, are also depicted. These solutions can be found in Appendix B.3.

5.4.1 Transversely isotropic beam

Those loading cases which cause pure mode-I and pure mode-II energy release rate were already discussed as examples. In order to extend the ivestigation, mode mixity of symmetric delamination with different loadings are illustrated by Figure 5.15. As it is shown, the higher-order theories represent a perfect agrement with the other solutions form the literature, which were proposed by Williams and Suo-Hutchinson. The VCCT technique predict a really small difference compare to the others [14].

The results of mode mixity in the case of asymmetric delaminated beam with different loading scenarios are depicted by Figure 5.15. This is the point where the theories significantly separate from each other and predict different mode mixity. Figure 5.15a illustrates the FSDT and SSDT results and Figure 5.15b represents the TSDT and numerical results. In order to help the comparison each figure shows the literature solutions, as well. In conclusion, the higher-order theories are in the small vicinity of the Suo-Hutchinson solution and the set of numerical results.

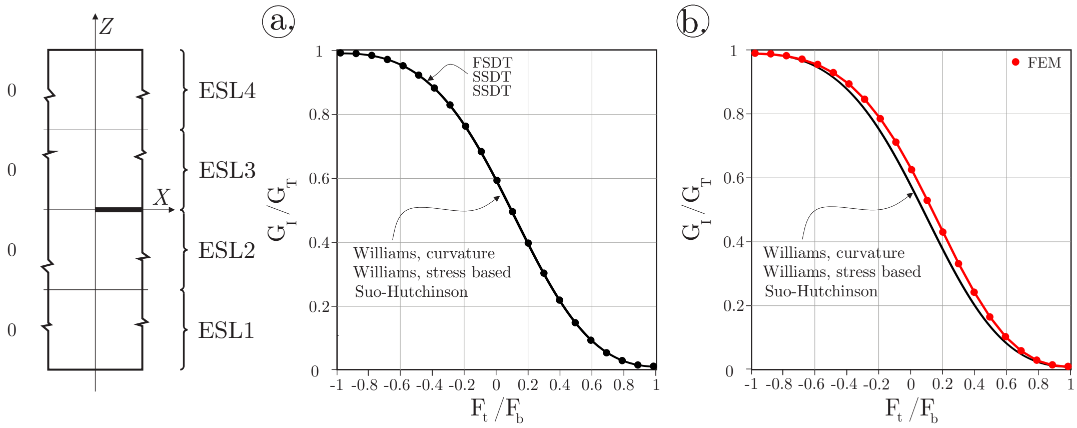

FIGURE 5.15: Mode mixity of symmetrically delaminated beam in different loading scenarios using analytical (a) and numerical (b) solutions, $a/l = 1/3$, $2h = 6$ mm.

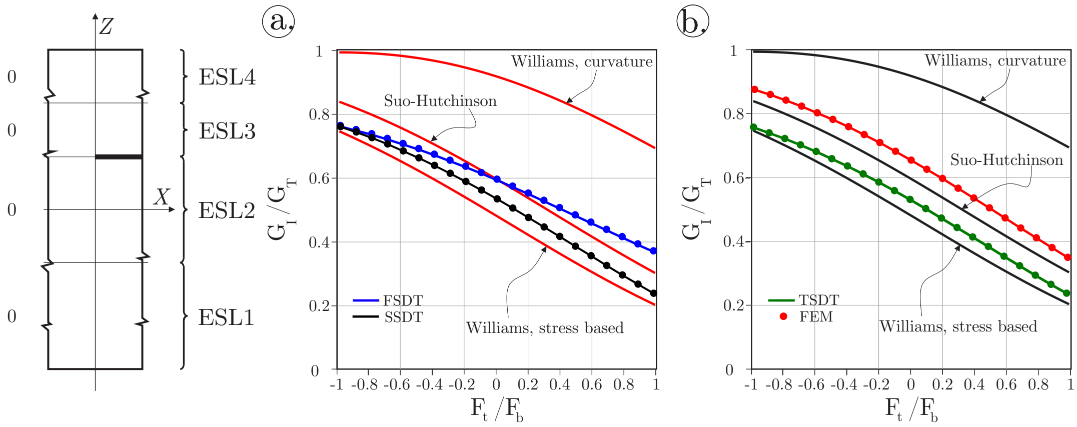

FIGURE 5.16: Mode mixity of asymmetrically delaminated beam in different loading scenarios using analytical (a) and numerical (b) solutions, $t_t/t_b = 0.5$, $a/l = 1/3$, $2h = 6$ mm.

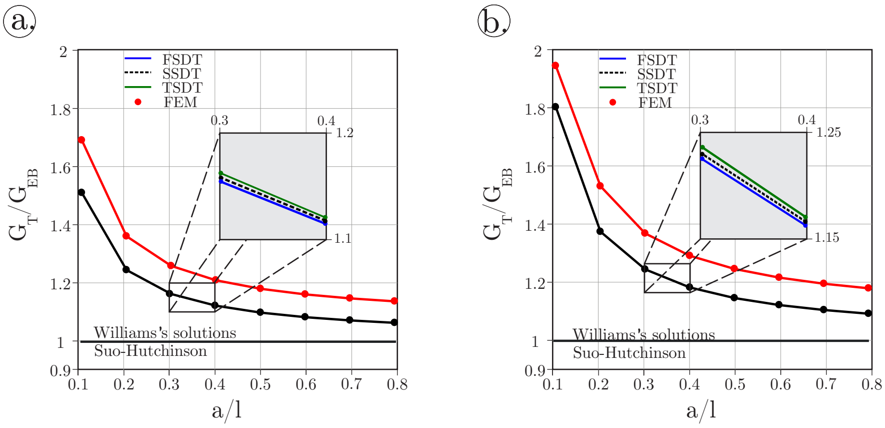

FIGURE 5.17: The ratio of the G_T total and G_{EB} classical energy relase rates with $2h = 4$ mm (a) and with $2h = 6$ mm total thickness, $F_t/F_b = -1$.

In order to get picture about the magnitude of G_T total energy relase rate the Figure 5.17 can be considered. Here the effect of a/l ratio on G_T is investigated with fixed $F_t/F_b = -1$ loading case. The results are normalized by the classical Euler-Bernoulli theory. Thus, the higher-order solutions, similarly to the numerical set of data, predict higher energy relase rates if the a length of delamination decreases compared to the l total length of the beam. It can be explained by the effect of shear forces. The higher-order theories are already able to take into account the strain energy which comes from the shear deformation. Other solutions in the literature are not because they deal only with that energy which comes from bending. By increasing the $2h$ total thickness of the beam the importance of this effect becomes higher and higher.

5.4.2 Bi-material beam

In the case of bi-material beam similar effects can be investigated. Figure 5.18 depicts the case of symmetric and Figure 5.19 represents the case of asymmetric delamination. Comparing the results with the transversely isotropic counter parts (Figure 5.15 and 5.16), significant changes can be identified. It can be attributed to the change of material properties. It is important to highlight, even those solutions which are propesed by the actual literature predict really different mode-mixities. These curves are located quite far from the numerical and the higher-order solutions. Finally, in the case of the magnitude of G_T total energy release rate, absolutely the same figure with the same tendencies could be depicted as Figure 5.17.

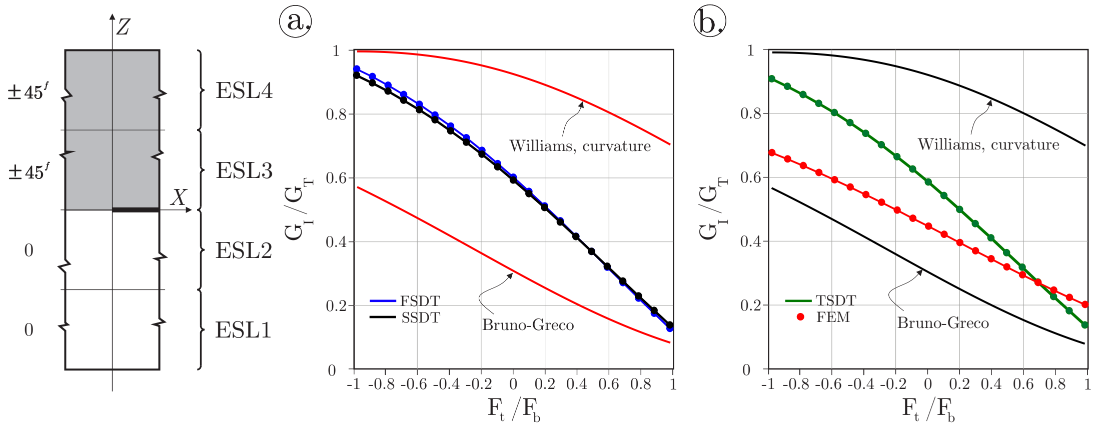

FIGURE 5.18: Mode mixity of symmetrically delaminated bi-material beam in different loading scenarios using analytical (a) and numerical (b) solutions, $a/l = 1/3$, $2h = 6$ mm.

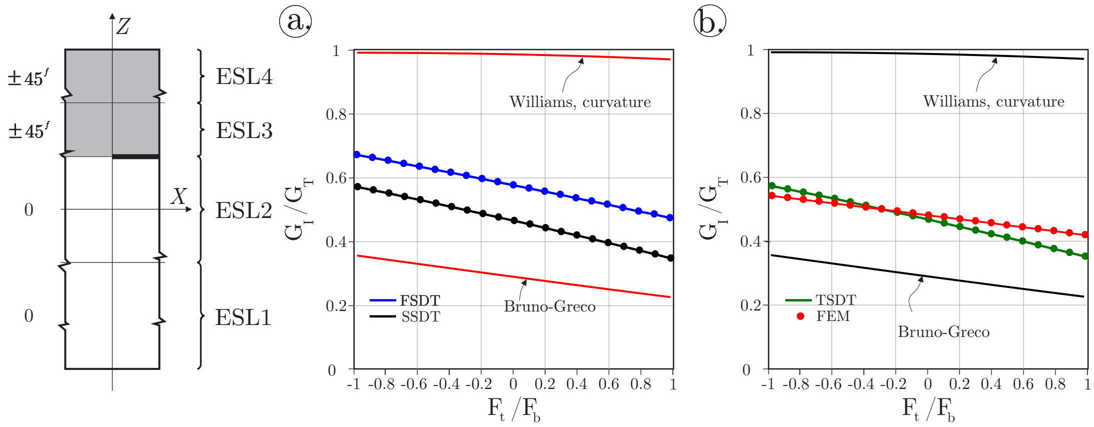

FIGURE 5.19: Mode mixity of symmetrically delaminated bi-material beam in different loading scenarios using analytical (a) and numerical (b) solutions, $a/l = 1/3$, $2h = 6$ mm.

Chapter 6

Asymmetric Double Cantilever Beam

This chapter deals with the asymmetric double cantilever beam (ADCB) specimen. Using the intorduced 4ESLs method the effect of asymmetric delamination arrangement on mode mixity can be investigated. This type of configuration is quite common and represents an important role within the fracture mechanics community because of its simplicity. It can be easily implemented by using displacement controlled testing machine.

6.1 Analytical solution

The geometry of the problem with the associated structure of ESLs is depicted in Figure 6.1, where l is the total length, b denotes the width and $2h$ represents the total thickness of the beam. As it was discussed previously, the delamination splits the structure into a top and bottom sub-laminate. The corresponding thicknesses are denoted by t_t and t_b. Similarly to the built-in configuration, the beam can be made out from one and two types of material, as well. These cases are distinguished from each other in the remaining discussion in terms of mode mixity. The material properties can be found in Table 5.1.

First, the required boundary conditions have to be imposed. Contrary to the built-in configuration, now the end of the undelamianted region is free. Without constrains, the free end must be unloaded. Equivalent stress resultants cannot take place. In the case of normal

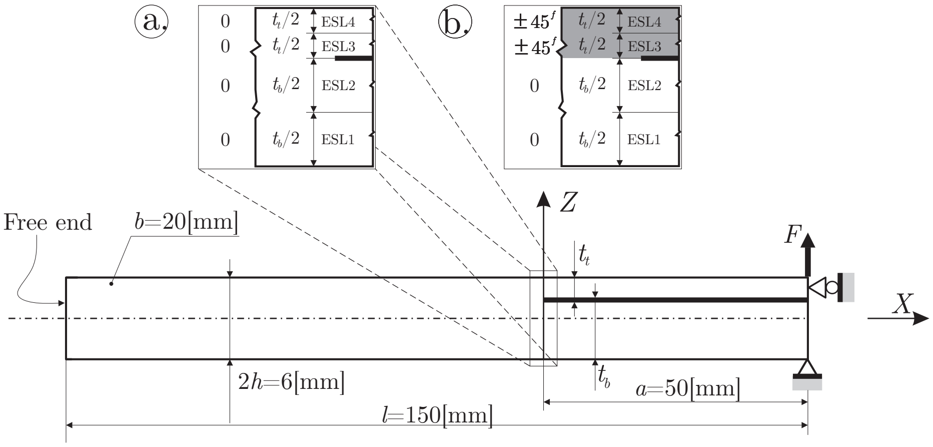

FIGURE 6.1: Geometry and ESLs structure of the ADCB specimen with one material (a) and with two different material (b).

forces and shear forces these conditions can be formulated as:

$$\sum_{i=1}^{4}\left(N_{x(i)}\right)\Bigg|_{x=-l+a}^{(undel)}=0,\qquad \sum_{i=1}^{4}\left(Q_{x(i)}\right)\Bigg|_{x=-l+a}^{(undel)}=0, \tag{6.1}$$

imposing two conditions for each theory. For equivalent bending moments it can be expressed:

$$\sum_{i=1}^{4}\left(K_{ij}^{(0)}\ K_{ij}^{(1)}\ K_{ij}^{(2)}\ K_{ij}^{(3)}\right)\Big|^{(undel)}\cdot\left(\begin{array}{c} N_{x(i)}\\ M_{x(i)}\\ L_{x(i)}\\ P_{x(i)}\end{array}\right)\Bigg|_{x=-l+a}^{(undel)}=\left(\begin{array}{c}0\\0\\0\\0\end{array}\right)\qquad j=1..q_{del}, \tag{6.2}$$

representing four conditions for FSDT and five-five conditions for SSDT, TSDT higher-order theories. The top sub-laminate of the delaminated portion at the other side of the beam is loaded by F_T force. Causing F_T equivalent shear force in the top part, it can be expressed by:

$$\sum_{i=3}^{4}\left(Q_{x(i)}\right)\Bigg|_{x=a}^{(del)}=F_t. \tag{6.3}$$

It represent only one condition for each theory. At the end of delaminated portion there is no acting bending moment, therefore it can be written:

$$\sum_{i=1}^{4}\left(K_{ij}^{(0)}\ K_{ij}^{(1)}\ K_{ij}^{(2)}\ K_{ij}^{(3)}\right)\Big|^{(del)}\cdot\left(\begin{array}{c} N_{x(i)}\\ M_{x(i)}\\ L_{x(i)}\\ P_{x(i)}\end{array}\right)\Bigg|_{x=a}^{(del)}=\left(\begin{array}{c}0\\0\\0\\0\end{array}\right)\qquad j=1..q_{del}, \tag{6.4}$$

representing zero equivalent bending moments. The condition above includes the stress resultants of the top and bottom arms, as well, represengting four conditions for FSDT and six-six conditions for SSDT and TSDT theories. Moreover, in the X direction the displacements have to be constrained at the top and bottom parts also:

$$u_{0b}\Big|_{x=a}^{(del)}=0,\qquad u_{0t}\Big|_{x=a}^{(del)}=0, \tag{6.5}$$

meaning two additional conditions. Finally, at the end of bottom sub-laminate, the tranverse deflection has to be fixed with the condition below:

$$w_b\Big|_{x=a}^{(del)}=0. \tag{6.6}$$

The continuity conditions at delamination tip between the delaminated and undelaminated regions can be expressed exactly the same way as it was discussed in the case of the built-in configuration. Eqs.(5.1)-(5.12) are appropriate for the ADCB specimen, as well. The applied theories with the number of unknown functions and differential equations are

	FSDT	SSDT	TSDT
No. of Unknown functions	6+8	7+10	7+10
No. of Differential equations	6+8	7+10	7+10
No. of Boundary conditions	㉘	㉞	㉞
Cont. conditions $(x = 0)$	14	17	17
Free-end shear force $(x = -l + a)$	1	1	1
Free-end normal force $(x = -l + a)$	1	1	1
Free-end equivalent bendings $(x = -l + a)$	4	5	5
Bottom del. deflection $(x = a)$	1	1	1
Bottom del. membrane $(x = a)$	1	1	1
Bottom del. equivalent bendings $(x = a)$	2	3	3
Top del. shear force $(x = a)$	1	1	1
Top del. membrane $(x = a)$	1	1	1
Top del. equivalent bendings $(x = a)$	2	3	3
Σ	㉘	㉞	㉞

TABLE 6.1: Summary of the necessary continuity and boundary conditions for ADCB specimen.

summarized by Table 6.1. This table contains the number of conditions coming from the continuity and the boundary conditions, as well.

6.2 FEA solution

In order to verify the analytical results of the ADCB specimen FE analyses can be carried out. The structure of the mesh with the necessary boundary conditions are depicted in Figure 6.2. It also contains the applied Davidson mesh to determine energy release rates and mode mixity. The FEA model is applicable for bi-material case, as well. The scheme and relevant equations of VCCT technique can be found in Appendix B.3. The material conditions are given in Table 5.1.

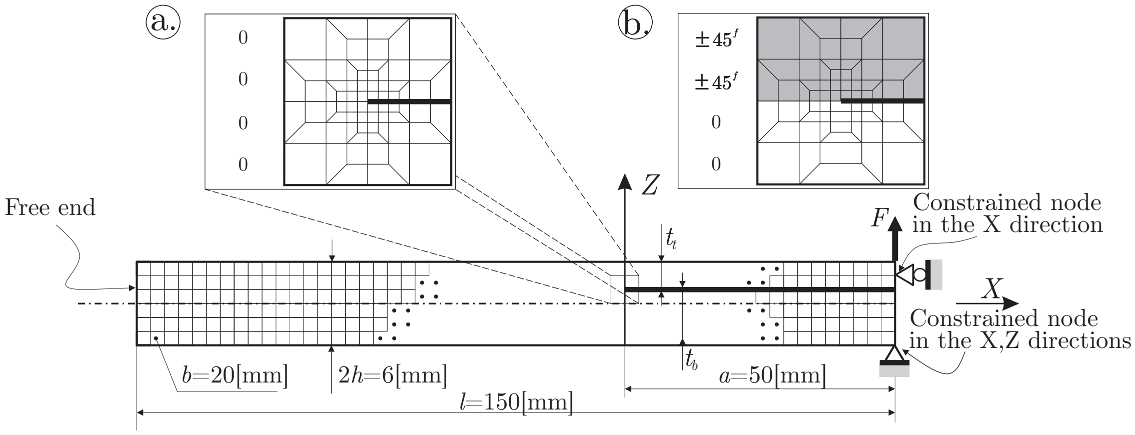

FIGURE 6.2: Discretization of the ADCB specimen with only one materials (a) and using two different material (b) with the applied Davidson mesh at the crack tip.

6.3 Energy release rates and mode mixity

In this section the effect of different delamination location on mode partitioning are investigated. In the case of the ADCB specimen the mode mixity can be varied by using different kind of materials for the top and bottom sub-laminate with different thicknesses.

Figure 6.3 represents the normalized energy release rate of tranversely isotropic ADCB specimen. If the t_t/t_b ratio decreases, apart from the Williams curvature solution, most of the theories predict decrease of G_I energy relase rate. From experimental point of view selection of the evaluation method is really crucial. Williams's methods, compared to each other, can result even more than 60 percentage difference. Actually in the literature, the more acceptable solution is the Suo-Hutchinson models. Results of the higher-order theories and the numerical set of data agree quite well with this solution.

Figure 6.3 depicts the case of bi-material. Here, the situation can be even worse. Using Bruno-Greco solution and Williams curvature based solution can result even 80 percentage difference. The result of the higher-order theories are located between these solution curves.

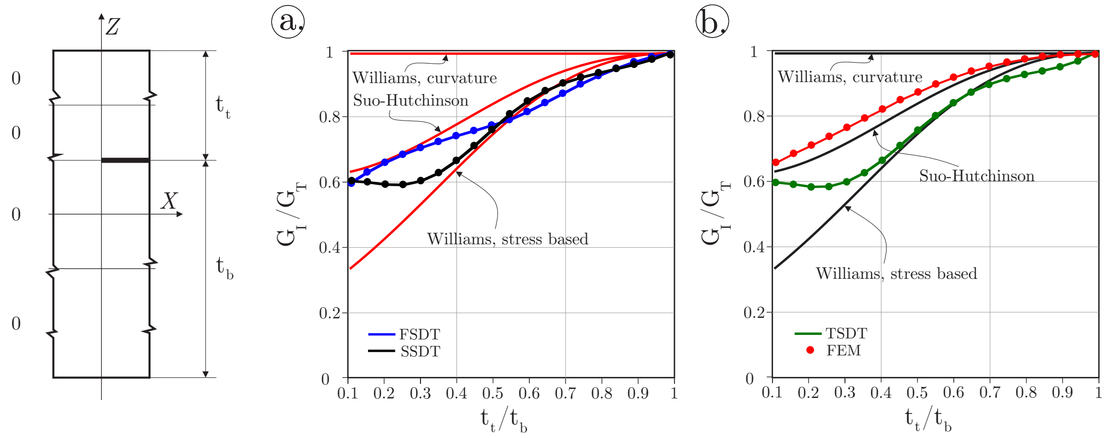

FIGURE 6.3: The effect of different delamination location on mode partitioning in the case of tranversely isotproic material using FSDT, SSDT (a) and TSDT (b), $a/l = 1/3$, $2h = 6$ mm.

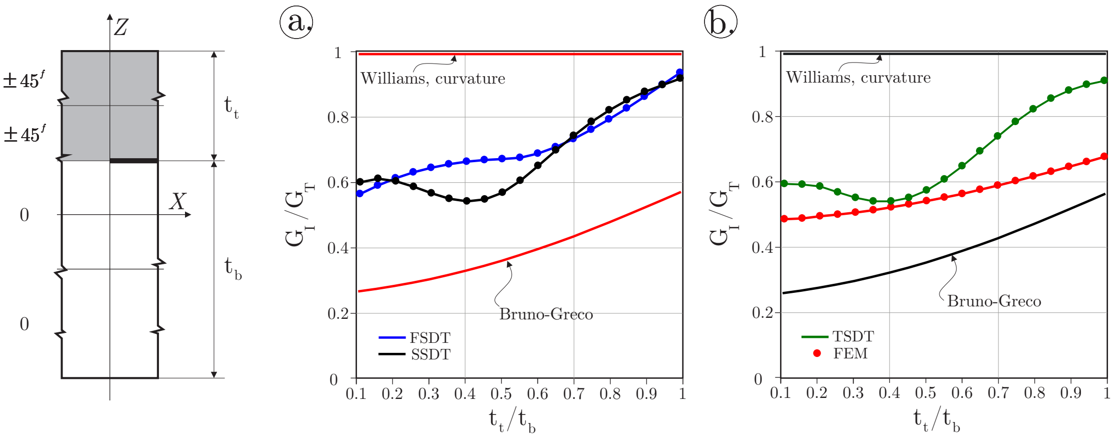

FIGURE 6.4: The effect of different delamination location on mode partitioning in the case of bi-material using FSDT, SSDT (a) and TSDT (b), $a/l = 1/3$, $2h = 6$ mm.

Chapter 7

Measurements

In this chapter the previously introduced ADCB and ELS specimens are used to measure energy release rates of transversely isotropic UD glass and bi-material specimens. The top sub-laminate of the bi-material beam is made from UD glass, furthermore, the bottom sub-laminate is made from UD carbon. (The ELS specimen is applicable only for transversely isotropic beam with symmetric delamination for pure mode-II condition.) Determination of the basic fracture mechanical properties is based on the newly developed TSDT theorem and decomposition of the J-integral into symmetric and asymmetric portions. (According to the discussed examples before, based on individual decision, it is assumed to be the most accurate technique among the other higher-order theories.) The results of this evaluation method are compared to the VCCT technique and other solutions from the actual literature. Finally conclusions are deducted and further possible improvements are proposed from experimental point of view.

7.1 Manufacturing of the composite specimens

Specimens for this study were made by simple wet lay-up process using general purpose unsaturated polyester (UP) resin, produced by Novia, as matrix and unidirectional

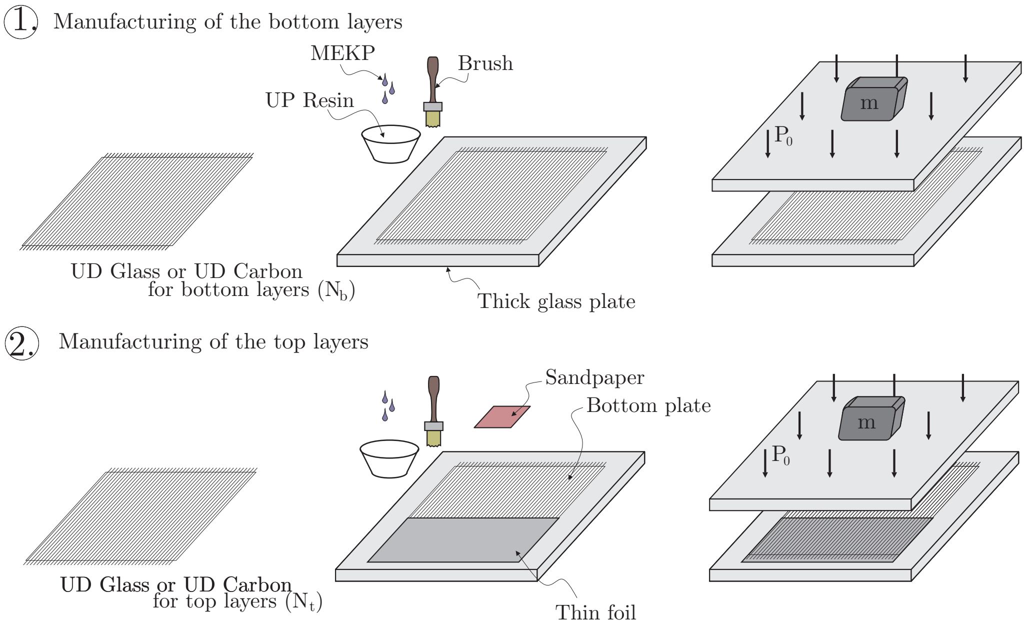
①
Manufacturing of the bottom layers
MEKP
Brush
UP Resin
m
P_0
UD Glass or UD Carbon for bottom layers (N_b)
Thick glass plate
②
Manufacturing of the top layers
Sandpaper
Bottom plate
m
P_0
UD Glass or UD Carbon for top layers (N_t)
Thin foil

FIGURE 7.1: Manufacturing of the composite specimens

	E [GPa]	ν [GPa]	G [-]	V [-]
0 UP Resin	3	0.35	1.11	0.6
UD Glass	72	0.21	29.75	0.4
UD Carbon	242	0.2	100.83	0.4

TABLE 7.1: Elastic properties of the resin and fibers with the specific volume fractions

glass (UD Glass) and carbon fibre (UD Carbon) as reinforcements. The initiator for curing process was diisobutyl dissolved methyl ethyl ketone peroxide (MEKP). The initiator of the UP was used in 1.5 weight percent which was calculated from the global weight of the UP resin. The UD glass was produced by Saertex with 397 g/m^2 specific weight and the UD carbon was produced by Zoltek with 355 g/m^2 specific weight. According to the Figure 7.1, the whole lamina was manufactured in 2 separate steps. First, the bottom sub-laminate was produced on a quite thick glass plate using N_b number of plies. Before this procedure, the glass plate had been treated with Loctite 770 solvent to make the surface suitable for wet lay-up process. The layers were impregnated by brush. In order to apply additional pressure during the curing simple weights were used. The bottom lamina had 14h curing time at room temperature, afterwards, it was cured at $60-70°C$ for 4h. The artificial delamination was created before the second wet lay-up process by putting a thin foil on the bottom plate. Furthermore, a sandpaper was used to rub the interface part of the bottom plate to help bonding with the top layers in the undelaminated region. Finally, top layers were laminated with the same technique and curing process using N_t number of plies. From the manufactured delaminated lamina test specimens were cut off.

7.2 Material parameters

As a first step in the evaluation process of the measurement results, the elastic properties of the materials have to be determined. In this study, the E_{11} flexural modulus of the tested specimens was deteremined from a simple three-point bending test using uncracked specimens, separately for UD carbon and UD glass layers. The value was calculated based on the slope of the measured load-displacement curves using classical Euler-Bernoulli beam theory. The additional properties were predicted using rule of mixtures and inverse rule of mixtures [3]. For ν_{12} Poisson's ratio the rule of mixtures can be formulated as:

$$\nu_{12} = V_f \nu_f + V_m \nu_m, \tag{7.1}$$

furthermore, for E_{22} moduli the inverse rule of mixtures is:

$$E_{22} = \frac{E_f E_m}{E_m V_f + E_f V_m}, \tag{7.2}$$

and finally, for G_{12} in-plane shear modulus becomes:

$$G_{12} = \frac{G_f G_m}{G_m V_f + G_f V_m}, \tag{7.3}$$

	E_{11} [GPa]	E_{22} [GPa]	E_{33} [GPa]	G_{23} [GPa]	G_{13} [GPa]	G_{12} [GPa]	ν_{23} [-]	ν_{13} [-]	ν_{12} [-]	t_{ply} [mm]
UD Glass ply	20.11	7.2	7.2	2.77	2.68	2.68	0.3	0.3	0.3	0.442
UD Carbon ply	76.81	2.74	2.74	1,06	2.75	2.75	0.29	0.29	0.29	0.429

TABLE 7.2: Elastic properties and thickness of single UD glass/UP and UD carbon/UP plies.

where V_f, V_m denote the specific volume fraction of the fibers and matrix, G_f, ν_f are the material parameters of the fibers and G_m, ν_m of the UP matrix. The values of these quantities can be found in Table 7.1. Taking advantage of the transversely isotropic material behaviour, the remaining parameters can be determined also:

$$E_{33} := E_{22}, \qquad G_{13} := G_{12}, \qquad \nu_{23} \approx \nu_{13} := \nu_{12}, G_{23} := \frac{E_{22}}{2(1+\nu_{23})}. \tag{7.4}$$

Each of the elastic parameters and t_{ply} thickness for UD Glass and UD Carbon ply can be found in Table 7.2. The thickness of one ply was determined by simple geometric measurement using caliper.

7.3 Measurement results

The applied measurement setups are depicted in Figure 7.2. In the case of ADCB specimen, as it is shown by Figure 7.2a, additional hinges were used. The piano hinges were fixed by two-component adhesive. The specimens were subjected to displacement controlled load. The F_c critical force was determined according to displacement-force curve. Because of the displacement controlled investigation of the beams if the delamination initiated and the crack propagation started a load drop occurs. Then the test was stopped and the initiation was checked by visual inspection, as well. A typical load-displacement curve for UD glass DCB specimen and a quite visible crack propagation for bi-material case are illustrated by Figure 7.3 and 7.4. (The DCB abbreviation represent that subcase of ADCB investigation when the location of the delamination is symmetric and the top and bottom sub-laminates are made from the same material resulting pure mode-I energy release rate).

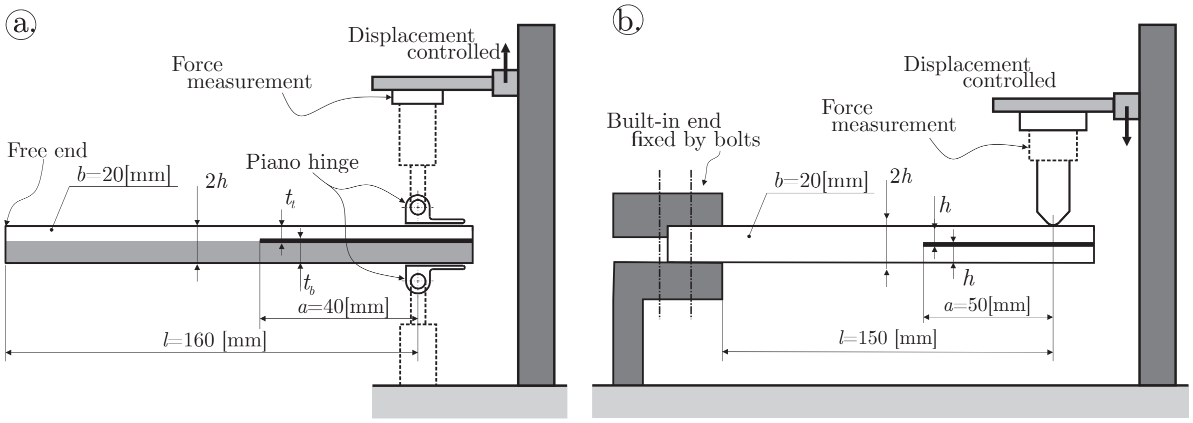

FIGURE 7.2: The measurement setup for ADCB specimen (a) and for ELS specimen (b).

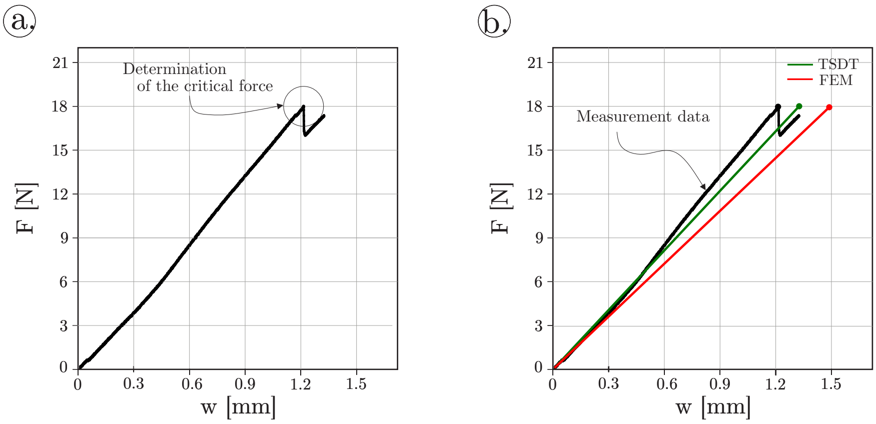

FIGURE 7.3: A typical load-displacement curve for UD glass DCB specimen (a) and its comparison with the evaluation techniques (b).

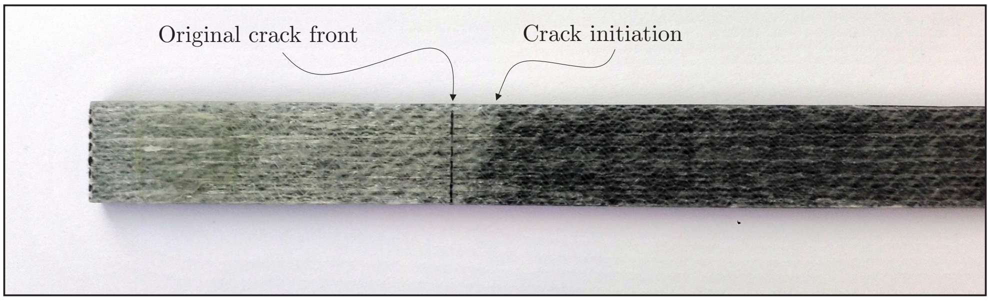

FIGURE 7.4: Original straight crack front and the occured crack initiation in the case of bi-material ADCB specimen.

N_t and type	6 UD Glass	4 UD Glass	2 UD Glass	7 UD Carbon	5 UD Carbon	2 UD Carbon
t_t $[mm]$	2.650	1.767	0.883	3.000	2.143	0.857
N_b and type	6 UD Glass	8 UD Glass	10 UD Glass	4 UD Glass	6 UD Glass	10 UD Glass
t_b $[mm]$	2.650	3.533	4.417	1.767	2.650	4.417
$2h$ $[mm]$	5.300	5.300	5.300	4.767	4.793	5.274
① F_c $[N]$	17.77	13.03	5.80	10.04	12.18	7.22
② F_c $[N]$	19.35	14.23	4.98	8.52	12.83	10.29
③ F_c $[N]$	18.98	15.31	5.75	9.14	11.05	7.48
Avarage F_c $[N]$	18.70	14.19	5.51	9.27	12.02	8.33

TABLE 7.3: The measured F_c critical forces for ADCB specimens with the corresponding layer structures and thicknesses.

In Figure 7.3a the measured slope of the DCB specimen is compared to the TSDT theory and the numerical analysis. The visible stiffening can be attributed to the fixed piano hinges. Other uncertainties can be caused by the estimated material parameters using rule of mixtures and inverse rule of mixtures. In the matter of ELS specimen displacement controlled

	① F_c $[N]$	② F_c $[N]$	③ F_c $[N]$	Avarage F_c $[N]$
ELS specimen	165	170	160	165

TABLE 7.4: The measured F_c critical forces for UD glass ELS specimens with symmetric delamination.

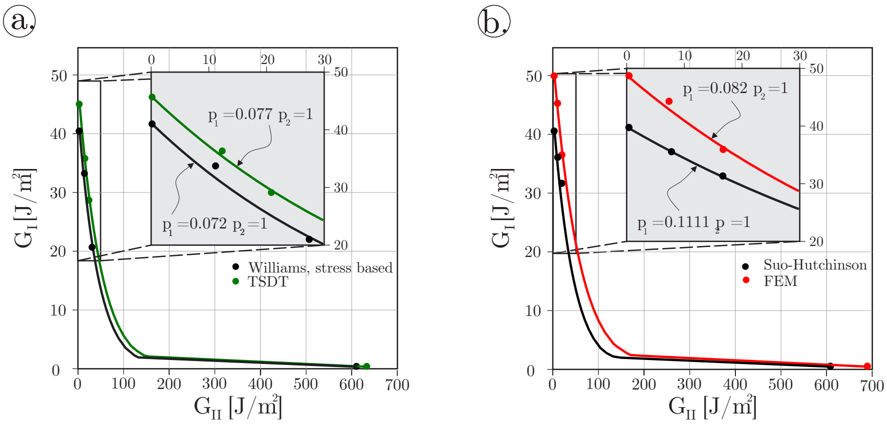

FIGURE 7.5: The mode mixity and the fitted interlaminar fracture envelopes for UD glass specimen using different evaluation techniques.

compression was applied. The F_c critical force was determined by visual inspection. As the crack propagation was always unstable the determination of the critical point was quite clear.

Each and every case three specimens were investigated and the F_c forces were determined according to the previously discussed methods. Table 7.3 contains the measurement data with the corresponding structure and geometry of the ADCB specimens and Table 7.3 contains the measurement results of ELS specimen. The calculation of the energy release rates was performed using the mean value of the three measurement data. The results of different evaluation techniques for UD glass specimens are illustrated by Figure 7.5. Comparison of the mode-mixity using TSDT and Williams' stress based solution is pedicted by Figure 7.5a. As it was mentioned previously, the TSDT solution was selected, based on individual decision, as the most accurate solution among the higher-order theories. Figure 7.5b shows the results of Suo-Hutchinson and VCCT techniques. Williams' curvature based solution was not utilized beacuse, as it was illustrated by Figure 6.3, this method always predicts only mode-I energy release rate for ADCB specimens. Hence, it is absolutely useless from mode mixity point of view. In accordance with Figure 5.17, a small energy relase rate increase can be experienced using higher-order theory or VCCT technique. In each case, based on the presented experimental results, fracture envelopes might be fitted or established [9]. Using power criterion in G_I-G_{II} plane the envelopes can be formulated as:

$$\left(\frac{G_{II}}{G_{IIc}}\right)^{p_2} + \left(\frac{G_I}{G_{Ic}}\right)^{p_1} = 1, \tag{7.5}$$

where G_{Ic}, G_{IIc} denote the critical value of pure mode-I and mode-II cases, which are associated to the actual evaluation technique and measured by DCB and ELS specimens. The p_1 and p_2 constants can be determined by minimizing the error between the envelope and the measurement points. (Because the limited number of measurement data only p_1 value was

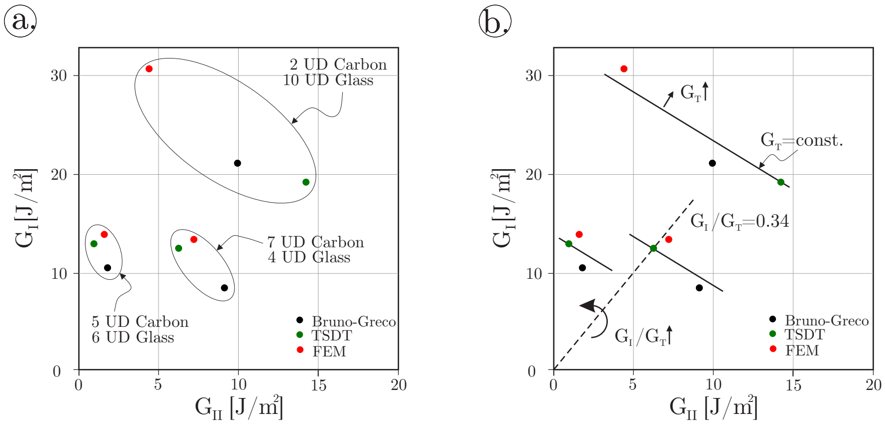

FIGURE 7.6: The evaluated mode mixity in the case of bi-material specimens using UD carbon and UD glass plies (a) and the corresponding $G_T = const.$ contour lines (b).

fitted using least square method. The p_2 value was fixed with $p_2 = 1$ value in each case.) The approximated fracture envelopes can be found also in Figure 7.5.

Figure 7.6 depicts the calculated mode mixity in the case of bi-material. The evaluation was performed by Bruno-Greco solution, TSDT theory and VCCT. At a first look, the results seem to be chaotic. In order to help the understanding, in Figure 7.6a ellipse denotes those results which correspond to a given specimen structure. Moreoverr, Figure 7.6b represents $G_T = const.$ contour lines. According to these lines and referring to Figure5.17, the numerical evaluation predict a bit higher and Bruno-Greco a bit lower value compare to the TSDT theory. (As a reminder, the Bruno-Greco solution uses the classical Euler-Bernoulli theory to determine G_T.) Referring to Figure 6.4, the differences between the selected methods are dramatically increasing in terms of thicknesses. The "2 UD Carbon, 10 UD Glass" specimen represents an extreme example when the ratio of the top and bottom layer thicknesses is small. It finally cause pretty huge mode mixity differences. Based on the obtained results, construction of the approximated fracture envelope is not clear enough. The selection among the possible evaluation methods is not straightforward and strongly change the structure of the G_I-G_{II} plane.

According to the measurement data, including the analysis of transversely isotropic and bi-material specimens also, the following recommendations can be stated in terms of evaluation techniques:

- Apart from the Williams's curvature based solution, each of the classical and higher-order solution is applicable to investigate ADCB specimens to determine that part of the fracture envelope curve which contains more G_I mode than G_{II} mode (referring to Figure 7.5).

- In the case of transversely isotropic beam using only ADCB and ESL specimens the curve fitting of the fracture envelope is more or less possible. Nevertheless, in order to increase the accuracy of the envelope, some other tests have to performed. Application of mixed-mode bening specimen (MMB) would be desirable and convenient to determine that part of the curve which contains more G_{II} mode than mode G_I [14].

- In the matter of relatively short delamination length compared to the total length of the beam one of the higher-order solutions is recommended to use. It can be concluded for each specimen type and material structure (referring to Figure 7.6 and 7.5).

- In the case of the bi-material specimens, selection of the evaluation method is absolutely crucial. There is no generally accepted solution in the litelature. Even nowadays, it is a pioneering research topic from fracture mechanics point of view.
- The final goal would be the fracture mechanical caharcterization of the laminated composite beams with multi directional layers. Based on the experiment of bi-material specimens it looks a quite hard task. The generalization of the applied techniques for laminated composite beams with quite complex lay-up sequence can be found in Appendix C.

Summary

In this student scientific report interlaminar fracture in composite beams was investigated. Based on the virtual work principle new semi-layerwise models were developed assuming the displacement field in the form of higher-order polynomials. The equivalent single layers were connected to each other via the exact kinematic conditions. The deflections were assumed with only one term in each portion. During the examples the undelaminated portion was modelled using four equivalent single layers. To describe the top and bottom sub-laminates on the delaminated portion two-two equivalent single layers were applied. The portions were connected to each other at delamination front by expressing continuity of the displacement fields and continuity between the eqivalent stress resultants. This moldel was applied for built-in configuration and for asymmetric double cantilever beam, as well.

To perform fractual mechanical investigation the J-integral was applied. The obtained total energy release rate, which is the basic property of the linear elastic fracture mechanics, was separated into mode-I and mode-II components. By using symmetric and asymmetric decomposition of the strain and displacement fields it became possible resulting more exact solutions compared to the actual soloutions in the literature. In terms of the different configurations, lay-up structures, geometries and loading scenarios the mode mixity was investigated and explored. The results of higher-order theories, numerical technique and classical solutions were depicted together.

Fracture mechanical tests were carried out for transversely isotropic and bi-material specimens. The specimens were manufactured by wet lay-up. During the measurements the critical force was determined according to the load-displacement curve and visual inspection. The newly developed models were used to evaluate the measurement data of asymmetric double cantilever beam and end load split specimens. The analysis was carried out using numerical technique and other evaluation methods from the literature, as well. In the case of transversely isotropic beam fracture envelopes were proposed assuming power criterion. Physical interpretation of the bi-material results was slightly more complicated. In terms of the findings and possible further applications advices were proposed.

Összefoglalás

Dolgozatomban delaminációt tartalmazó kompozit rudak leírására alkalmas mechanikai modellekkel foglalkoztam. A virtuális munka elvének felhasználásával, valamint az elmozdulásmezők magasabb rendű polinomok alakjában való közelítésével szemi-réteg modell került kfejlesztésre. Az egyes rétegek közötti kapcsolatot az egzakt kinematikai peremfeltétel rendszer segítségével biztosítva, a példák során a nem delaminált rész leírására négy egyenértékű réteg, míg a delaminált részek leírására két-két egyenértékű réteg került alkalmazásra. A repedéscsúcs keresztmetszetében a két modell egymáshoz lett illesztve előírva az elmozdulásmezők és az egyenértékű igénybevételek folytonosságát. A modell transzverzálisan izotróp és két külöböző anyagot tartalmazó befogott tartón került bemutatásra.

A J-integrál alkalmazásával a lineáris törésmechanika alapvető mennyisége, a repedésfeszítő erő vagy más néven energia felszabadulási ráta került számszerűsítésre. Ennek alkalmazásával továbbá lehetőség nyílt annak I-es és II-es módusokra való szétválasztására, amely így az eddigi módszerekhez képest jóval egzaktabb megoldásnak tekinthető. Ehhez a repedéscsúcsban lévő fajlagos alakváltozásokat és feszültségeket kellett szétbontani a repedésfrontra szimmetrikus és aszimmetrikus függvényekre. A különböző módusok aránya a rúd geometriájának, terhelésének és anyagának függvényében vizsgálatra került mind befogott mind ADCB típusú próbatestre.

A dolgozatom legvégén modelljeimet saját gyártású üvegszálas és szénszálas próbatesteken alkalmaztam, és segítségükkel meghatároztam azok alapvető törésmechanikai jellemzőit. A próbatestek kézi laminálással készültek. A mérések során a kritikus erő került meghatározásra erő-elmozdulás görbék és szemrevételezés segítségével. A kritikus erők valamint a próbatestek anyagának és geometriájának ismeretében a mérések kiértékelésre kerültek. Ennek során a szemi-réteg modell eredményei kerültek összehasonlításra numerikus és korábbi kiértékelő technikákkal. Unidirekcionális üveg esetén határgörbéket is készítettem. Két külöböző anyagot tartalmazó próbatestek esetén a fizikai értelmezés valamivel nehezebbnek bizonyult. Dolgozatom legvégén a tapasztalatok és a kapott eredmények alapján megfogalmaztam néhány iránymutatót a kísérletekre nézve.

Bibliography

[1] J.N.Reddy: Mechanics of Laminated Composite Plates and Shells - Theory and Analysis, Second edition, *Boca Raton, London, New York, Washington D.C.*, CRC Press, 2004.

[2] T.L.Anderson: Fracture Mechanincs - Fundamentals and Applications, Third Edition, *Boca Raton, London, New York, Washington D.C.*, 2005.

[3] Stephen W. Tsai: Theory of composite design, *Stranford University*, 2008.

[4] Meinhard Kuna: Finite elements in Fracture Mechanics Theory-Numerics-Applications, Springer, *Dordrecht Heidelberg New York London*, 2010.

[5] A.Szekrényes: Nonsingular delamination modeling in orthotropic composit plates by semi-layerwise analysis, DSc dissertation, *Budapest, Budapest University of Technology and Economics, Department of Applied Mechanics*, 2016.

[6] A.Szekrényes: Delamination of composite specimens, Ph. D. dissertation, *Budapest, Budapest University of Technology and Economics, Department of Applied Mechanics*, 2005.

[7] A.Szekrényes: Nonsingular crack modelling in orthotropic plates by four equivalent single layers, *Europen Journal of Mechanics A/Solids 55 73-99*, 2015.

[8] A.Szekrényes: Semi-layerwise analysis of laminated plates with nonsingular delamination - The theorem of autocontinuity, *Applied Mathematical Modelling 40, 1344–1371*, 2016.

[9] A.Szekrényes: Delamination facture analysis in the G_{II}-G_{III} plane using prestressed transparent composite beams, *International Journal of Solids and Structures 44,10, 3359-3378*, 2016.

[10] A.Leski: Implementation of the virtual crack closure technique in engineering FE calculations, *Finite Elements in Analysis and Design 43 261-268*, 2006.

[11] Domenico Bruno, Fabrizio Greco: Mixed mode delamination in plates: a refined approach, *Internation Journal of Solids and Structures 38 9149-9177*, 2001.

[12] Gergely Czél: Composite technology - Lecture notes, *Budapest University of Technology and Economics, Department of Polymer Engineering*, 2018.

[13] András Szekrényes: Mechanics of composites - Technical Manual No.1, *Budapest University of Technology and Economics, Department of Applied Mechanics*, 2018.

[14] András Szekrényes: Experimental methods in solid mechanics - Technical Manual No.3, *Budapest University of Technology and Economics, Department of Applied Mechanics*, 2018.

Appendix A

Matrix elements - Method of 4ESLs

A.1 Third-order beam theory

This Appendix collects the K_{ij} matrix elements for the third-order beam theory.

Undelaminated region

$$K_{11}^{(0)} = -z_R^{(2)} - \frac{t_1+t_2}{2}, \tag{A.1}$$

$$K_{12}^{(0)} = \frac{(t_1+t_2+z_R^{(2)})(t_1^2+2t_1t_2-2t_1z_R^{(2)}-2t_2^2-2t_2z_R^{(2)}+4[z_R^{(2)}]^2)}{12(t_1+t_2)}, \tag{A.2}$$

$$K_{13}^{(0)} = \frac{(t_1+t_2+z_R^{(2)})(2t_1^2+10t_1t_2-4t_1z_R^{(2)}+11t_2^2-4t_2z_R^{(2)}-4[z_R^{(2)}]^2)}{12(t_1+t_2)}, \tag{A.3}$$

$$K_{14}^{(0)} = \frac{(3t_3+2t_4)(t_1+t_2+2z_R^{(2)})t_3}{4(t_3+t_4)},\ K_{15}^{(0)} = -\frac{(t_1+t_2+2z_R^{(2)})t_3}{4(t_3+t_4)}, \tag{A.4}$$

$$K_{21}^{(0)} = -z_R^{(2)},\ K_{22}^{(0)} = -\frac{(3t_2^2-4[z_R^{(2)}]^2)z_R^{(2)}}{6(t_1+t_2)}, \tag{A.5}$$

$$K_{23}^{(0)} = \frac{(6t_1t_2-6t_1z_R^{(2)}+9t_2^2-6t_2z_R^{(2)}-4[z_R^{(2)}]^2)}{6(t_1+t_2)},\ K_{24}^{(0)} = \frac{(3t_3+2t_4)t_3z_R^{(2)}}{2(t_3+t_4)}, \tag{A.6}$$

$$K_{25}^{(0)} = -\frac{t_3^2z_R^{(2)}}{2(t_3+t_4)},\ K_{31}^{(0)} = \frac{t_2+t_3}{2} - z_R^{(2)},\ K_{32}^{(0)} = \frac{(t_2+z_R^{(2)})(t_2-2z_R^{(2)})^2}{t_1+t_2}, \tag{A.7}$$

$$K_{33}^{(0)} = -\frac{(t_2-2z_R^{(2)})^2(3t_1+5t_2+2z_R^{(2)})}{12(t_1+t_2)}, \tag{A.8}$$

$$K_{34}^{(0)} = -\frac{(9t_2t_3 + 6t_2t_4 + 4t_3^2 + 3t_3t_4 - 18t_3z_R^{(2)} - 12t_4z_R^{(2)})t_3}{12(t_3+t_4)}, \tag{A.9}$$

$$K_{35}^{(0)} = \frac{(3t_2 + t_3 - 6z_R^{(2)})t_3^2}{12(t_3+t_4)},\ K_{41}^{(0)} = \frac{t_2+t_4}{2} + t_3 - z_R^{(2)}, \tag{A.10}$$

$$K_{42}^{(0)} = \frac{(t_2 + z_R^{(2)})(t_2 - 2z_R^{(2)})^2}{t_1+t_2},\ K_{43}^{(0)} = -\frac{(t_2 - 2z_R^{(2)})^2(3t_1 + 5t_2 + 2z_R^{(2)})}{12(t_1+t_2)}, \tag{A.11}$$

$$K_{44}^{(0)} = -\frac{9t_2t_3^2 + 6t_2t_3t_4 + 2t_3^2 - 3t_3^2t_4 - 18t_3^2z_R^{(2)} - 6t_3t_4^2 - 12t_3t_4z_R^{(2)} - 2t_4^3}{12(t_3+t_4)}, \tag{A.12}$$

$$K_{44}^{(0)} = \frac{3t_2t_3^2 + 2t_3^3 + 3t_3^2t_4 - 6t_3^2z_R^{(2)} + 3t_3t_4^2 + t_4^3}{12(t_3+t_4)}, \tag{A.13}$$

$$K_{11}^{(1)} = 1,\ K_{12}^{(1)} = -\frac{t_1(t_1+2t_2)}{2(t_1+t_2)},\ K_{13}^{(1)} = -\frac{(t_1+2t_2)}{2(t_1+t_2)^2}, \tag{A.14}$$

$$K_{14}^{(1)} = -\frac{(3t_3+2t_4)t_3}{2(t_3+t_4)},\ K_{15}^{(1)} = \frac{t_3^2}{2(t_3+t_4)},\ K_{21}^{(1)} = 1,\ K_{22}^{(1)} = \frac{t_2^2}{2(t_1+t_2)}, \tag{A.15}$$

$$K_{23}^{(1)} = -\frac{(2t_1+3t_2)t_2}{2(t_1+t_2)},\ K_{24}^{(1)} = -\frac{(3t_3+2t_4)t_3}{2(t_3+t_4)},\ K_{25}^{(1)} = \frac{t_3^2}{2(t_3+t_4)}, \tag{A.16}$$

$$K_{31}^{(1)} = 1,\ K_{32}^{(1)} = K_{33}^{(1)} = K_{34}^{(1)} = K_{35}^{(1)} = 0,\ K_{41}^{(1)} = 1,\ K_{42}^{(1)} = K_{43}^{(1)} = 0, \tag{A.17}$$

$$K_{44}^{(1)} = \frac{t_3+t_4}{2},\ K_{45}^{(1)} = \frac{t_3+t_4}{2}, \tag{A.18}$$

$$K_{11}^{(2)} = 0,\ K_{12}^{(2)} = 1,\ K_{13}^{(2)} = K_{14}^{(2)} = K_{15}^{(2)} = K_{21}^{(2)} = K_{22}^{(2)} = 0,\ K_{23}^{(2)} = 1, \tag{A.19}$$

$$K_{24}^{(2)} = K_{25}^{(2)} = K_{31}^{(2)} = K_{32}^{(2)} = K_{33}^{(2)} = 0,\ K_{34}^{(2)} = 1, \tag{A.20}$$

$$K_{35}^{(2)} = K_{41}^{(2)} = K_{42}^{(2)} = K_{43}^{(2)} = K_{44}^{(2)}, \, K_{45}^{(2)} = 1, \tag{A.21}$$

$$K_{11}^{(3)} = 0, \, K_{12}^{(3)} = -\frac{2}{3(t_1 + t_2)}, \, K_{13}^{(3)} = \frac{2}{3(t_1 + t_2)}, \, K_{14}^{(3)} = K_{15}^{(3)} = K_{21}^{(3)} = 0, \tag{A.22}$$

$$K_{22}^{(3)} = -\frac{2}{3(t_1 + t_2)}, \, K_{23}^{(3)} = \frac{2}{3(t_1 + t_2)}, \tag{A.23}$$

$$K_{24}^{(3)} = K_{25}^{(3)} = K_{31}^{(3)} = K_{32}^{(3)} = K_{33}^{(3)} = 0, \, K_{34}^{(3)} = -\frac{2}{3(t_3 + t_4)}, \tag{A.24}$$

$$K_{35}^{(3)} = \frac{2}{3(t_3 + t_4)}, \, K_{41}^{(3)} = K_{42}^{(3)} = K_{43}^{(3)} = 0, \tag{A.25}$$

$$K_{44}^{(3)} = -\frac{2}{3(t_3 + t_4)}, \, K_{45}^{(3)} = \frac{2}{3(t_3 + t_4)}. \tag{A.26}$$

Delaminated region

$$K_{11}^{(0)} = -\frac{t_2}{2}, \, K_{12}^{(0)} = -\frac{t_2^3(3t_1 + 2t_2)}{12(t_1 + t_2)}, \, K_{13}^{(0)} = -\frac{t_2^3}{12(t_1 + t_2)}, \tag{A.27}$$

$$K_{14}^{(0)} = K_{15}^{(0)} = K_{16}^{(0)} = 0, \, K_{21}^{(0)} = \frac{t_1}{2}, \, K_{22}^{(0)} = \frac{t_1(2t_1^2 + 6t_1t_2 + 3t_2^2)}{12(t_1 + t_2)}, \tag{A.28}$$

$$K_{23}^{(0)} = \frac{t_1(2t_1^2 + 3t_1t_2 + 3t_2^2)}{12(t_1 + t_2)}, \, K_{24}^{(0)} = K_{25}^{(0)} = K_{26}^{(0)} = K_{31}^{(0)} = K_{32}^{(0)} = K_{33}^{(0)} = 0, \tag{A.29}$$

$$K_{34}^{(0)} = -\frac{t_4}{2}, \, K_{35}^{(0)} = -\frac{t_4^2(3t_3 + 2t_4)}{12(t_3 + t_4)}, \, K_{36}^{(0)} = -\frac{t_4^2}{12(t_3 + t_4)}, \tag{A.30}$$

$$K_{41}^{(0)} = K_{42}^{(0)} = K_{43}^{(0)} = 0, \, K_{44}^{(0)} = \frac{t_3}{2}, \, K_{45}^{(0)} = \frac{t_3(2t_3^2 + 6t_1t_3 + 3t_4^2)}{12(t_3 + t_4)}, \tag{A.31}$$

$$K_{46}^{(0)} = \frac{t_3(2t_3^2 + 3t_3t_4 + 3t_4^2)}{12(t_3 + t_4)}, \tag{A.32}$$

$$K_{11}^{(1)} = 1,\, K_{12}^{(1)} = K_{13}^{(1)} = K_{14}^{(1)} = K_{15}^{(1)} = K_{16}^{(1)} = 0,\, K_{21}^{(1)} = 1,\, K_{22}^{(1)} = K_{23}^{(1)} = \frac{t1 + t2}{2}, \tag{A.33}$$

$$K_{24}^{(1)} = K_{25}^{(1)} = K_{26}^{(1)} = K_{31}^{(1)} = K_{32}^{(1)} = K_{33}^{(1)} = 0,\, K_{34}^{(1)} = 1, \tag{A.34}$$

$$K_{35}^{(1)} = K_{36}^{(1)} = K_{41}^{(1)} = K_{42}^{(1)} = K_{43}^{(1)} = 0,\, K_{44}^{(1)} = 1,\, K_{45}^{(1)} = K_{46}^{(1)} = \frac{t_3 + t_4}{2}, \tag{A.35}$$

$$K_{11}^{(2)} = 0,\, K_{12}^{(2)} = 1,\, K_{13}^{(2)} = K_{14}^{(2)} = K_{15}^{(2)} = K_{16}^{(2)} = K_{21}^{(2)} = K_{22}^{(2)} = 0,\, K_{23}^{(2)} = 1, \tag{A.36}$$

$$K_{24}^{(2)} = K_{25}^{(2)} = K_{26}^{(2)} = K_{31}^{(2)} = K_{32}^{(2)} = K_{33}^{(2)} = K_{34}^{(2)} = 0,\, K_{35}^{(2)} = 1, \tag{A.37}$$

$$K_{36}^{(2)} = K_{41}^{(2)} = K_{42}^{(2)} = K_{43}^{(2)} = K_{44}^{(2)} = K_{45}^{(2)} = 0,\, K_{46}^{(2)} = 1, \tag{A.38}$$

$$K_{11}^{(3)} = 0,\, K_{12}^{(3)} = -\frac{2}{3(t_1 + t_2)},\, K_{13}^{(3)} = \frac{2}{3(t_1 + t_2)},\, K_{14}^{(3)} = K_{15}^{(3)} = K_{16}^{(3)} = K_{21}^{(3)} = 0, \tag{A.39}$$

$$K_{22}^{(3)} = -\frac{2}{3(t_1 + t_2)},\, K_{23}^{(3)} = \frac{2}{3(t_1 + t_2)}, \tag{A.40}$$

$$K_{24}^{(3)} = K_{25}^{(3)} = K_{26}^{(3)} = K_{31}^{(3)} = K_{32}^{(3)} = K_{33}^{(3)} = K_{34}^{(3)} = 0,\, K_{35}^{(3)} = -\frac{2}{3(t_3 + t_4)}, \tag{A.41}$$

$$K_{36}^{(3)} = \frac{2}{3(t_3 + t_4)},\, K_{41}^{(3)} = K_{42}^{(3)} = K_{43}^{(3)} = K_{44}^{(3)} = 0,\, K_{45}^{(3)} = -\frac{2}{3(t_3 + t_4)}, \tag{A.42}$$

$$K_{46}^{(3)} = \frac{2}{3(t_3 + t_4)}. \tag{A.43}$$

A.2 Second-order beam theory

In this Appendix the K_{ij} matrix elements for the second-order beam theory are presented.

Undelaminated region

$$K_{11}^{(0)} = -z_R^{(2)} - \frac{t_1 + t_2}{2},\ K_{12}^{(0)} = 0,\ K_{13}^{(0)} = -\frac{t_1}{4}(t_1 + 2t_2 + 4z_R^{(2)}), \tag{A.44}$$

$$K_{14}^{(0)} = -\frac{(t_2 + 2z_R^{(2)})^2}{4},\ K_{15}^{(0)} = 0,\ K_{21}^{(0)} = -z_R^{(2)},\ K_{22}^{(0)} = 0,\ K_{23}^{(0)} = -t_1 z_R^{(2)}, \tag{A.45}$$

$$K_{24}^{(0)} = -z_R^{(2)}(t_2 + z_R^{(2)}),\ K_{25}^{(0)} = 0,\ K_{31}^{(0)} = \frac{t_3}{4} + \frac{t_2}{2} - z_R^{(2)},\ K_{32}^{(0)} = \frac{t_3}{4}, \tag{A.46}$$

$$K_{33}^{(0)} = \frac{t_1}{4}(t_3 + 2t_2 - 4z_R^{(2)}),\ K_{34}^{(0)} = \frac{t_2 t_3}{2} + \frac{3t_2^2}{4} - t_2 z_R^{(2)} - [z_R^{(2)}]^2, \tag{A.47}$$

$$K_{35}^{(0)} = 0,\ K_{41}^{(0)} = \frac{t_2 - t_4}{2} - z_R^{(2)},\ K_{42}^{(0)} = t_3 + t_4,\ K_{43}^{(0)} = \frac{t_1}{2}(t_2 - t_4 - 2z_R^{(2)}), \tag{A.48}$$

$$K_{44}^{(0)} = \frac{3t_2^2}{4} - t_2 t_4 - t_2 z_R^{(2)},\ K_{45}^{(0)} = \frac{t_4^2}{4}. \tag{A.49}$$

$$K_{11}^{(1)} = 1,\ K_{12}^{(1)} = K_{13}^{(1)} = K_{14}^{(1)} = K_{15}^{(1)} = 0,\ K_{21}^{(1)} = 1,\ K_{22}^{(1)} = 0,\ K_{23}^{(1)} = t_1, \tag{A.50}$$

$$K_{24}^{(1)} = t_2,\ K_{25}^{(1)} = K_{31}^{(1)} = K_{32}^{(1)} = K_{34}^{(1)} = K_{35}^{(1)} = 0,\ K_{41}^{(1)} = -1, \tag{A.51}$$

$$K_{42}^{(1)} = 2,\ K_{43}^{(1)} = -t_1,\ K_{44}^{(1)} = -2t_2,\ K_{45}^{(1)} = t_4,\ K_{11}^{(2)} = K_{12}^{(2)} = 0, \tag{A.52}$$

$$K_{13}^{(2)} = 1,\ K_{14}^{(2)} = K_{15}^{(2)} = K_{21}^{(2)} = K_{22}^{(2)} = K_{23}^{(2)} = 0, \tag{A.53}$$

$$K_{24}^{(2)} = 1,\ K_{25}^{(2)} = 0,\ K_{31}^{(2)} = -\frac{1}{t_3},\ K_{32}^{(2)} = \frac{1}{t_3},\ K_{33}^{(2)} = -\frac{t_1}{t_3},\ K_{34}^{(2)} = -\frac{2t_2}{t_3}, \tag{A.54}$$

$$K_{35}^{(2)} = K_{41}^{(2)} = K_{42}^{(2)} = K_{43}^{(2)} = K_{44}^{(2)} = 0,\ K_{45}^{(2)} = 1 \tag{A.55}$$

Delaminated region

$$K_{11}^{(0)} = -\frac{t_2}{2},\ K_{12}^{(0)} = -\frac{t_2^2}{4},\ K_{13}^{(0)} = K_{14}^{(0)} = K_{15}^{(0)} = K_{16}^{(0)} = 0,\ K_{21}^{(0)} = \frac{t_1}{2}, \tag{A.56}$$

$$K_{22}^{(0)} = \frac{t_1^2}{4} + \frac{t_1 t_2}{2} - \frac{t_2^2}{4},\ K_{23}^{(0)} = \frac{t_2^2}{4},\ K_{24}^{(0)} = K_{25}^{(0)} = K_{26}^{(0)} = K_{31}^{(0)} = K_{32}^{(0)} = K_{33}^{(0)} = 0, \tag{A.57}$$

$$K_{34}^{(0)} = -\frac{t_4}{2},\ K_{35}^{(0)} = -\frac{t_4^2}{4},\ K_{36}^{(0)} = K_{41}^{(0)} = K_{42}^{(0)} = K_{43}^{(0)} = 0,\ K_{44}^{(0)} = \frac{t_3}{2}, \tag{A.58}$$

$$K_{45}^{(0)} = \frac{t_3^2}{4} + \frac{t_3 t_4}{2} - \frac{t_4^2}{4},\ K_{45}^{(0)} = \frac{t_4^2}{4} \tag{A.59}$$

$$K_{11}^{(1)} = 1,\ K_{12}^{(1)} = K_{13}^{(1)} = K_{14}^{(1)} = K_{15}^{(1)} = K_{16}^{(1)},\ K_{21}^{(1)} = 1,\ K_{22}^{(1)} = t_1,\ K_{23}^{(1)} = t_2, \tag{A.60}$$

$$K_{24}^{(1)} = K_{25}^{(1)} = K_{26}^{(1)} = K_{31}^{(1)} = K_{32}^{(1)} = K_{33}^{(1)} = 0,\ K_{34}^{(1)} = 1, \tag{A.61}$$

$$K_{35}^{(1)} = K_{36}^{(1)} = K_{41}^{(1)} = K_{42}^{(1)} = K_{43}^{(1)} = 0,\ K_{44}^{(1)} = 1,\ K_{45}^{(1)} = t_3,\ K_{46}^{(1)} = t_4, \tag{A.62}$$

$$K_{11}^{(2)} = 0,\ K_{12}^{(2)} = 1,\ K_{13}^{(2)} = K_{14}^{(2)} = K_{15}^{(2)} = K_{16}^{(2)} = K_{21}^{(2)} = K_{22}^{(2)} = 0, \tag{A.63}$$

$$K_{23}^{(2)} = 1,\ K_{24}^{(2)} = K_{25}^{(2)} = K_{26}^{(2)} = K_{31}^{(2)} = K_{32}^{(2)} = K_{33}^{(2)} = K_{34}^{(2)} = 0;\ K_{35}^{(2)} = 1, \tag{A.64}$$

$$K_{36}^{(2)} = K_{41}^{(2)} = K_{42}^{(2)} = K_{43}^{(2)} = K_{44}^{(2)} = K_{45}^{(2)},\ K_{46}^{(2)} = 1. \tag{A.65}$$

A.3 First-order beam theory

This Appendix collects the K_{ij} matrix elements of the FSDT solution.

Undelaminated region

$$K_{11}^{(0)} = -\frac{t_1}{2},\ K_{12}^{(0)} = -\frac{t_2}{2} - z_R^{(2)},\ K_{13}^{(0)} = K_{14}^{(0)} = K_{21}^{(0)} = 0,\ K_{22}^{(0)} = -z_R^{(2)}, \tag{A.66}$$

$$K_{23}^{(0)} = K_{24}^{(0)} = K_{31}^{(0)} = 0,\ K_{32}^{(0)} = \frac{t_2}{2} - z_R^{(2)},\ K_{33}^{(0)} = \frac{t_3}{2},\ K_{34}^{(0)} = K_{41}^{(0)} = 0, \tag{A.67}$$

$$K_{42}^{(0)} = \frac{t_2}{2} - z_R^{(2)},\ K_{43}^{(0)} = t_3,\ K_{44}^{(0)} = \frac{t_4}{2} \tag{A.68}$$

$$K_{11}^{(1)} = 1,\ K_{12}^{(1)} = K_{13}^{(1)} = K_{14}^{(1)} = K_{21}^{(1)} = 0,\ K_{22}^{(1)} = 1,\ K_{23}^{(1)} = K_{24}^{(1)} = 0 \tag{A.69}$$

$$K_{31}^{(1)} = K_{32}^{(1)} = 0,\ K_{33}^{(1)} = 1,\ K_{34}^{(1)} = K_{41}^{(1)} = K_{42}^{(1)} = K_{43}^{(1)} = 0,\ K_{44}^{(1)} = 0. \tag{A.70}$$

Delaminated region

$$K_{11}^{(0)} = -\frac{t_2}{2},\ K_{12}^{(0)} = K_{13}^{(0)} = K_{14}^{(0)} = 0,\ K_{21}^{(0)} = \frac{t_1 - t_2}{2},\ K_{22}^{(0)} = \frac{t_2}{2}, \tag{A.71}$$

$$K_{23}^{(0)} = K_{24}^{(0)} = 0,\ K_{31}^{(0)} = K_{32}^{(0)} = 0,\ K_{33}^{(0)} = -\frac{t_4}{2}, \tag{A.72}$$

$$K_{34}^{(0)} = K_{41}^{(0)} = K_{42}^{(0)} = 0,\ K_{43}^{(0)} = \frac{t_3 - t_4}{2},\ K_{44}^{(0)} = \frac{t_4}{2}, \tag{A.73}$$

$$K_{11}^{(1)} = 1,\ K_{12}^{(1)} = K_{13}^{(0)} = K_{14}^{(0)} = 0,\ K_{21}^{(1)} = 0,\ K_{22}^{(1)}1,\ K_{23}^{(1)} = K_{24}^{(0)} = 0, \tag{A.74}$$

$$K_{31}^{(1)} = K_{32}^{(1)} = 0,\ K_{33}^{(1)} = 1,\ K_{34}^{(1)} = 0,\ K_{41}^{(1)} = K_{42}^{(1)} = K_{43}^{(1)} = 0,\ K_{44}^{(1)} = 1. \tag{A.75}$$

Appendix B

Other evaluation techniques in the literature

In this Appendix the previously used reference solutions are introduced including the VCCT technique.

B.1 Suo-Hutchinson solution

The Suo-Hutchinson solution is based on the classical Euler-Bernoulli beam theory and the distributed dislocation method to perform mode partitioning of the total energy release rate in fracture specimens containing only one type of material. It is commonly called local method, as well. The general loading case is illustrated by Figure B.1, where M_t and M_b represent the tip bending moments on the top and bottom sub-laminates. A quite important property of the illustrated case is that the reference planes coincide with the neutral planes of the portions. Unfortunately, the deduction is quite complicated, so hereby only the final expressions are given:

$$G_I = \frac{1}{2b^2 E_{11}}\Big(\frac{F}{\sqrt{R_1}} cos\omega + \frac{M}{\sqrt{R_1 2}} sin(\omega+\gamma)\Big)^2, \tag{B.1}$$

$$G_{II} = \frac{1}{2b^2 E_{11}}\Big(\frac{F}{\sqrt{R_1}} cos\omega + \frac{M}{\sqrt{R_1 2}} sin(\omega+\gamma)\Big)^2, \tag{B.2}$$

where R_1 and R_2 are defined as:

$$R_1 = \frac{t_t}{1+4t_t/t_b+6(t_t/t_b)^2+3(t_t/t_b)^2}, \qquad R_2 = \frac{t_t^3 t_b^3}{12(t_t^3+t_b^3)}, \tag{B.3}$$

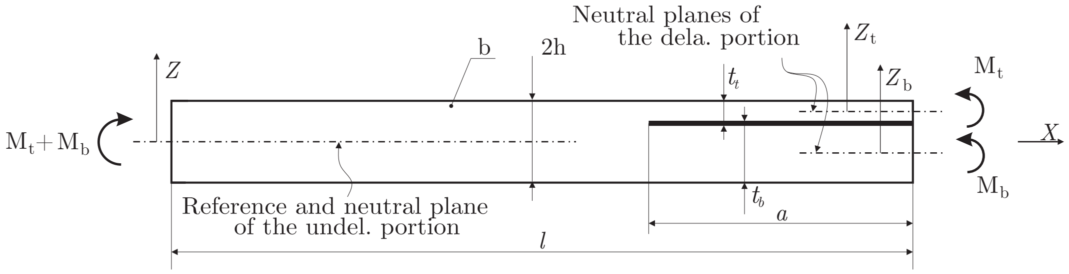

FIGURE B.1: General loading case for mixed-mode I/II specimen using only one material

furthermore γ and ω are:

$$\gamma = arcsin(\frac{6\sqrt{R_1 R_2}}{t_b^2}(1+\frac{t_t}{t_b})), \qquad \omega = \left(52.1 - 3\frac{t_t}{t_b}\right)\frac{\pi}{180}, \tag{B.4}$$

and finally F and M are:

$$F = -\frac{6(M_t + M_b)t_t t_b}{(t_t + t_b)^3}, \qquad M = M_t - \frac{(M_t + M_b)t_t^3}{(t_t + t_b)^3} \tag{B.5}$$

B.2 Williams and Bruno-Greco solutions

Unlikely to the previously introduced Suo-Hutchinson method, these solutions are suitable to describe mode partitioning in composite specimens containing two or even any kind of orthotropic plies. In these cases, it is important to highlight and emphasize, the neutral planes of the portions are not necessarily coincide with the reference planes anymore. As it is illustarted by Figure B.2, according to the actual structure of the laminated plies, they are shifted or can be shifted. By making the B_{11} coupling stiffnes with respect to the local reference planes equal to zero, each and every case the neutral plane can be found. Generally, this can be expressed as:

$$B_{11} = b\frac{1}{2}\sum_{m=1}^{N_l} \overline{C}_{11}^{(m)}([z_{m+1} + t_s]^2 - [z_m + t_s]^2) = 0, \tag{B.6}$$

where t_s denotes the unknown offset between the neutral and loacal reference plane and the other terms are equivalent with the previous notations used in Eqs.(2.15) and (2.19). Solving this equation, separately for the undelaminated and delaminated portions, t_s, t_{st} and t_{sb} can be obtained. Thus the bending stiffnesses, taking into account the offset, can be calculated

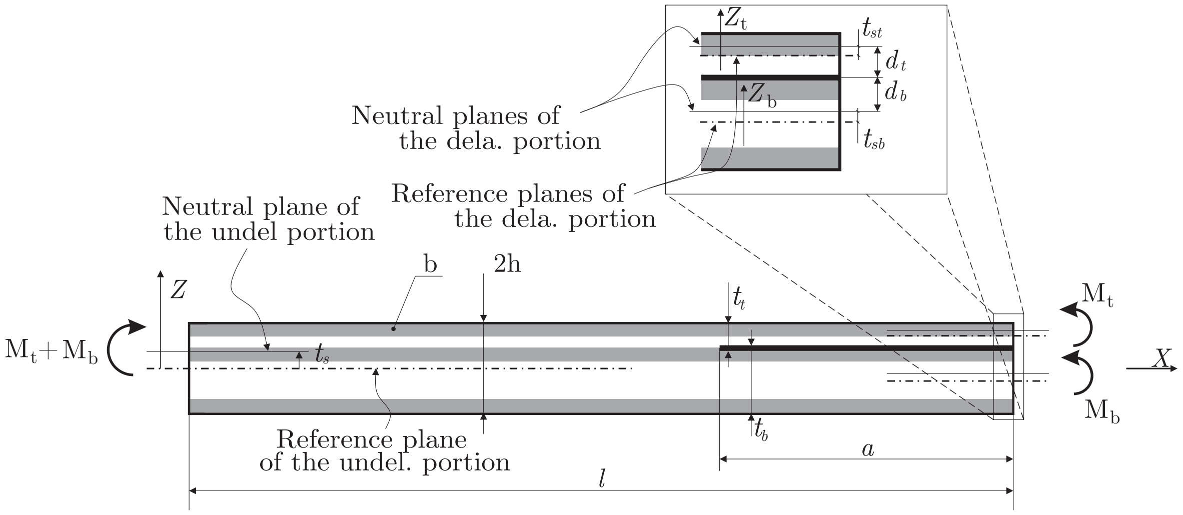
Z_t
t_{st}
d_t
d_b
Z_b
t_{sb}
Neutral planes of the dela. portion
Reference planes of the dela. portion
Neutral plane of the undel portion
b
2h
Z
t_t
M_t
M_t+M_b
t_s
X
M_b
t_b
Reference plane of the undel. portion
a
l

FIGURE B.2: General loading scenario and the offset of the neutral planes in the case of composite specimen with orthotropic plies.

as:

$$D_{11}^{(undel)} = b\frac{1}{3}\sum_{m=1}^{N_l}\overline{C}_{11}^{(m)}([z_{m+1}-t_s]^3-[z_m-t_s]^3), \tag{B.7}$$

furthermore:

$$D_{11}^{(top)} = b\frac{1}{3}\sum_{m=1}^{N_l^{(top)}}\overline{C}_{11}^{(m)}([z_{m+1}^{(top)}-t_{st}]^3-[z_m^{(top)}-t_{st}]^3), \tag{B.8}$$

and:

$$D_{11}^{(bot)} = b\frac{1}{3}\sum_{m=1}^{N_l^{(bot)}}\overline{C}_{11}^{(m)}([z_{m+1}^{(bot)}-t_{sb}]^3-[z_m^{(bot)}-t_{sb}]^3). \tag{B.9}$$

where $(undel)$ referes to the undelaminated protion, and (top), (bot) superscripts to the top and bottom sub-laminates of the delaminated portions, separately. Utilizing the calculated stiffnesses the strain energy of the system can be obtained:

$$U = \frac{1}{2}\Big(\frac{(M_t+M_b)^2(l-a)}{D_{11}^{(undel)}}+\frac{M_t^2 a}{D_{11}^{(top)}}+\frac{M_b^2 a}{D_{11}^{(bot)}}\Big). \tag{B.10}$$

And finally, the G_T total energy release rate of the system, according to the Irwin-Kies formula [2], can be determined as:

$$G_T = \frac{1}{b}\frac{dU}{da}. \tag{B.11}$$

B.2.1 Curvature based solution (Williams)

To carry out energy release rate partition, the bending moments can be decomposed into its mode components:

$$\begin{aligned} M_t &= M_I + M_{II} \\ M_b &= \alpha M_I + \psi M_{II}, \end{aligned} \tag{B.12}$$

where M_I denotes that part of the bending moment which contributes to mode-I and M_{II} represents that part which contributes to mode-II energy release rate. Furthermore, α and ψ are unknown parameters which have to be determined by using assumptions. In order to make mode separation possible, Williams proposed to use curvature equality. Therefore, in the case of pure mode-II tests, the curvatures of the sub-laminate deflections are equal to each other along the delamination length. By assuming pure mode-II loading scenario:

$$\begin{aligned} M_I = 0 \longrightarrow\ & M_t = M_{II}, \\ & M_b = \psi M_{II}, \end{aligned} \tag{B.13}$$

and by expressing the curvatures of the sub-laminate deflections:

$$\frac{M_t}{D_{11}^{(top)}} = \frac{M_b}{D_{11}^{(bot)}} \longrightarrow \frac{M_{II}}{D_{11}^{(top)}} = \frac{\psi M_{II}}{D_{11}^{(bot)}}, \tag{B.14}$$

from which the ψ unknown parameter can be determined as:

$$\psi = \frac{D_{11}^{(bot)}}{D_{11}^{(top)}}. \tag{B.15}$$

In order to determine α, everything has to be substituted back to the Eq.(B.11). Hereby, one important property of the G_T is utilized by referring to Eq.(4.10). According to it, the total energy release rate cannot contain $M_I M_{II}$ mixed product terms. By collecting the mixed product term and, in order to vanish, make it equal to zero:

$$M_I M_{II}: \ \left(\frac{(1 + D_{11}^{(bot)}/D_{11}^{(top)})(1+\alpha)}{bD_{11}^{(undel)}} + \frac{1}{bD_{11}^{(top)}} + \frac{\alpha}{bD_{11}^{(bot)}} \right) M_I M_{II} = 0, \tag{B.16}$$

this leads to:

$$\alpha = -1. \tag{B.17}$$

Imposing these conditions, the mode partitiong can already be accomplished by:

$$M_I: \ G_I = \frac{1}{2}\left(\frac{bD_{11}^{(top)} D_{11}^{(bot)}}{(D_{11}^{(top)} + D_{11}^{(bot)})} \right) M_{II}^2 \qquad M_{II},: \ G_{II} = \frac{1}{2}\left(... \right) M_I^2. \tag{B.18}$$

In the remaining parts only the necessary conditions are modified. The algorithm of the partitioning is exactly the same.

B.2.2 Strain and stress based solutions (Bruno-Greco and Williams)

According to these solutions, pure mode-I condition produce the same strain at the delamination tip. By assuming this type of loading scenario:

$$\begin{aligned} M_{II} = 0 \longrightarrow M_t &= M_I \\ M_b &= \alpha M_I, \end{aligned} \tag{B.19}$$

and by using this condition leads to the following relation for α :

$$-\frac{M_t}{D_{11}^{(top)}} d_t = \frac{M_b}{D_{11}^{(bot)}} d_b \longrightarrow -\frac{M_I}{D_{11}^{(top)}} d_t = \frac{\alpha M_I}{D_{11}^{(bot)}} d_b, \tag{B.20}$$

where d_t and d_b denote the distance of the neutral planes from the delmination by referring again to Figure B.2. Furthermore, according to the previously introduced algorithm, ψ is obtained by imposing that the mixed-term must be zero. This solution can be found in the literature as Bruno-Greco solution, although, it contains Williams stress based solution, as well. If the specimen is made by using only one type of material, meaning the E_{11} material parameters of the sub-laminates are equal to each other, the strain condition is equivalent with the stress condition. This solution is referred to as Williams stress based solution.

B.3 VCCT

The virtual crack closure technique (VCCT) for determination of energy release rate has been proposed for 40 years ago. According to it, as it is depicted by Figure B.3, the so-called "Davidson-mesh" has to be built up in the small vicinity of the delamination front. By reading out the F_{ki} nodal forces and u_{ki} nodal displacements of the k^{th} node, the energy relase rates become:

$$G_i = \frac{1}{2b\Delta c} \sum_{k=1}^{2} F_{ki} u_{ki} \qquad (i = 1, 2, 3) \tag{B.21}$$

where i refers to the mode type, b and Δc represent the geometry of the applied mesh. This technique is equally applicable for numerical calculation of mode-I, mode-II and mode-III energy relase rates by using even 2D or 3D elements.

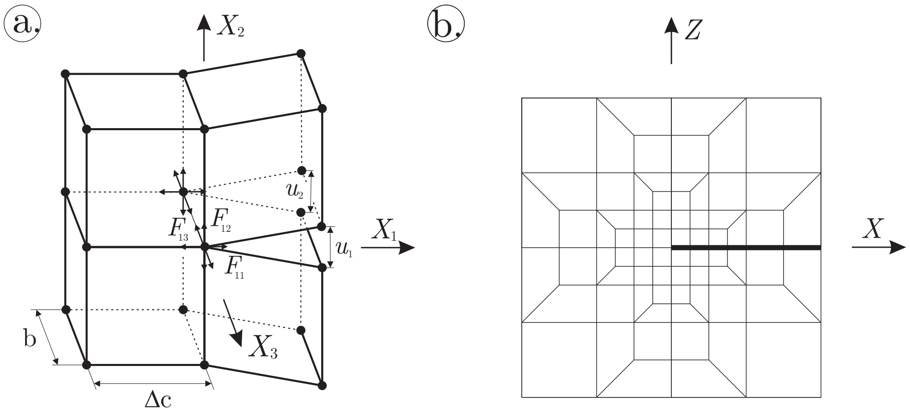

FIGURE B.3: The VCCT technique (a) and the special Davidson-mesh around the crack tip (b).

Appendix C

Laminated composite beams with complex lay-up sequence

Application of the semi-layerwise model is possible to describe laminated composite beams with quite complex lay-up sequence, as well. Figure C.1 represents beam configurations with $[\pm 45^f/0/\pm 45_2^f/\bar{0}]_S$ lay-up structure as an example. Hereby only two delamination scenarios are presented. The structures are investigated under built-in configuration referring to Figure 5.1 with different loading cases. The necessary boundary and continuity conditions can be formulated in absolutely the same way at it was discussed. Table 5.1 contains the elastic properties of the plies. The mode mixity can be compared to each other.

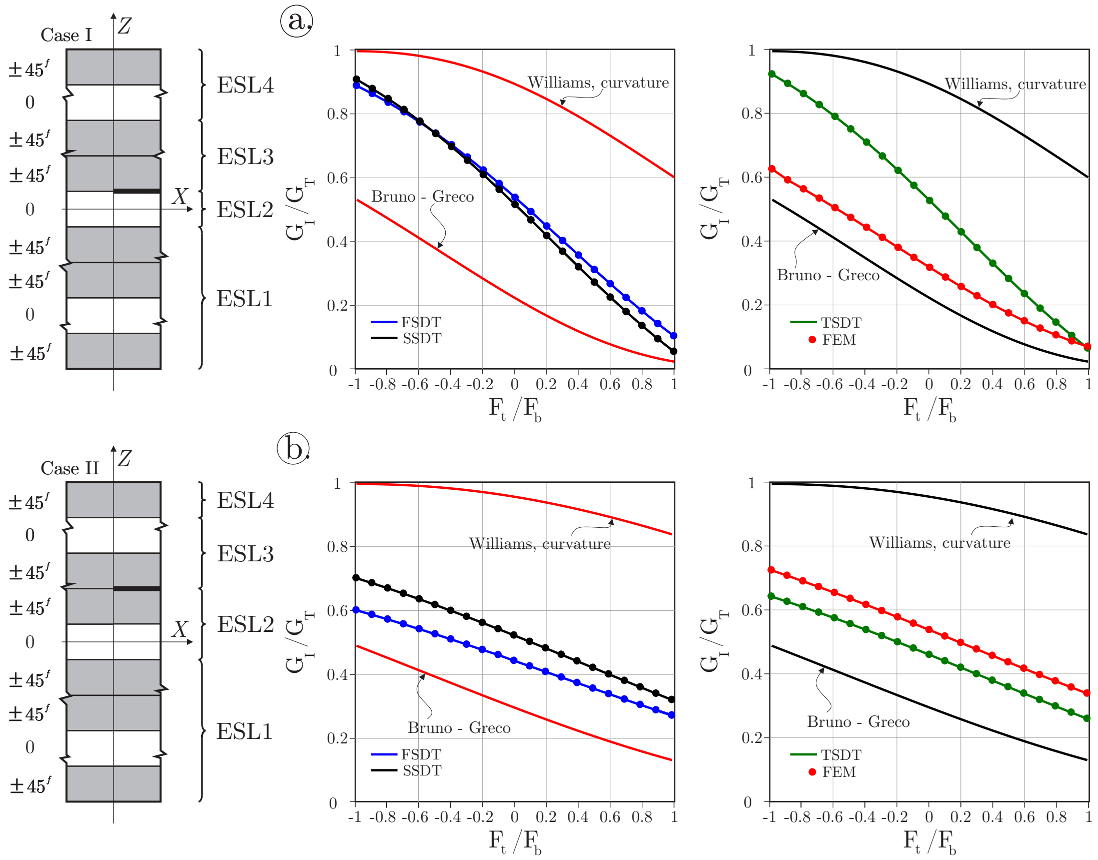

FIGURE C.1: Comparison of different delamination scenarios with Bruno-Greco solution, numerical evaluation and higher-order theorems. The delamination is located between 0 - $\pm 45^f$ layers (a) and $\pm 45^f$ - $\pm 45^f$, $a/l = 1/3$, $b = 20$ mm and $2h = 4.5$ mm.